Michael Reppel

Novel HTS Microstrip Resonator Configurations for Microwave Bandpass Filters

Witten, Germany
September 2000

Novel HTS Microstrip Resonator Configurations for Microwave Bandpass Filters

Vom Fachbereich Elektrotechnik und Informationstechnik der
Bergischen Universität – Gesamthochschule Wuppertal
angenommene Dissertation
zur Erlangung des akademischen Grades eines
Doktor–Ingenieurs

von
Diplom–Ingenieur
Michael Reppel
aus
Witten

Tag der mündlichen Prüfung:
23.06.2000

Referenten:
Prof. Dr.-Ing. Heinz Chaloupka
Prof. Dr.-Ing. Volkert Hansen

Contents

Summary

This work introduces novel microstrip resonator configurations and presents experimental results of superconducting filters developed based on this configurations.

The suggested resonator type, which forms the building block for filters, is especially qualified for applications where a weak coupling is required, e.g. for narrow–band filters with a high selectivity because of its doubly–symmetric design. Furthermore, the natural phase of the coupling of two resonators can be altered so that filters which depend on cross–couplings with specific phases can easily be built. This is the case e.g. for quasi–elliptic or self–equalising filters. Using high temperature superconductors high unloaded quality factors which exceed those of conventional resonators can be achieved.

The first chapter of this work gives a short introduction into the topic. In chapter two the novel resonator design and the coupling method is explained after a brief introduction into planar microstrip resonators. It is also shown that the new design implies a unique tuning capability for the coupling coefficients of a filter.

The next chapter discusses the issue of microstrip resonators fabricated from high temperature superconducters. It is shown that due to the extremely low conductor losses of HTS materials other loss contributions as e.g. packaging losses can dominate the overall unloaded quality factor and that the novel microstrip resonator is relatively immune to such losses compared to conventional resonators.

After the measurement methods and set–ups are briefly explained in chapter four, experimental results for the HTS resonators and filters are presented in the next chapter. Firstly, the fabrication of the devices is illustrated, and then measured results of the unloaded quality factor of different microstrip resonators are presented. A validation for the unique coupling method of the doubly–symmetric resonator is given with two–pole test filters. It is experimentally shown that the natural phase as well as the coupling strength can easily be chosen. Based on the novel resonator, the designs and experimental results for filters with a high selectivity are described. Firstly, a four–pole filter design with a quasi–elliptic response at $\sim$2 GHz and a bandwidth of only 5 MHz, that is 0.25 % fractional bandwidth, is presented. Then, designs and results of two quasi–elliptic nine–pole

filters at ∼1715 MHz (∼1775 MHz) with 10.5 MHz (15 MHz) bandwidth are shown. Finally, measurement results of an alternative filter based on meander–line resonators are presented. All the developed and measured filters had steep filter skirts and low insertion loss. Results of intermodulation measurements obtained with the latter filter are presented at the end of this chapter.

The last chapter deals with filter tuning issues. It describes how filter parameters (centre frequencies of the resonators, coupling coefficients and external quality factor) can be experimentally determined. It further suggests a step by step tuning method if the measured filter response differs significantly from the theoretical design.

Chapter 1

Introduction

The rapid growth of communication systems and the emerging practise of spectrum auctions have increasingly necessitates an efficient usage of the limited frequency spectrum, and with increasing subscriber numbers the interference between different systems may increase. For example, in the third generation mobile communication system (UMTS), which will be introduced in Europe in about 2003, the frequency bands of time domain duplex (TDD) systems are directly adjacent to frequency domain duplex (FDD) systems. Whereas in FDD systems the up–link (mobile to base station) and the down–link (base station to mobile) operate at separate frequencies, the up– and down–link of a TDD system operate at the same frequency. If the location of a FDD system base station is close to a TDD system base station, the weak up–link signals of mobile subscribers of the FDD system are interfered by strong down–link signals of the TDD base station. To avoid intermodulation in the RF front ends, highly selective preselect filters are required for an efficient exploitation of the spectrum.

To give reasons for the latter statement, Fig. 1.1 shows two simplified receiver front ends for one sector of a mobile communication base transceiver station (BTS) in case of strong interference by out–of–band signals (e.g. of a different TDD mobile system). The case (a) depicts a front end with a preselect filter of moderate selectivity, whereas in (b) a filter with high selectivity is used.

Because of the moderate filter selectivity in case (a), the signal strength of the interferers is still high at the input of the low noise amplifier (LNA). However, a real LNA becomes nonlinear at a relatively low power level, and as consequence intermodulation products emerge at the output of the LNA. The frequencies of some of these products are within the system bandwidth, and the bit error rate of up–link signals may therefore significantly increase. In order to avoid such incidences, highly selective filters with steep filter skirts are required. As depicted in Fig. 1.1 (b), such filters are able to reduce interfering signals to power levels that

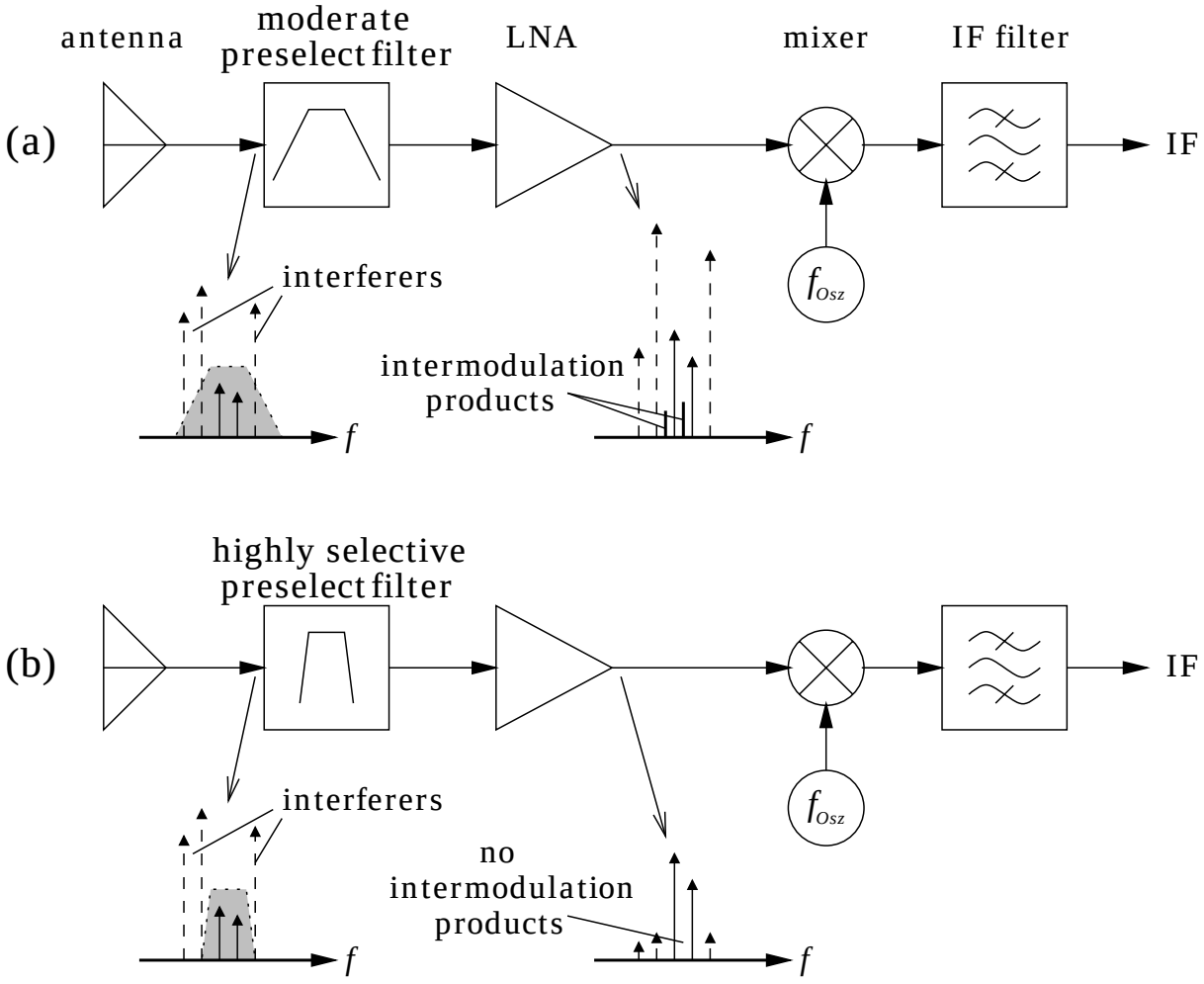

Figure 1.1: Simplified receiver front ends of one sector of a mobile communication BTS in case of an unfavourable receive situation: (a) preselect filter with moderate selectivity, (b) preselect filter with high selectivity.

do not cause nonlinearity of the LNA. However, only filters consisting of resonators with high unloaded quality factors can possess both, steep filter skirts as well as low insertion loss.

Planar microstrip resonators made of high temperature superconducting (HTS) materials are well suited to meet the requirements of highly selective preselect filters. On the one hand, HTS resonators can achieve unloaded quality factors which are significantly higher than those of any conventional resonator, and on the other hand, the planar technology offers the opportunity for miniaturisation. By way of examples, at cryogenic temperatures between 60 K and 80 K and frequencies of about 2 GHz, small HTS microstrip resonators possess unloaded quality factors between 50,000 and 100,000 whereas quality factors of bulky waveguide resonators are between 10,000 and 20,000. The commonly used coaxial resonators possess quality factors between 1,000 and 5,000.

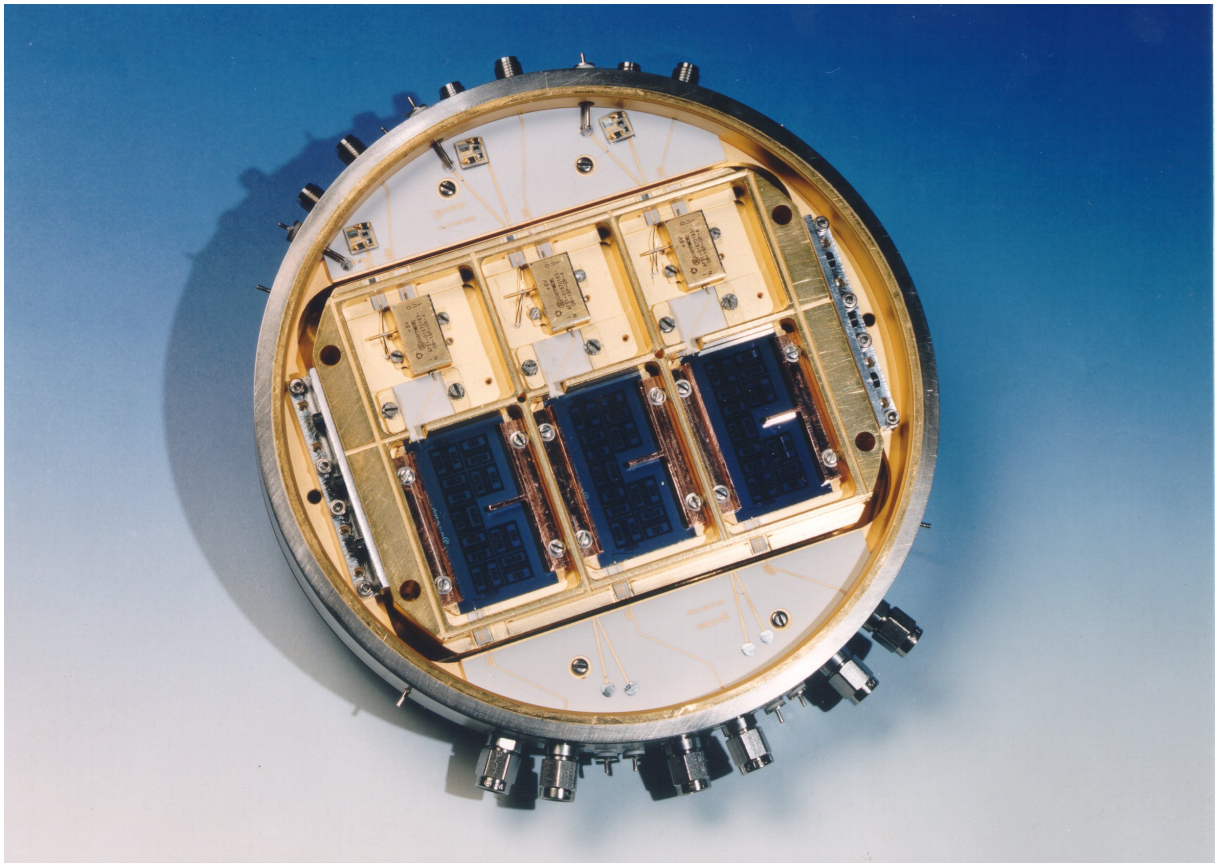

Figure 1.2: Photo of a cryogenic front end with six highly selective HTS filters and LNAs (three on each side of the ring) developed within the ACTS project SUCOMS (courtesy of GEC Marconi Research Centre, Chelmsford, UK).

Although the required cooler reduces the miniaturisation advantage, a system with a high number of filters can still be built extremely compact. Furthermore, a cryogenic unit can include other system components. If for example the low noise amplifiers of a receive system are cooled to temperatures below 100 K, the noise figures of the amplifiers are significantly reduced (e.g. from 1 dB to only 0.2 dB).

This work introduces novel microstrip resonator structures and presents designs and experimental results of highly selective HTS filters based on these resonator structures. The proposed structures are especially suitable for narrow–band receive filters with quasi–elliptic filter response. Initially, the resonator layout was developed within the ACTS* project SUCOMS† which was funded by the European Commission. The objective of this project was the development of a cryogenic front end for a demonstrator basestation. Fig. 1.2 shows details of the cryogenic unit with six HTS nine–pole filters (three on either side of the “ring”) based on the novel resonator layout and the integrated low noise

*ACTS = Advanced Communications Technologies & Services
†SUCOMS = Superconducting Systems for Communications

amplifiers. In combination with an appropriate duplexer, this unit can be used with a three–sector antenna and a diversity antenna. The ring was developed by GEC Marconi Infra Red, Southampton, UK and GEC Marconi Research Centre, Chelmsford, UK (both now BAE SYSTEMS).

Chapter 2

Planar Resonator Configurations

Planar resonators offer a convenient way to realise frequency selective microwave devices since their fabrication is relatively simple and reliable. Furthermore, with the approach of high temperature superconductivity (HTS), the disadvantage of low quality factors can be overcome. As example, Fig. 2.1 shows the principle structure of a microstrip and a coplanar resonator. The resonators are patterned into the conductor metallization of a specific substrate material which is usually mounted in a metallic housing. In case of the microstrip resonator, the second substrate side (ground plane) is completely metalised and can therefore be placed at the bottom of the housing. A coplanar structure has only one level of metallization and has to be suspended as indicated in the figure.

Since this thesis describes new microstrip resonator configurations, only this technology will be addressed further, and therefore is explained in detail. Some conventional resonator types are introduced to make the differences clear. More comprehensive descriptions of planar technology and conventional resonators can be found in the literature [1], [2].

2.1 Distributed resonators

Resonators where both the electric and magnetic field are distributed over the whole resonant structure are denoted as distributed resonators. The simplest distributed microstrip resonator is a microstrip line section of length l and width w as depicted in Fig. 2.3 (a). For a nonmagnetic substrate ($\mu_r = 1$), the lowest resonant frequency of such a resonator is given by

$$f_0 \approx \frac{1}{2\,l\,\sqrt{\varepsilon_0\ \varepsilon_{r,eff}\ \mu_0}}. \tag{2.1}$$

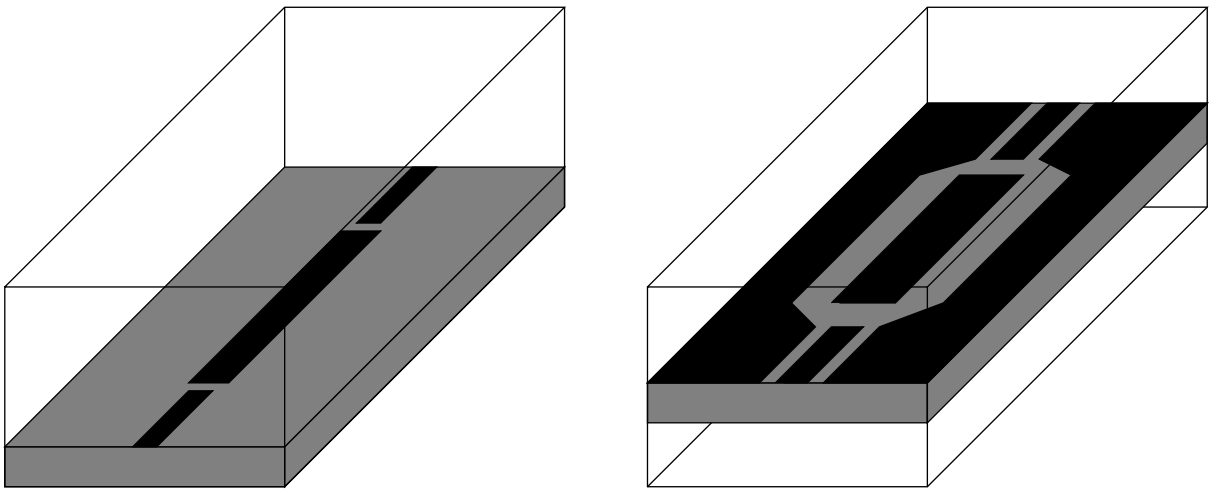

Figure 2.1: Sketches of a microstrip resonator (left) and a coplanar resonator (right) with feed lines. Black represents the conductor, gray the substrate.

Rearranging this equation gives the required length of the resonator for a given resonant frequency

$$l \approx \frac{1}{2\ f_0\ \sqrt{\varepsilon_0\ \varepsilon_{r,eff}\ \mu_0}}. \tag{2.2}$$

The effective permittivity $\varepsilon_{r,eff} < \varepsilon_r$ depends on w and on the permittivity and thickness of the substrate.

The approximate electromagnetic field distribution for a microstrip line resonator in resonance at the lowest resonant frequency ($f = f_0$) is depicted in Fig. 2.2. Whereas the electric field is mainly concentrated in the substrate between the microstrip and the ground plane, the magnetic field is expanded in the substrate as well as above the resonator. The right hand side of Fig. 2.2 shows the field distribution along the resonator. At the ends of the resonator the electric field is at maximum, and at the centre of the resonator zero. In contrast, the magnetic field is at maximum at the resonator centre.

The microstrip line resonator can significantly be miniaturised by using high permittivity substrates with $\varepsilon_r \geq 10$. Additionally, by bending the microstrip line section the resonant structure becomes more compact. Such a resonator type is

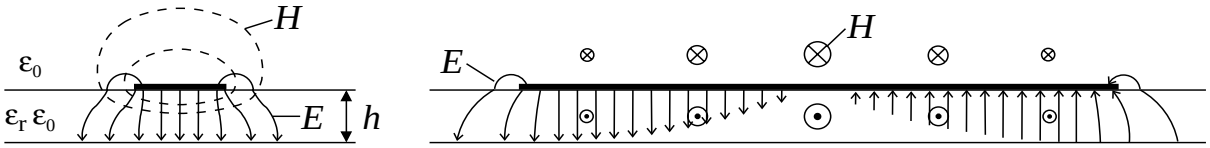

Figure 2.2: Approximate electromagnetic field distribution for a microstrip line resonator at the resonant frequency f_0; left front view, right side view.

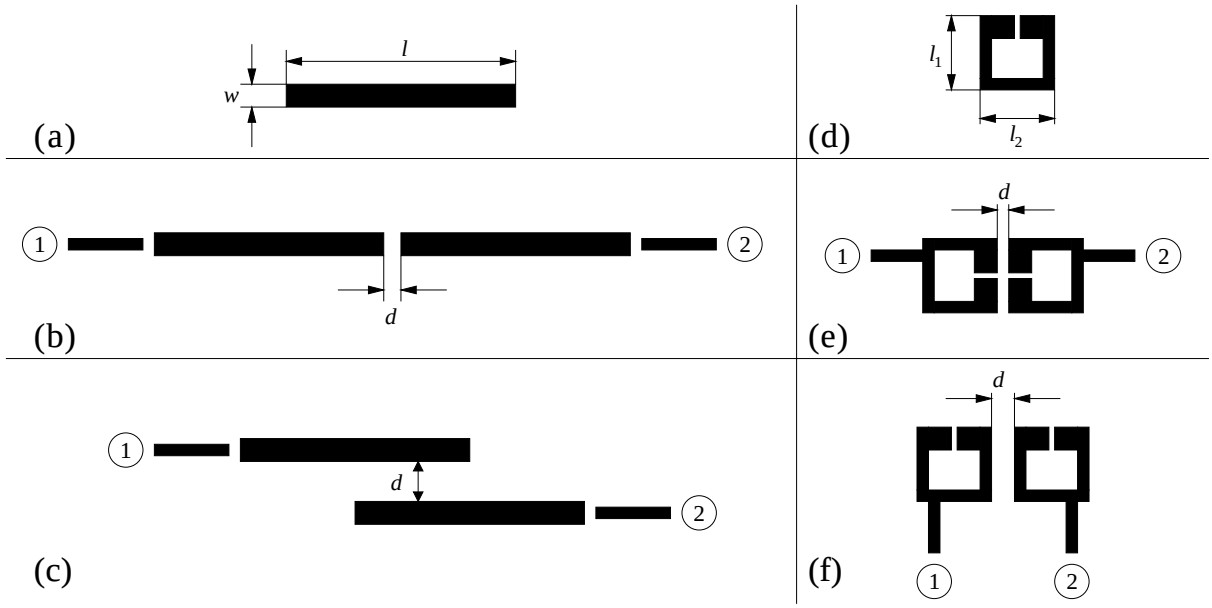

Figure 2.3: Layout of single and coupled distributed microstrip resonators: (a) microstrip line section, (d) hairpin; (b) and (c) coupled microstrip line sections, (e) and (f) coupled hairpin resonators.

known in the literature as hairpin or open–loop resonator. In Fig. 2.3 (d), a typical hairpin resonator design is shown.

2.2 Coupling of distributed resonators

Microwave bandpass filters which are based on distributed resonators are built by coupling the electromagnetic fields of the resonators. This is done by placing resonators next to each other in specified distances d. As examples, Fig. 2.3 depicts coupled microstrip line sections ((b) and (c)) and hairpin resonators ((e) and (f)). Because of the different distribution of electric and magnetic field (see Fig. 2.2), the coupling may be of electric or of magnetic nature. Mixed coupling types are also possible whereby either one type dominates or the coupling vanishes. However, the latter case is extremely sensitive to the geometric parameters.

The dependence of the coupling of two resonators on geometric parameters (coupling coefficient k) can be evaluated either theoretically, e.g. with approximation formulae or simulation software, or experimentally with a set of test devices. Knowing the angular frequencies ω_e (even mode) and ω_d (odd mode) of the eigenmodes of two coupled resonators, k may be defined by

$$k = \frac{\omega_e - \omega_d}{\sqrt{\omega_e \omega_d}}. \tag{2.3}$$

In case of $\omega_e > \omega_d$ the coupling coefficient k is positive, and in case of $\omega_e < \omega_d$

negative. The sign (or the "natural phase") of the coupling is therefore determined by the order of the eigenmodes. This order and thus the sign of the coupling coefficient depends on the nature of the coupling (electric or magnetic), but also on the position of the ports relative to the resonant structure.

Fig. 2.4 shows the equivalent circuits of two coupled resonators in case of (a) electric and (b) magnetic coupling. From these equivalent circuits the eigenmodes are given by

$$\left.\begin{aligned} \omega_e^2 &= \frac{1}{L\,C\,(1-C_k/C)} \\ \omega_d^2 &= \frac{1}{L\,C\,(1+C_k/C)} \end{aligned}\right\} \quad \omega_e > \omega_d \tag{2.4}$$

for electrically coupled resonators, and

$$\left.\begin{aligned} \omega_e^2 &= \frac{1-L/L_k}{L\,C} \\ \omega_d^2 &= \frac{1+L/L_k}{L\,C} \end{aligned}\right\} \quad \omega_e < \omega_d \tag{2.5}$$

for magnetically coupled resonators.

Examples for practical realisations of electric and magnetic coupling with hairpin resonators are shown in Fig. 2.5. Figure (a) visualizes the odd mode of electrically coupled resonators whereas (b) depicts the even mode. Because of the additional electric field between the resonators, the frequency of the odd mode is lower than the frequency of the even mode, and the coupling coefficient k is

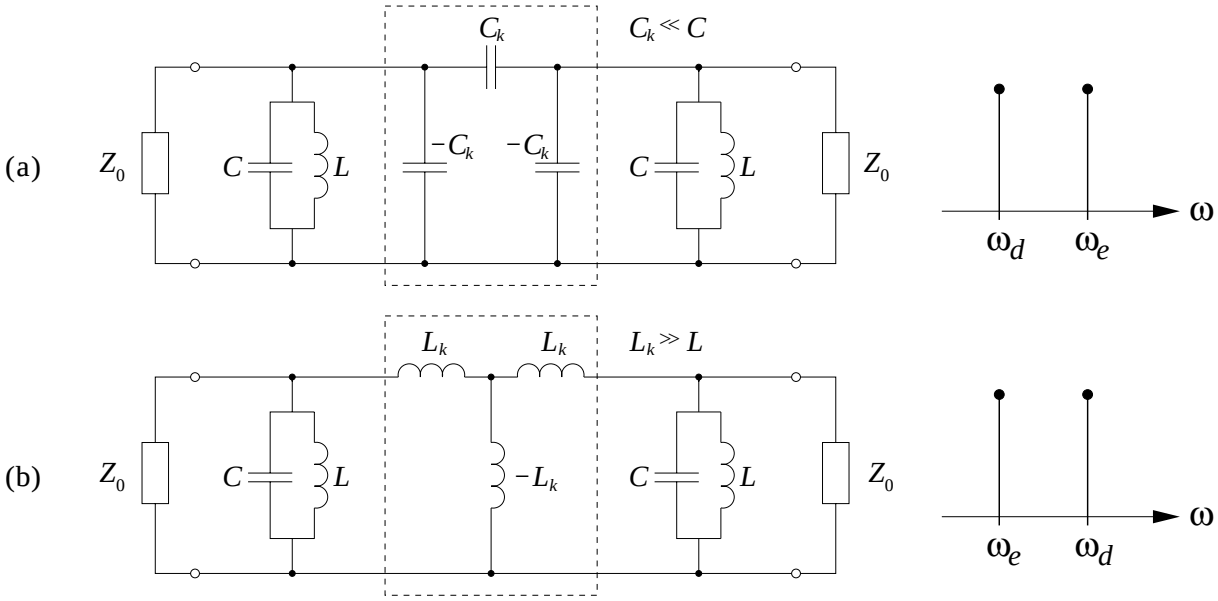

Figure 2.4: Equivalent circuits and order of the eigenmodes for coupled resonators: (a) electric coupling, (b) magnetic coupling.

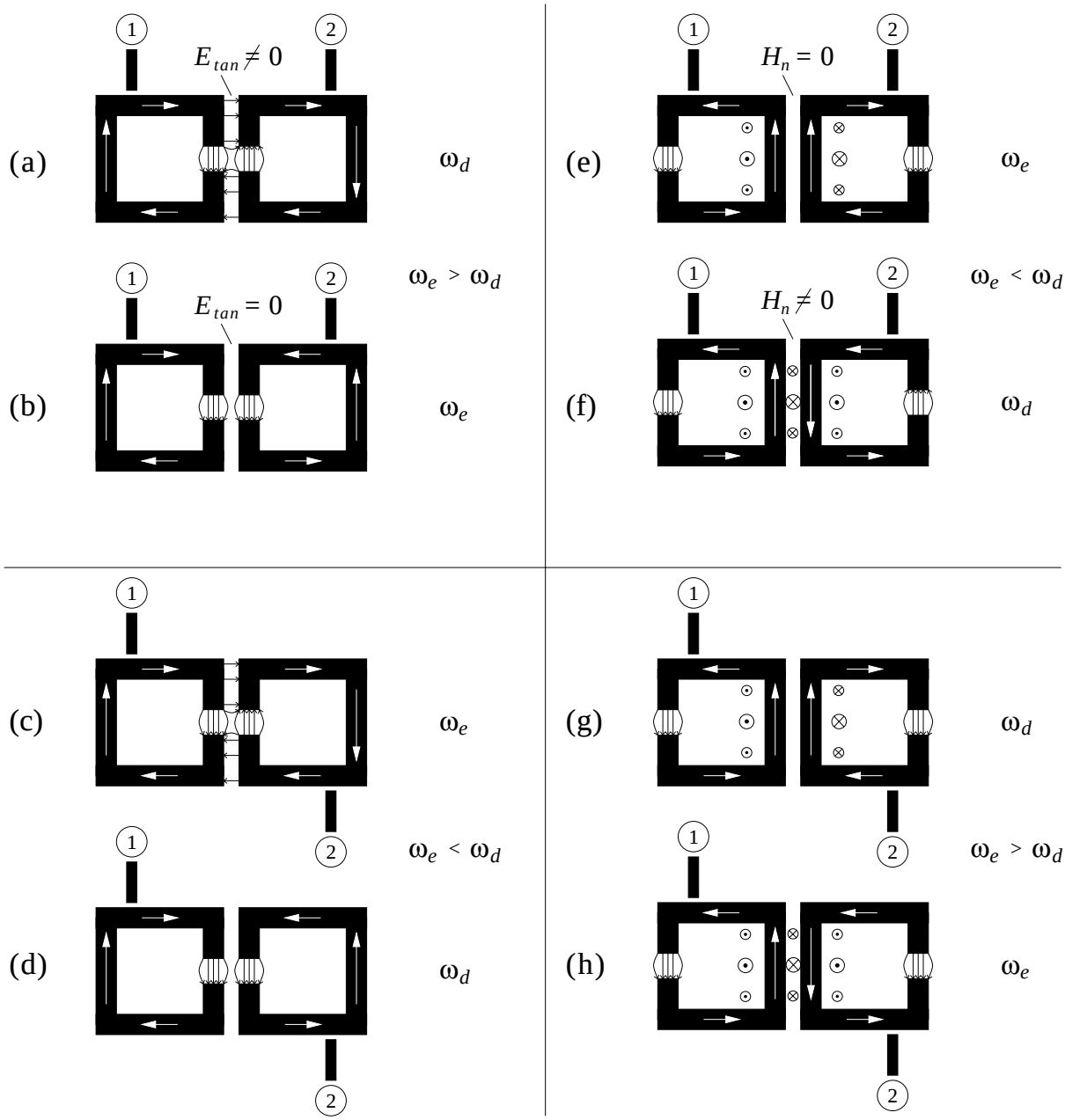

Figure 2.5: Approaches for negative and positive coupling coefficients k with hairpin resonators: (a)–(d) coupling with electric fields, (e)–(h) coupling with magnetic fields. The white arrows indicate the instantaneous current distributions of the eigenmodes

therefore positive (according to (2.3)). However, if port two is changed to the position as shown in Fig. 2.5 (c) and (d), the odd mode becomes the even mode and vice versa because of symmetry considerations. In this case, k is negative.

In case of magnetically coupled resonators (Fig. 2.5 (e) and (f)) and the same port positions as in (a) and (b) , a negative coupling coefficient results. If the position of port two is also changed as in (c) and (d), the coupling becomes positive.

2.3 Lumped element resonators

In comparison to the distributed case, if the field components are concentrated, a resonant structure may be described as a lumped element resonator. In other words, the parts of the resonator where the magnetic energy is stored is seperated from the parts where the electric energy is stored. One advantage of this approach is a possible direct transformation of an equivalent circuit consisting of capacitors and inductors into a microstrip structure. This is however limited by the planar technology itself as well as fabrication restrictions.

Generally, lumped element resonators lead to a significant size reduction and are therefore interesting for filters at lower frequencies. On the other hand, the unloaded quality factor of lumped element resonators is significantly lower when compared with distributed resonators as metallization and dielectric losses have much higher influence. A realised structure is therefore always a compromise between miniaturisation and tolerable losses.

High temperature superconducting materials offer a way to extreme miniaturisation while still maintaining high quality factors. Because of the lower surface resistance R_s (see 3.5) of HTS materials compared to normal conductors, elements with very narrow lines can be realised without increasing dissipative losses. This is especially attractive if a large number of filters is required, e.g. in filter banks. In Fig. 2.6, two examples for lumped element resonators in microstrip technology are depicted.

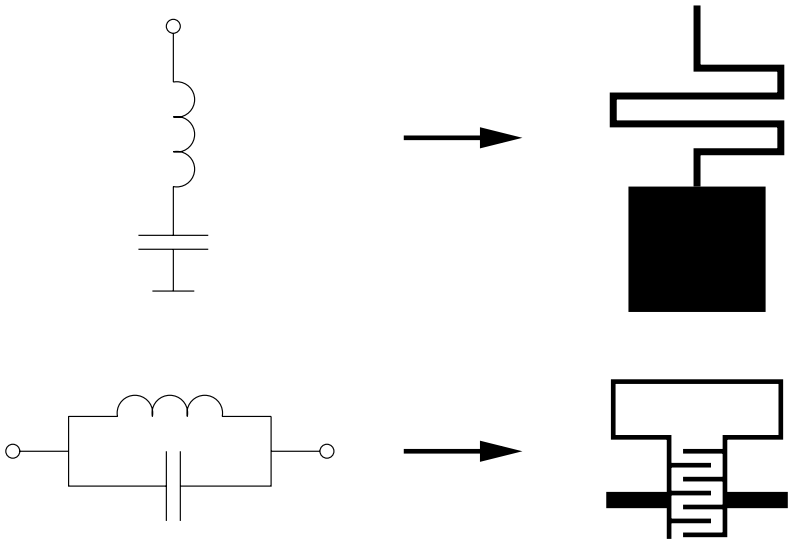

Figure 2.6: Examples for lumped element resonators in microstrip technology: series resonator (top) and shunt resonator (below).

2.4 Novel doubly–symmetric microstrip resonator

With the resonators described in the previous sections the development of planar filters with moderate selectivity (e.g. low order Chebyshev filters) is a relatively simple task. However, if highly selective filters are required, these resonators face some restrictions. In case of narrow–band filters for example, the spacing between two adjacent distributed resonators can become relatively large. Furthermore, if filters are to be fabricated using high temperature superconductors, distributed planar resonators such as microstrip line sections are limited with respect to the achievable unloaded quality factor Q_0 as explained in detail in a later chapter. These restrictions have been the motivation for the development of a new microstrip resonator, which is described in the following section.

2.4.1 Resonator design and coupling between resonators

In principle, the layout of the novel resonator, which serves as building block for bandpass filters, is similar to the layout of the hairpin resonator. However, the novel resonator has two planes of symmetry and thus can be refered to as doubly–symmetric hairpin resonator. Fig. 2.7 shows the novel design compared with a conventional hairpin resonator.

The main advantage of this new design is the fact that two of these resonators can be placed extremely close to each other by ensuring that a very weak coupling coefficient exists between them. For this to be achieved, one resonator has to be rotated by 90 degrees as depicted in Fig. 2.8. In this case if resonator one is excited externally, the currents in its branches excite currents in resonator two as indicated in the figure. As consequence of the symmetry, the currents $I_2^{'}$ and $I_2^{''}$ are

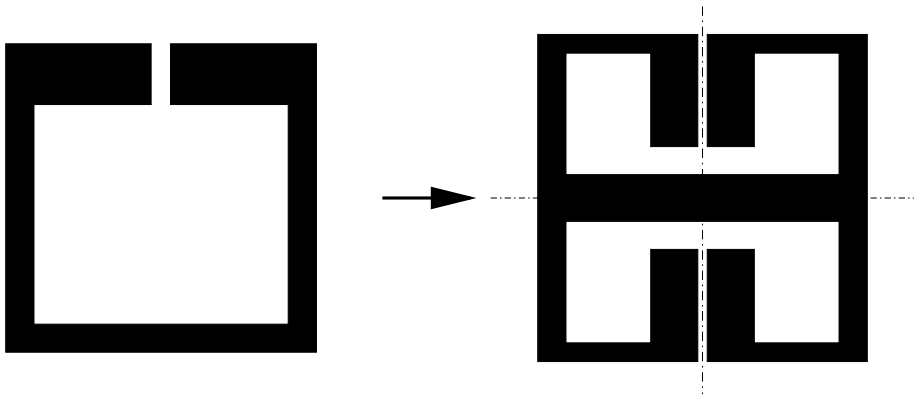

Figure 2.7: Layout of the novel doubly–symmetric hairpin resonator compared with a conventional hairpin resonator (black representing the conductor).

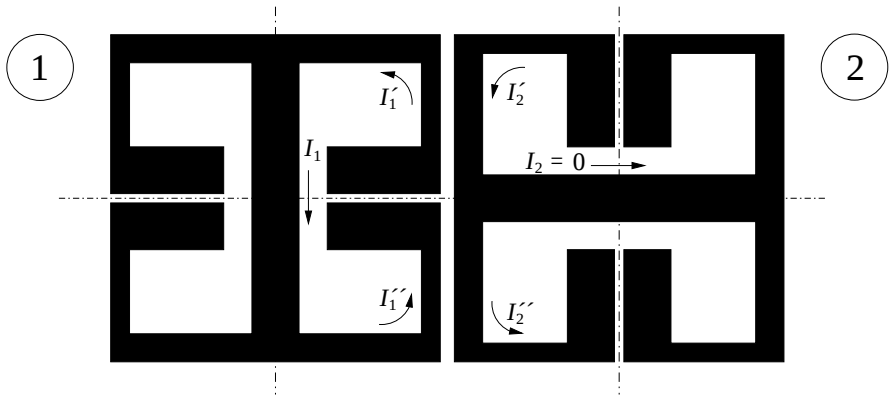

Figure 2.8: Two closely placed novel resonators which are not coupled because of symmetry aspects: the currents $I_2^{'}$ and $I_2^{''}$ are equal and $I_2 = 0$ results therefore.

identical and the current I_2 in the main branch of resonator two is zero. Since the remaining branches are not in resonance, the magnitudes of the excited currents $I_2^{'}$ and $I_2^{''}$ are low giving a negligible coupling between the two resonators.

To obtain a defined coupling between the two resonators, one plane of symmetry of resonator two has to be perturbed as depicted in Fig. 2.9. The introduced asymmetry results in a current $I_2 \neq 0$ in the main branch of resonator two as the currents $I_2^{'}$ and $I_2^{''}$ are unequal now. The functional dependence of the coupling coefficient between the resonators and the asymmetry has been investigated with the help of electromagnetic full–wave analysis software [3]. In Fig. 2.10 (left hand side), the asymmetry is defined by the geometric difference $x_1 - x_2$, and the obtained simulation result (right hand side of the figure) suggest a nearly linear dependence between this difference and the coupling coefficient k (as this investigation was to show the principle dependence, no other geometric or material

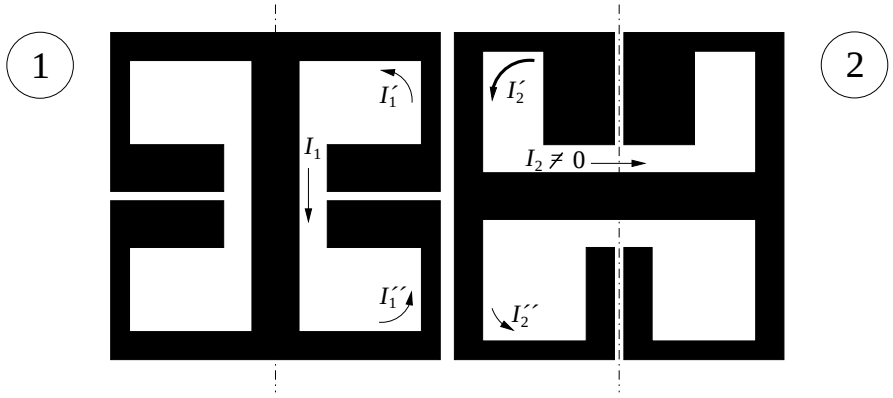

Figure 2.9: Two closely placed novel resonators which are coupled due to the asymmetry of resonator two ($I_2^{'} \neq I_2^{''}$, $I_2 \neq 0$).

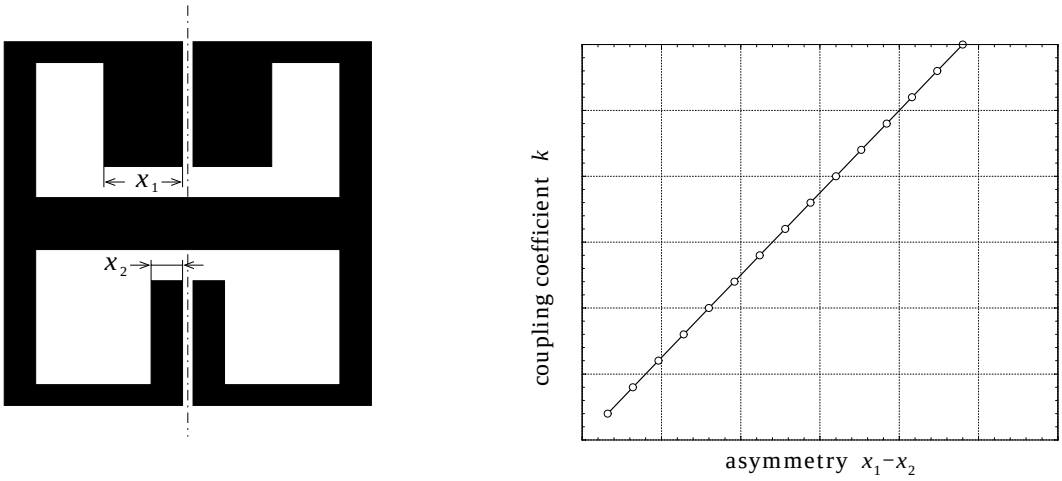

Figure 2.10: Definition of the asymmetry by the geometric difference $x_1 - x_2$ (left hand side) and functional dependence (right hand side) of the coupling coefficient. The obtained functional dependence is nearly linear.

parameters are mentioned). The absolute value of the coupling coefficient between two doubly–symmetric hairpin resonators is determined by

- the degree of asymmetry
- the distance of the resonators
- the geometric parameters of the resonators, e.g. line width
- thickness and permittivity of the substrate material

which means that besides the asymmetry, the same parameters as used with conventional resonators are available. On the other hand, the asymmetry is limited by the geometry of the resonator, which gives a limitation for the maximum achievable coupling coefficient. Because of this, this resonator type is restricted to narrow–band applications (e.g. bandpass filters with a fractional bandwidth of 2 % or less).

2.4.2 Couplings of different natural phases

Up to this point, only the strength of the coupling has been discussed, which corresponds to the magnitude of a transmitted signal through two resonators when the resonators are connected to ports with an external quality factor Q_{ext} (see also (D.5) on page 80). On the other hand, the (natural) phase of this signal is equivalent to the sign of the coupling as defined with (2.3).

In the design of a specific class of socalled quasi– or pseude–elliptic function filters, additional cross–couplings between nonadjacent resonators are required. If such cross–couplings are of different natural phase with respect to the main couplings, symmetric transmission zero pairs occur, which increase the filter selectivity. In the case where cross–couplings with the same natural phase occur, self–equalising filters can be designed [4]. In planar technology however, the natural phase of couplings cannot be selected arbitrarily but depends on the specific resonator design.

Implementing the doubly–symmetric hairpin resonator, a new way for the realisation of couplings with different natural phases is introduced. In Fig. 2.11, the layouts of two two–pole test filters are shown. The only difference in the two layouts is the vertically mirrored resonator on the right–hand side of filter (b). If resonator one is excited (port one), the magnitude and direction of current I_1 is equal in both cases (a) and (b). However, due to the mirrored resonator two in case (b), the direction of current I_2 is opposite as indicated in Fig. 2.11. Since the directions of the currents I_1 and I_2 can be related to the ports, case (a) may be refered to as odd mode, and case (b) as even mode. This change of the modes is directly linked to a different natural phase of the coupling, and an alternative way

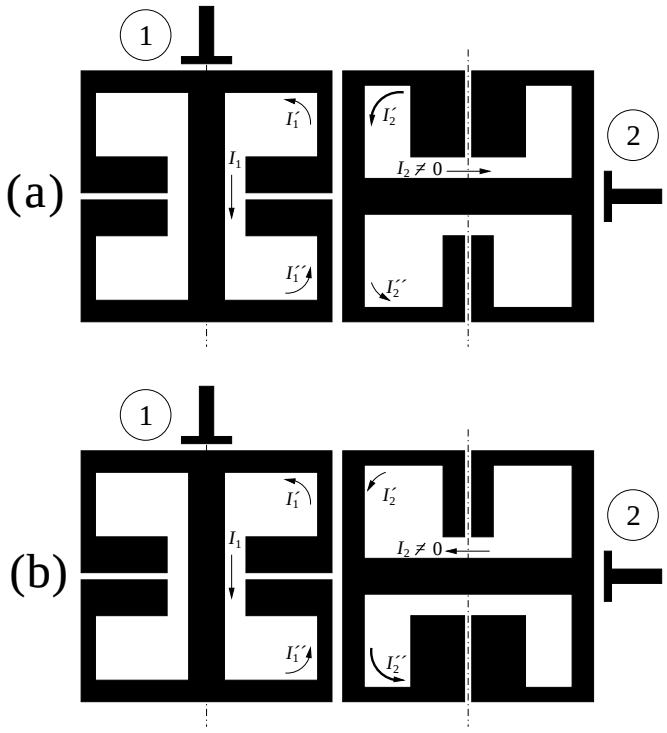

Figure 2.11: Layouts of two test filters to demonstrate couplings with different natural phases. Both filters are identical except that the resonator on the right–hand side of filter (b) is mirrored vertically.

for the design of quasi–elliptic filters has therefore been established. Experimental verification of this is described in chapter 5.

2.4.3 Superior tuning of coupling coefficients

Besides the realisation of different natural phases, the unique coupling scheme of the doubly–symmetric resonator introduces superior tuning capabilities. Although for the analysis of microwave properties of microstrip devices advanced software packages are available, tuning is often required. This is particularly the case for high order narrow–band filters because even small fabrication tolerances (e.g. substrate height, etching process) and permittivity tolerances may result in a significantly reduced performance.

With the doubly–symmetric resonator it is possible to tune not only the resonant frequency, but also the coupling coefficient between two resonators. The principle of this can be explained with the resonators depicted in Fig. 2.12. In case (a), a single resonator is shown with a specific asymmetry which gives a predetermined coupling coefficient in a filter structure. If now a dielectric tuning element is placed above the larger patches of the resonator as shown in (b), the asymmetry is increased, and consequently a larger coupling coefficient results. On the other hand, if the tuning element is placed above the smaller patches as shown in (c), the asymmetry and the coupling are decreased respectively. However, it is to note that in both cases (b) and (c) the resonant frequency of the resonator is decreased as well. This is also the case if tuning elements are placed above the larger and the smaller patches as depicted in (d). Here, the asymmetry is retained unchanged and the same coupling coefficient as in case (a) results.

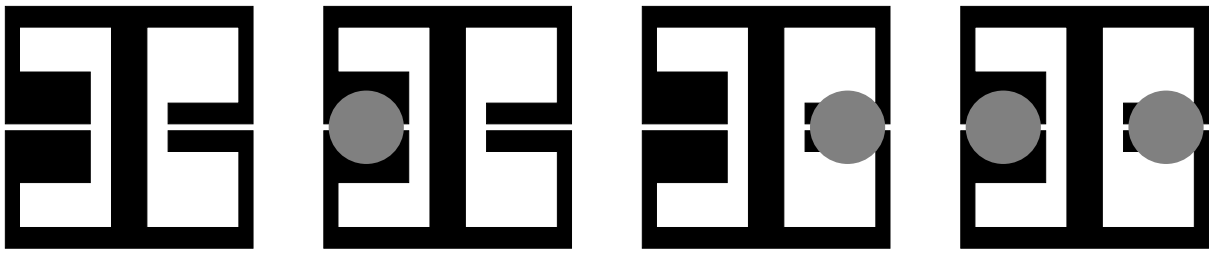

(a) (b) (c) (d)

Figure 2.12: Changing of the asymmetry with tuning screws: (a) original asymmetry; (b) increased asymmetry; (c) decreased asymmetry; (d) original asymmetry with lower resonant frequency. The gray circles represent the positions of the tuning screws above the planar structure.

Chapter 3

HTS Microstrip Resonators

Microwave resonators and filters in conventional metal planar technology suffer from reduced quality factors compared to bulky waveguide or dielectric equivalents. Their usage is therefore limited to applications where size, weight and costs are more important than e.g. insertion loss. This drawback can be overcome with the utilisation of superconductors, which were first discovered in 1911 by Onnes [5] at the expense of the need for a large cooling system. Competitive applications became only possible after the discovery of high temperature superconductivity (HTS) by Bednorz and Müller in 1986 [6]. Since that time, materials have been found which become superconductive at relatively high temperatures ($>$ 30 K). The discovery of materials with critical temperatures T_c higher than the temperature of liquid nitrogen (77 K) intensified the development of thin film planar HTS devices.

The superconductivity effect leads to a significant reduction of the surface resistance R_s of the superconducting material compared with conventional conductors such as silver or copper. Although this reduction is frequency dependant ($R_s \propto f^2$), for technically interesting frequencies ($<$ 10 GHz) the unloaded quality factor of HTS resonators is several orders of magnitudes higher than cooled conventional metals. A large number of publications dealing with HTS related topics is available, and the interested reader is refered to the literature for more detailed explanations, e.g. [7]–[10].

Within this chapter, the unloaded quality factor of HTS microstrip resonators is investigated. It will be shown that because of the reduced conductor losses other loss contributions tend to dominate.

3.1 Loss contributions

As already explained in the second chapter, microstrip resonators consist of two conductive layers on a substrate, which is fixed in a housing. For reasons of shielding, this housing is almost always metallic. Fig. 3.1 shows a cross–section of the described structure. In addition to the conductor losses, dielectric losses in the substrate and losses due to the packaging occur. If radiation losses are also present, they can be included in the packaging losses.

The unloaded quality factor of a resonator with respect to a single loss contribution is defined by

$$Q_i = \frac{\omega W}{P_{dis,i}}. \tag{3.1}$$

W denotes the stored energy in the resonator and $P_{dis,i}$ the dissipated power averaged over time. Taking different loss contributions into account, all dissipative losses may be added as they are with good approximation independent from each other:

$$\sum_i P_{dis,i} = P_{dis} = \sum_i \frac{\omega W}{Q_i} = \omega W \sum_i \frac{1}{Q_i}. \tag{3.2}$$

From this the overall unloaded quality factor Q_0 can be determined

$$\frac{1}{Q_0} = \sum_i \frac{1}{Q_i}. \tag{3.3}$$

In case of a HTS microstrip resonator with the above loss contributions Q_0 becomes

$$\frac{1}{Q_0} = \frac{1}{Q_c} + \frac{1}{Q_d} + \frac{1}{Q_p} \tag{3.4}$$

where Q_c stands for the contribution of the conductor, Q_d for dielectric losses and Q_p for packaging losses including all housing losses. From Eqn. (3.4), it is clear

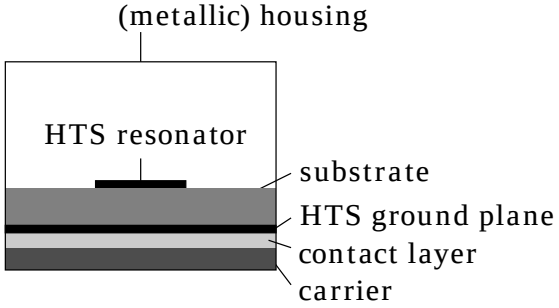

Figure 3.1: Sketch of a HTS microstrip resonator in a metallic housing.

that the overall quality factor is dominated by the lowest single quality factor. To maximise the quality factor of a structure as shown in Fig. 3.1, the highest loss contribution has to be identified. In the following subsections, these loss contributions are discussed in more detail.

3.1.1 Conductor losses

At microwave frequencies, dissipative losses of a conductor are approximately described in terms of the surface resistance R_s which is the real part of the surface impedance

$$Z_s = R_s + jX_s = \frac{E_t}{H_t} \tag{3.5}$$

at the boundary of an infinite half–plane. The tangential magnetic and electric field components E_t and H_t are at right angle. The dissipated power is given by [7]

$$P_{dis} = \frac{1}{2} R_s \int_S |H_t|^2 dS. \tag{3.6}$$

This expression is valid for both, normal (metallic) and superconductors, but is exact only for infinite half–planes. For thin films, (3.6) is an approximation, which is good for film thicknesses $t \geq 2\ \delta^*$ (normal conductors) respectively $t \geq 2\ \lambda_L{}^\dagger$ (superconductors). For thinner films, R_s increases which is known in the literature as *transparency*. Furthermore, the surface impedance concept fails close to the edges of planar structures.

The stored energy W of a resonator can be calculated from the magnetic field by

$$W = \frac{1}{2} \int_V \mathbf{HB}\ dV = \frac{1}{2}\ \mu_0 \int_V |H|^2\ dV, \tag{3.7}$$

and from (3.1) the quality factor Q_c becomes

$$Q_c = \omega\ \frac{\mu_0}{R_s}\ \frac{\int_V |H|^2\ dV}{\int_S |H_t|^2 dS} \tag{3.8}$$

A more common notation for Q_c is obtained by using the relationships

$$\omega = 2\pi f_0 = \frac{2\pi c_0}{\lambda_0} = \frac{2\pi}{\lambda_0 \sqrt{\mu_0 \varepsilon_0}},$$

$$Z_0 = \sqrt{\mu_0/\varepsilon_0} \approx 377\ \Omega$$

*δ = skin depth

†λ_L = London penetration depth. λ_L is temperature but not frequency dependant ($\lambda_L = \lambda_L(T)$)

and introducing the geometric parameter l_c:

$$Q_c = \frac{\pi\ Z_0}{\lambda_0\ R_s}\ 2\ \frac{\int_V |H|^2\ dV}{\int_S |H_t|^2 dS} = \frac{\pi\ Z_0}{\lambda_0\ R_s}\ l_c. \tag{3.9}$$

The latter expression is valid for any resonator geometry, and the quality factors of two resonators made out of the same conductive material can directly be compared by the ratio of their geometric parameters. On the other hand, Q_c is inversely proportional to the surface resistance R_s and a reduction of R_s results directly in a higher quality factor.

Of interest is the case of resonators which consist of two or more different conductive materials or where the current distribution in different parts is significantly different. For microstrip resonators, such as shown in Fig. 2.3, the current distribution in the actual resonant structure (the resonator) and the ground plane is completely different. The current in the resonator is enhanced at the edges of the microstrip line section due to the skin effect, whereas the current in the semi–infinite ground plane is almost homogeneously distributed. This implies that the losses in the microstrip line section are higher than in the ground plane (for the same R_s). An analytic expression of the current density in the ground plane of a microstrip transmission line is given in [11].

The surface current density J_s is given by the boundary condition for the tangential magnetic field which is for good conductors $|H_t| = |J_s|$, thus (3.6) becomes

$$P_{dis,res} = \frac{1}{2}\ R_{s,res} \int_{S,res} |J_{s,res}|^2\ dS \tag{3.10}$$

$$P_{dis,gp} = \frac{1}{2}\ R_{s,gp} \int_{S,gp} |J_{s,gp}|^2\ dS \tag{3.11}$$

for the losses in the resonator and in the ground plane respectively. Both loss contributions can be associated with different quality factors, which contribute to Q_c:

$$\frac{1}{Q_c} = \frac{1}{Q_{c,res}} + \frac{1}{Q_{c,gp}} \tag{3.12}$$

For a microstrip resonator made out of copper, the relation $Q_{c,gp} \gg Q_{c,res}$ holds and losses in the ground plane can be neglected. However, in case of HTS resonators there are situations where $Q_{c,gp}$ is not negligible or can even be dominant:

- Early applications of HTS microstrip resonators were sometimes fabricated with single–sided HTS thin films and a normal conductor ground plane [12]. With this approach, $Q_{c,gp}$ dominates all other loss contributions and the achievable unloaded quality factor is relatively low. This has explicitly been experienced in [13] where a silver ground plane limited Q_0 to less than 10,000 at 4.2 K, but with a Nb[‡] ground plane Q_0 increased to more than 100,000 when Nb became superconducting.

- The thin film structure has to be fixed in a housing as shown in Fig. 3.1. With double–sided films, the film can be adhered into the housing if the HTS ground plane is covered by an additional gold or silver layer. This layer provides a good ohmic contact and avoids chemical reactions between the adhesive and the HTS. However, the surface resistance of the ground plane $R_{s,gp}$ may increase as the extra normal conducting layer adds losses. This effect is especially strong if the film thickness t is smaller than $\lambda_L(T)$ (see also section 3.1.3 about packaging losses).

The sensitivity of different microstrip resonator types to a lossy ground plane can easily be investigated with the aid of full–wave simulation software [3], as it is possible to simulate losses in specific parts with all other materials being perfect conductors. From the simulation results $Q_{c,gp}$ can be evaluated for different resonator types, line widths, substrate heights and permittivities.

Four resonator types as shown in Fig. 3.2 have been investigated. The width w was varied between 0.2 and 1 mm for each resonator, and in case of

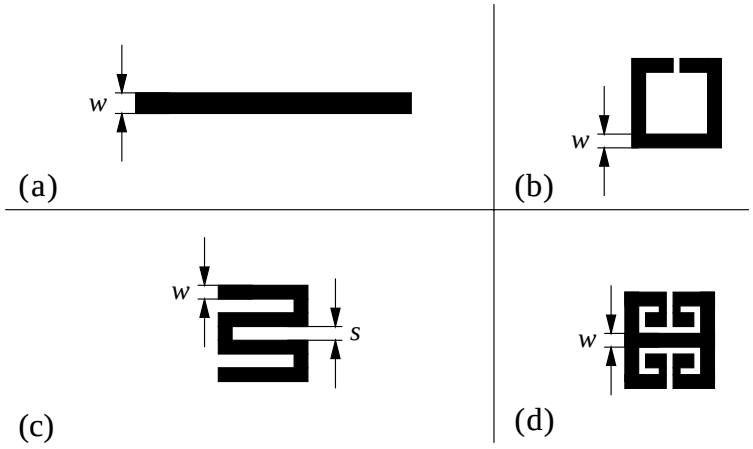

Figure 3.2: Four microstrip resonator types investigated with respect to losses in the ground plane: (a) microstrip line section, (b) hairpin, (c) meander–line, and (d) doubly–symmetric hairpin.

[‡] Nb (niobium) is a low temperature superconductor with $T_c \approx 9.2$ K

the meander–line resonator an additional parameter s for the distance (spacing) between two sections was introduced. The resonant frequency of all resonators was tuned to 2 GHz, and for the ground plane a surface resistance of $R_s = 12$ mΩ was used in the simulations. The simulation results obtained are presented in Fig. 3.3 where the product of unloaded quality factor and surface resistance ($Q_0 \times R_s$) is given as a function of the line width for different resonators and substrates. The advantage of using the product $Q_0 \times R_s$ in the graphs is that the simulation results can be used for any frequency and value of R_s as long as the condition $w \ll \lambda_g$ holds (λ_g denotes the guided wavelength $\lambda_0/\sqrt{\varepsilon_{r,eff}}$).

It can be seen from Fig. 3.3 that $Q_{c,gp}$ largely depends on the resonator geometry. With the same substrate thickness, a factor of about 10 between the lowest (wide microstrip section) and the highest value (narrow meander–line) of $Q_{c,gp}$ exists. Furthermore, for thicker substrates $Q_{c,gp}$ increases because of the lower surface tangential magnetic field H_t. On the other hand, losses in the ground plane are not dependant on the permittivity of the substrate. Although the simulation results obtained suggest the use of narrow lines, it has to be considered that losses in the resonator will increase and the power handling capability will decrease because of higher edge currents. Therefore, the line width has to be a compromise, determined by $Q_{c,gp}$ and $Q_{c,res}$.

The novel doubly–symmetric hairpin resonator and the meander–line resonator exhibit lower losses in the ground plane than the microstrip section and the conventional hairpin resonator. If double–sided HTS thin films are used, losses in the ground plane play only a minor role since they can be avoided with a proper

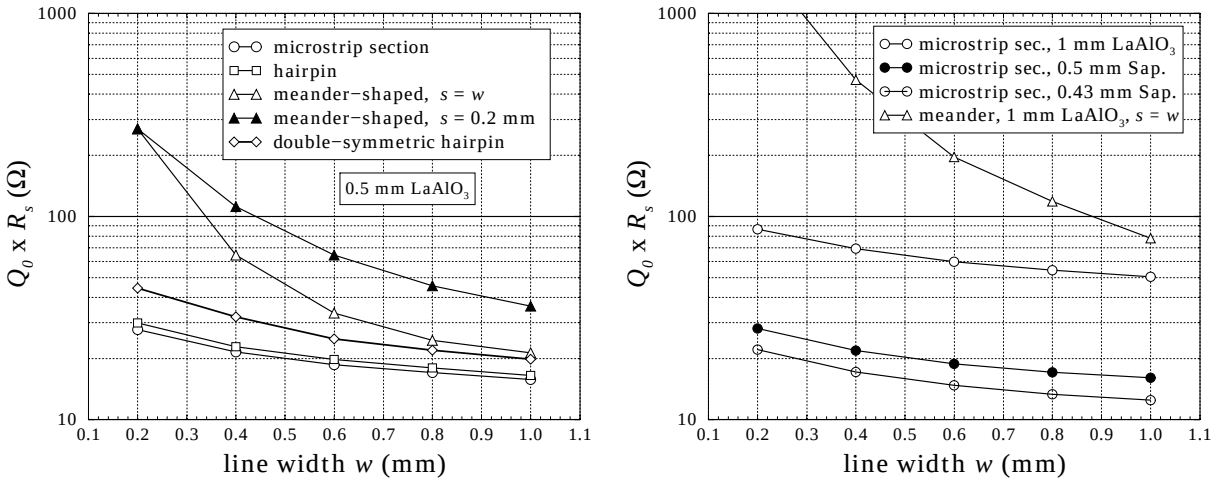

Figure 3.3: Simulation results for microstrip resonators with lossy ground planes: resonators on 0.5 mm thick $LaAlO_3$ (left), resonators on 1 mm thick $LaAlO_3$, 0.5 mm and 0.43 mm thick sapphire (right).

packaging as shown in section 3.1.3. However, these losses are directly related to housing losses and in both cases the surface magnetic field is the cause of the losses. The results obtained imply that both the doubly–symmetric hairpin resonator and the meander–line resonator are relatively insensitive to housing losses.

3.1.2 Dielectric losses

Dissipation in a dielectric material is expressed in terms of its loss tangent $\tan(\delta)$. Since the stored electric field energy is not completely contained within the substrate of a planar resonator, the loss tangent contributes only partly to dissipative losses, and this can be taken into account with a geometric factor $\beta_d \leq 1$:

$$P_{dis,d} = \omega W \ \beta_d \ \tan(\delta). \tag{3.13}$$

Q_d is therefore given by

$$Q_d = \frac{1}{\beta_d \tan(\delta)}. \tag{3.14}$$

The geometric factor β_d depends besides the permittivity and thickness of the substrate on the size and shape of the resonant structure. However, for high permittivity materials ($\varepsilon_r \geq 10$) an approximate value of $\beta_d \approx 1$ can be assumed. High quality resonators therefore require low loss substrate materials.

For planar HTS applications, the dielectric substrate material and HTS film must have a close crystal lattice match. This combined with a low $\tan(\delta)$ and other requirements means that only few dielectrics qualify as suitable substrate material. The most commonly used substrate materials are lanthanum alluminate ($LaAlO_3$), magnesium oxide (MgO) and CeO_2 buffered sapphire. However, each material has some disadvantages, which are given in table 3.1 together with material values for cryogenic temperatures ($T < 100$ K) and frequencies below 10 GHz. The numerical values in the table are only approximations which have been reported in [14]–[16]. Noting that the loss tangent value is dependant on the measurement method, and the frequencies and temperatures are different in the references.

All three substrate materials have successfully been used for HTS microwave applications. Results of test structures and filters presented in this thesis have been achieved with HTS thin films on $LaAlO_3$. Further examples of high order filters are reported on $LaAlO_3$ [17], on MgO [18], and on sapphire [19] respectively.

3.1.3 Packaging and housing losses

Packaging losses of a microstrip resonator can be classified by four loss contributions:

Table 3.1: Standard substrate materials for HTS applications.

Material	ε_r	$\tan(\delta)$	Comments
$LaAlO_3$	≈ 24	$\approx 1{\cdot}10^{-6}$ .. $8 \cdot 10^{-6}$	high miniaturisation, HTS film thickness up to $\approx$ 800 nm, twinning, loss tangent maximum at ≈ 65 K (depending on supplier and/or crystal growing method), substrates up to 3″ø
MgO	≈ 10	$\approx 2{\cdot}10^{-6}$	brittle, hygroscopic, HTS film thickness limited (≤ 350 nm), substrates up to 2″ø
Sapphire	≈ 10	$\approx 10^{-7}$	mechanically strong, low cost, buffer layer required, anisotropic, HTS film thickness limited (≤ 350 nm), substrates up to 9″ø

- losses in a passivation layer (Q_{pas}).
- radiation losses (Q_{rad})
- interfacing losses between the ground plane and carrier or base of the housing (Q_{if})
- housing losses in the top and side walls of the housing (Q_h)

For some applications passivation of the microstrip structure is required due to a humid environment or to avoid chemical reactions with the HTS. Losses in a passivation layer are mainly dielectric losses and comparable to losses in the substrate. To minimise these losses, the passivation layer must be thin, low loss and low permittivity material.

Radiation losses have to be taken into account if a microstrip resonator is used in a non–metallic or open housing. Being similar to an antenna element, a radiation impedance can be defined, and the real part of this impedance is a measure of the radiated and thus lost power. However, since microstrip resonators and filters are almost always mounted in metallic housings for reasons of shielding, radiation will not be discussed further. On the other hand, the comparision with antenna elements is useful with respect to the reactive part of the radiation impedance. The reactive part of the field (near field) does not contribute to losses in an open structure, but in a closed housing currents in the housing walls are induced. This produces dissipative losses according to Eqn. (3.6) whereby the geometry of the resonator determines the field distribution and consequently effects the losses.

As shown in Fig. 3.1, the ground plane of a microstrip structure can be fixed in a metallic housing or onto a carrier with a conductive epoxy adhesive paste or film. To avoid chemical reactions, the HTS is usually covered with a thin gold or silver layer. If the superconducting ground plane is too thin with respect to the London penetration depth λ_L, interfacing losses will occur. In that case, an increased surface resistance R_s of the ground plane results (see also Eqn. (3.11)). This effect can be reduced or avoided with a proper packaging and is discussed here.

A system of different conductive and thick layers can be modelled with transmission lines as shown in Fig. 3.4 if infinitely expanded planes are supposed.

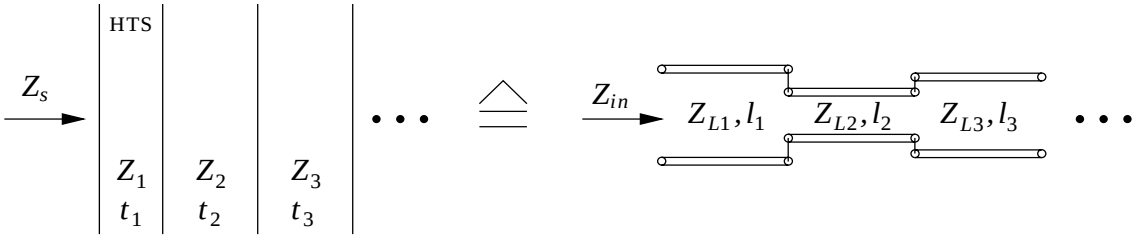

Figure 3.4: System of infinitely expanded planes and equivalent transmission line model.

Additionally, the model is valid for dielectric layers and vacuum. With this approach, the effective surface impedance on the upper side of the HTS thin film is equal to the input impedance of the line model, and the effective surface resistance of different systems of layers (thicknesses, conductivity, quantity) can directly be investigated [20].

With the transmission line model, the surface resistances for four systems of layers as depicted in Fig. 3.5 have been investigated at a frequency of 2 GHz and for temperatures between 20–90 K. The superconducting material in all systems is $YBa_2Cu_3O_{7-\delta}$ (YBCO) which has a transition temperature of $\sim$92 K. The normal

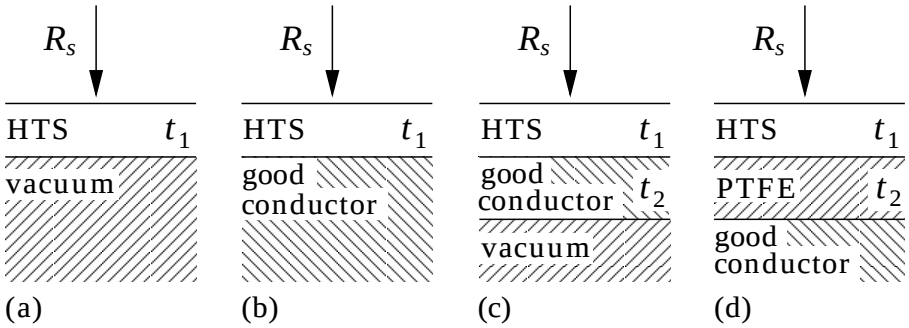

Figure 3.5: Four with respect to the surface resistance investigated systems of layers (last layers infinitely thick).

conducting material is copper[§]. In the last system a layer of PTFE[¶] is introduced to isolate the superconductive from the normal conductive layer, but there is no difference if other low loss dielectrics or vacuum are used instead.

The first system is the trivial case of HTS thin films in front of vacuum. As no other lossy materials are present, this case gives the lowest surface resistance and serves as standard for comparisons. Fig. 3.6 (a) shows results for $R_s(T)$ (20 K $\leq T \leq$ 90 K) obtained with the transmission line model for YBCO films between 50 nm and 1000 nm thick. For HTS films thicker than ∼500 nm the surface resistance is approximately the value of bulk material. For thinner films R_s increases significantly and is for extremely thin films ($\leq$ 50 nm) about ten times higher than for films of thicknesses $\geq$ 500 nm.

The observed higher surface resistance of thinner films is even greater if the HTS films are in front of a good normal conductor (e.g. copper) as the results shown in Fig. 3.6 (b) demonstrate (YBCO films with 50 nm $\leq t_1 \leq$ 1000 nm). In this case, the vacuum of the first structure (Fig. 3.5 (a)) has been replaced by an infinitely thick copper layer. The surface resistance for a 50 nm thick YBCO film is about 100 times higher than R_s for a 1000 nm thick film, and even the surface resistance for relatively thick films (e.g. 750 nm) is noticeably increased.

An interesting case is encountered if the second (metallic, e.g. copper) layer is not infinitely thick but rather thin. This case is depicted in Fig. 3.5 (c) where the metallic layer of thickness t_2 is followed by an infinitely thick layer of vacuum. As long as the metallic layer is not too thin (∼1000 nm), the same surface resistance as for an infinitely thick layer results. However, for thinner layers ($t_2 \leq$ 250 nm) the surface resistance increases. This increase is temperature dependant and stronger for thin HTS films. If the metallic layer is very thin ($t_2 \leq$ 50 nm), the monotonic increase of R_s with the temperature can change. This means that in case of an extremely thin metallic layer on top of a HTS layer the surface resistance can increase with decreasing temperature. This effect is especially strong for thin HTS films. Fig. 3.6 (c) shows the results of the transmission line model for the considered cases for 350 nm and 750 nm thick HTS films with 50 nm, 250 nm and 1000 nm thick copper layers.

The deleterious effect of the thin conductor can be avoided with the inclusion of an isolation layer between the HTS film and the normal conducting material as shown in Fig. 3.5 (d). The results of the transmission line model depicted in Fig. 3.6 (d) for 350 nm and 750 nm thick HTS films show that even with a thin dielectric layer similar surface resistances as shown in Fig. 3.6 (a) (YBCO–vacuum)

[§]Usually, silver or gold is used as contact layer, but copper is a good compromise with respect to the conductivity.

[¶]Polytetrafluoroethylene

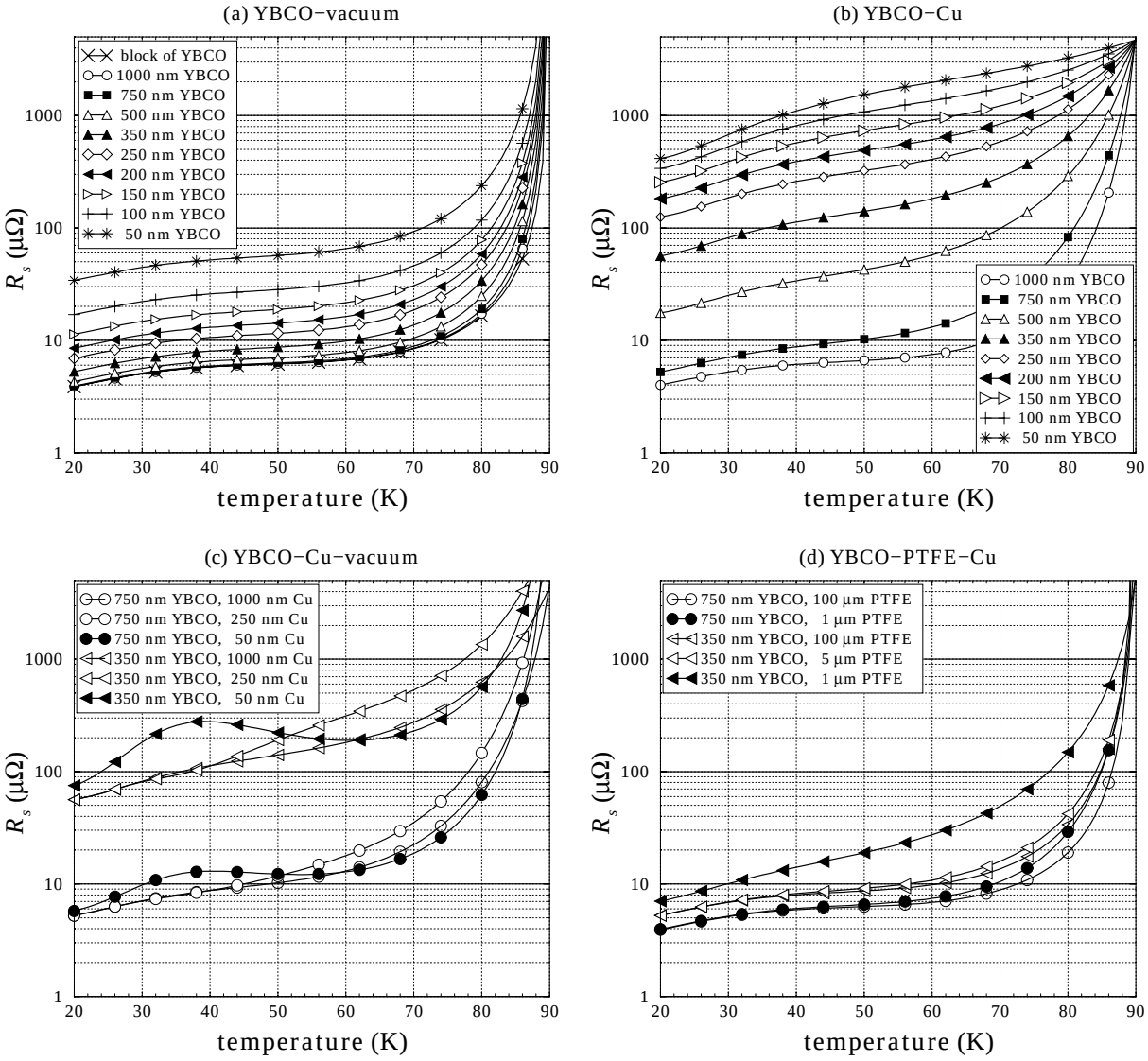

Figure 3.6: Modelled surface resistance for different systems of layers.

can be maintained. In case of 350 nm thick HTS films the isolation layer should be 5 μm or thicker, and in case of 750 nm thick HTS films the isolation layer should not be less than 1 μm thick.

As consequence of the results obtained by the transmission line model, the packaging of a microstrip structure as shown in Fig. 3.1 needs to be modified if highest quality factors are required. This is particularly advisable for devices fabricated from thin HTS films ($\leq$ 350 nm) on thin substrates ($\leq$ 0.5 mm). A proposed packaging for this case is shown in Fig. 3.7. Underneath the area of the HTS ground plane where high currents flow there should be no normal conducting material. Instead, an isolation layer (dielectric or vacuum) is introduced which may be kept thin ($\leq$ 5 μm). The whole structure can be fixed in the housing with a contact layer at the four edges of the ground plane. As there are no resonant

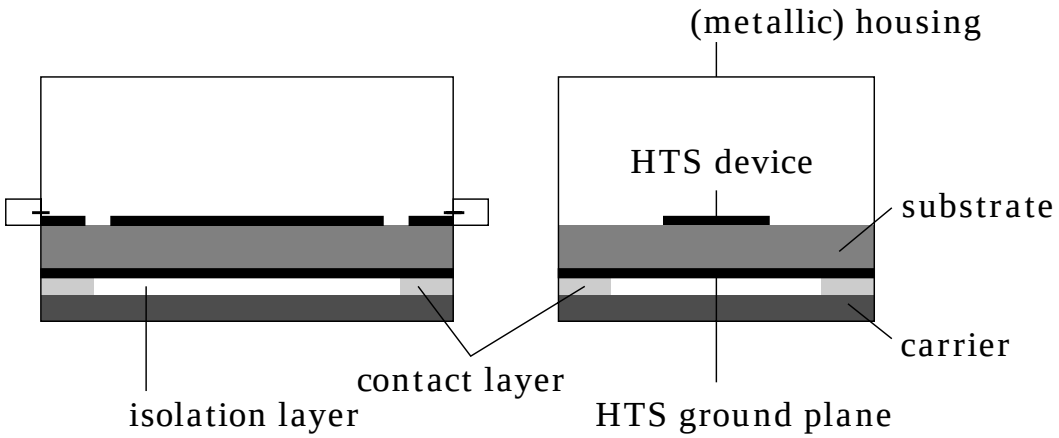

Figure 3.7: Proposed packaging for devices fabricated from thin HTS films on thin substrates.

currents present, this contact layer can be made of silver or gold.

Similar to losses in the ground plane, losses caused by a normal conducting housing cover have been investigated using full–wave simulation software. This investigation has been performed with the four resonator types shown in Fig. 3.2 assuming 0.5 mm thick $LaAlO_3$, 2 mm spacing between the substrate surface and the cover of the housing with a conductor surface resistance of $R_s = 12$ mΩ, and a resonant frequency of 2 GHz. The simulation results obtained for Q_h are summarised in table 3.2 and a comparison with the results for a lossy ground plane shows a similar pattern. The doubly–symmetric hairpin and the meander–line resonator are relatively immune to housing losses. In practice, this fact is of importance because housings are usually made of a normal counducting material and housing losses may exceed the losses in the ground plane. Additionally, the cover of the housing can be close to the microstrip structure to enable tuning.

Table 3.2: Housing quality factor Q_h for different resonator types with the same line width w = 0.8 mm.

resonator type	Q_h
microstrip section	56,300
hairpin	56,400
doubly–symmetric hairpin	110,000
meander–line	205,000

3.1.4 Analytic evaluation of losses in the housing cover

In the previous section, losses of a HTS resonator caused by a lossy housing cover have been investigated by the help of full–wave simulation software. However, with few approximations analytic expressions for such losses can be found. For this, a geometry as shown in Fig. 3.8 is considered. The figure depicts a metallic box with the measures $a \times b \times (c + h)$, assuming $a > b > (c + h)$. h denotes the thickness of the substrate. The current density $\mathbf{J}(x, y)$ in the plane $z = 0$ represents the surface current density of an arbitrary planar resonator at the resonant frequency. The side walls of the box are considered as ideally conductive, whereas for the top and bottom walls the surface impedances $Z_1 = R_1 + jX_1$ and $Z_2 = R_2 + jX_2$ may be introduced. These surface impedances at $z = c$ and $z = -h$ can be transformed into impedances Z_{t1} and Z_{t2} in the plane $z = 0$.

With this approach, losses in the two housing walls considered can be represented by an effective surface resistance R_{eff} in the plane $z = 0$. Taking Eqn. (3.10) into consideration, a planar resonator with the current density distribution $\mathbf{J}(x, y)$ at $z = 0$ dissipates the power

$$P_{dis} = \frac{1}{2} R_{eff} \int_S |\mathbf{J}(x, y)|^2 \, dS \quad = \quad \frac{1}{2} R_{eff} \, |I|^2. \tag{3.15}$$

According to this, R_{eff} is directly comparable to the surface resistance R_s of superconducting material. In order to avoid housing losses, R_{eff} has to be smaller than R_s of the resonator material. On the other hand, it was shown in the previous section that housing losses depend on the resonator geometry (or $\mathbf{J}(x, y)$ accordingly). As consequence, R_{eff} has to be derived from $\mathbf{J}(x, y)$.

For this, the waveguide eigenmodes excited by $\mathbf{J}(x, y)$ at $z = 0$ may be

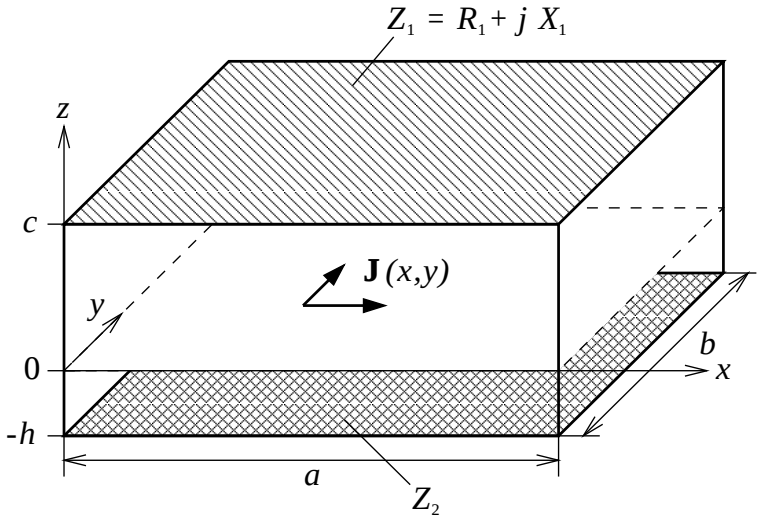

Figure 3.8: Rectangular housing with perfectly conducting side walls.

considered. These modes are either transverse electric (TE_{mn}–modes) or transverse magnetic (TM_{mn}–modes) with respect to z. The coefficients of the excited modes for a given current density distribution are determined by

$$I_{mn}^{\mathrm{TE}} = \int_0^b \int_0^a \mathbf{J}(x,y) \cdot \mathbf{f}_{mn}^{\mathrm{TE}}(x,y)\, dxdy \tag{3.16}$$

$$I_{mn}^{\mathrm{TM}} = \int_0^b \int_0^a \mathbf{J}(x,y) \cdot \mathbf{f}_{mn}^{\mathrm{TM}}(x,y)\, dxdy \tag{3.17}$$

for TE_{mn}–modes and TM_{mn}–modes respectively. The normalised expansion functions $\mathbf{f}_{mn}^{\mathrm{TE}}(x,y)$ and $\mathbf{f}_{mn}^{\mathrm{TM}}(x,y)$ represent the transverse spatial distribution of the waveguide eigenmodes and build a complete orthonormal set of functions. For the geometry considered these expansion functions are derived in appendix A (see page 67).

The dissipated power of one TE_{mn} or TM_{mn} eigenmode caused by the current density distribution $\mathbf{J}(x,y)$ is given by

$$P_{dis,mn}^{\mathrm{TE}} = \frac{1}{2}\, R_{eff,mn}^{\mathrm{TE}}\, |I_{mn}^{\mathrm{TE}}|^2, \tag{3.18}$$

$$P_{dis,mn}^{\mathrm{TM}} = \frac{1}{2}\, R_{eff,mn}^{\mathrm{TM}}\, |I_{mn}^{\mathrm{TM}}|^2. \tag{3.19}$$

Making use of the orthogonality, the total dissipated power is given by

$$P_{dis} = \frac{1}{2} \sum_m \sum_n \left(R_{eff,mn}^{\mathrm{TE}}\, |I_{mn}^{\mathrm{TE}}|^2 + R_{eff,mn}^{\mathrm{TM}}\, |I_{mn}^{\mathrm{TM}}|^2 \right). \tag{3.20}$$

With

$$\sum_m \sum_n \left(|I_{mn}^{\mathrm{TE}}|^2 + |I_{mn}^{\mathrm{TM}}|^2 \right) = |I|^2 \tag{3.21}$$

and using Eqn. (3.15), the effective surface resistance R_{eff} in the plane $z = 0$ becomes

$$R_{eff} = \frac{\sum_m \sum_n \left(R_{eff,mn}^{\mathrm{TE}}\, |I_{mn}^{\mathrm{TE}}|^2 + R_{eff,mn}^{\mathrm{TM}}\, |I_{mn}^{\mathrm{TM}}|^2 \right)}{\sum_m \sum_n \left(|I_{mn}^{\mathrm{TE}}|^2 + |I_{mn}^{\mathrm{TM}}|^2 \right)}. \tag{3.22}$$

In order to compute R_{eff} for a given current density distribution $\mathbf{J}(x,y)$, the current coefficients I_{mn}^{TE} and I_{mn}^{TM} have to be determined with Eqn. (3.16) and (3.17). The effective surface resistances $R_{eff,mn}^{\mathrm{TE}}$ and $R_{eff,mn}^{\mathrm{TM}}$ can be derived from the

transformed impedances Z_{t1} and Z_{t2} at $z = 0$. For a perfectly conducting ground plane ($Z_2 = 0$) and $\varepsilon_{r1} = 1$ they may be approximated to

$$R^{\mathrm{TE}}_{eff,mn} \approx \left(\frac{k_{z1,mn} \tan\left(k_{z2,mn} h\right)}{k_{z1,mn} \tan\left(k_{z2,mn} h\right) + k_{z2,mn} \tan\left(k_{z1,mn} c\right)} \right)^2 \frac{R_1}{\cos^2\left(k_{z1,mn} c\right)} \tag{3.23}$$

$$R^{\mathrm{TM}}_{eff,mn} \approx \left(\frac{k_{z2,mn} \tan\left(k_{z2,mn} h\right)}{k_{z2,mn} \tan\left(k_{z2,mn} h\right) + \varepsilon_{r2} k_{z1,mn} \tan\left(k_{z1,mn} c\right)} \right)^2 \frac{R_1}{\cos^2\left(k_{z1,mn} c\right)}. \tag{3.24}$$

The derivation of these approximations are given in appendix B. R_1 is the surface resistance of the housing cover, ε_{r2} is the permittivity of the substrate material, $k_{z1,mn}$ and $k_{z2,mn}$ are the wave numbers of the individual eigenmodes given by

$$k_{z1,mn} = \sqrt{\left(\frac{2\pi}{\lambda_0}\right)^2 - \left(\frac{m\pi}{a}\right)^2 - \left(\frac{n\pi}{b}\right)^2} \tag{3.25}$$

$$k_{z2,mn} = \sqrt{\varepsilon_{r2}\left(\frac{2\pi}{\lambda_0}\right)^2 - \left(\frac{m\pi}{a}\right)^2 - \left(\frac{n\pi}{b}\right)^2}. \tag{3.26}$$

Noting that the wave numbers $k_{z1,mn}$ and $k_{z2,mn}$ may be real or imaginary depending whether the associated eigenmode is propagating. However, (3.23) and (3.24) are real values in any case and depend besides the frequency on geometric and material parameters only.

Considering the dependence of (3.23) and (3.24) on the substrate thickness h, we find that the loss contribution of a lossy housing cover can be reduced with thin substrates. If higher modes are disregarded and $k_{z2,mn} h \ll 1$ is assumed so that $\tan\left(k_{z2,mn} h\right) \approx k_{z2,mn} h$, the effective surface resistance R_{eff} is approximately proportional to h^2. On the other hand, it was shown in section 3.1.1 that the conductor losses of a HTS microstrip resonator increases if the substrate thickness is reduced. This gives a lower limit for h therefore.

For not propagating modes and $\varepsilon_{r2} > 1$ we can conclude from (3.25) and (3.26) that $k_{z1,mn} > k_{z2,mn}$ and from this $R^{\mathrm{TE}}_{eff,mn} > R^{\mathrm{TM}}_{eff,mn}$ yields. Furthermore, for high permittivity substrates ($\varepsilon_{r2} \gg 1$) we find $R^{\mathrm{TE}}_{eff,mn} \gg R^{\mathrm{TM}}_{eff,mn}$. Thus, Eqn. 3.22 can be reduced to

$$R_{eff,h} \approx \frac{\sum_m \sum_n \left(R^{\mathrm{TE}}_{eff,mn} \left| I^{\mathrm{TE}}_{mn} \right|^2 \right)}{\sum_m \sum_n \left(\left| I^{\mathrm{TE}}_{mn} \right|^2 + \left| I^{\mathrm{TM}}_{mn} \right|^2 \right)}, \tag{3.27}$$

neglecting the loss contributions of all TM_{mn}–modes.

To give a numerical example, we consider a housing with $a = 30$ mm, $b = 15$ mm, and $c = 3$ mm. The substrate thickness is $h = 0.5$ mm and the permittivity $\varepsilon_{r2} = 24$. For $f = 2$ GHz the evaluation of (3.23) and (3.24) gives

$$\max(R^{\mathrm{TE}}_{eff,mn}) = R^{\mathrm{TE}}_{eff,10} \approx 2.0 \cdot 10^{-2} \cdot R_1 \tag{3.28}$$

and

$$\max(R^{\mathrm{TM}}_{eff,mn}) = R^{\mathrm{TM}}_{eff,12} \approx 1.6 \cdot 10^{-5} \cdot R_1. \tag{3.29}$$

Thus (3.27) has been validated. For higher modes, the values of $R^{\mathrm{TE}}_{eff,mn}$ decrease rapidly with increasing order. For $m = 15, n = 0$ we find an already low value of $R^{\mathrm{TE}}_{eff,15\,0} \approx 5.1 \cdot 10^{-5} \cdot R_1$, and for $m = 0, n = 10$ we get $R^{\mathrm{TE}}_{eff,0\,10} \approx 2.7 \cdot 10^{-6} \cdot R_1$. Therefore, all modes with either $m > 15$ or $n > 10$ can safely be neglected.

With (3.16) and (3.17) the coefficients I^{TE}_{mn} and I^{TM}_{mn} have been computed for a microstrip line section resonator and a meander–line resonator respectively (see Fig. 3.2). To do so, the current density distributions along both resonators have been approximated with cosine functions. The edge current crowding has not been taken into account, but a constant density distribution across the resonator width $w = 1$ mm was assumed. Furthermore, $R_1 = R^{\mathrm{Cu}}_s$ was substituted to represent a housing cover made of copper. For the microstrip line section resonator

$$R_{eff} = 3.8 \cdot 10^{-3} \cdot R^{\mathrm{Cu}}_s \tag{3.30}$$

was computed, and for the meander–line resonator

$$R_{eff} = 0.13 \cdot 10^{-3} \cdot R^{\mathrm{Cu}}_s \tag{3.31}$$

respectively. On the other hand, for $f = 2$ GHz and $T = 60$ K the surface resistance of YBCO thin films is about three orders of magnitude less than that of copper, that is

$$R^{\mathrm{YBCO}}_s \approx 1 \cdot 10^{-3} \cdot R^{\mathrm{Cu}}_s. \tag{3.32}$$

Therefore, the transformed effective surface resistance R_{eff} of a microstrip line section resonator is about four times higher than that of YBCO thin films for the housing geometry and substrate parameters considered. Hence, the unloaded quality factor Q_0 may significantly be reduced. For the meander–line resonator, $R_{eff} \ll R^{\mathrm{YBCO}}_s$ has been found, and in this case Q_0 is not limited by Q_h. These results are in good agreement with the full–wave simulation results presented in table 3.2.

3.2 Attainable unloaded quality factor

After the different loss contributions have been considered separately, the next question is what is the maximum unloaded quality factor Q_0 that can be achieved with a microstrip resonator when all loss contributions are present.

The upper limit of Q_0 for given geometric and material parameters is given by Eqn. (3.9) which is rewritten here as

$$Q_c = \frac{\pi\ Z_0}{\lambda_0}\ \frac{l_c}{R_s}. \tag{3.33}$$

For microstrip resonators, the geometric parameter l_c is limited by the inhomogenity of the current distribution (edge current crowding), which depends on the line width w and on the substrate height h. A theoretical upper limit for l_c is obtained if $w \gg h$ and homogeneous current distribution is assumed. For this case, $l_c \approx h$ results. On the other hand, in case of $w \ll h$ (e.g. for lumped element inductors) the lower limit for l_c is given by $l_c \approx w$.

For the microstrip resonator types (see Fig. 3.2) previously discussed the geometric parameter can be assumed to be in the range 0.05 mm $\leq l_c \leq$ 0.2 mm (for 0.2 mm $\leq w \leq$ 1 mm and 0.25 mm $\leq h \leq$ 1 mm). For this range of l_c and a temperature dependant surface resistance as given in Fig. 3.6 (upper left hand side) the maximimum quality factor Q_c of microstrip resonators fabricated from YBCO thin films can be estimated. Results of such an estimation for 350 nm and 750 nm thick YBCO films are shown in Fig. 3.9 ($f_0 \approx$ 2 GHz). For both film thicknesses, Q_c has been evaluated for two geometric parameters l_c (0.05 mm and 0.2 mm respectively) and temperatures between 30 K and 90 K. As expected, the highest quality factors are obtained for the thicker film and l_c = 0.2 mm, and the lowest for the thinner film and l_c = 0.05 mm. At 77 K, Q_c is between ~15,000 and ~100,000, and at 30 K Q_c is between ~60,000 and ~300,000.

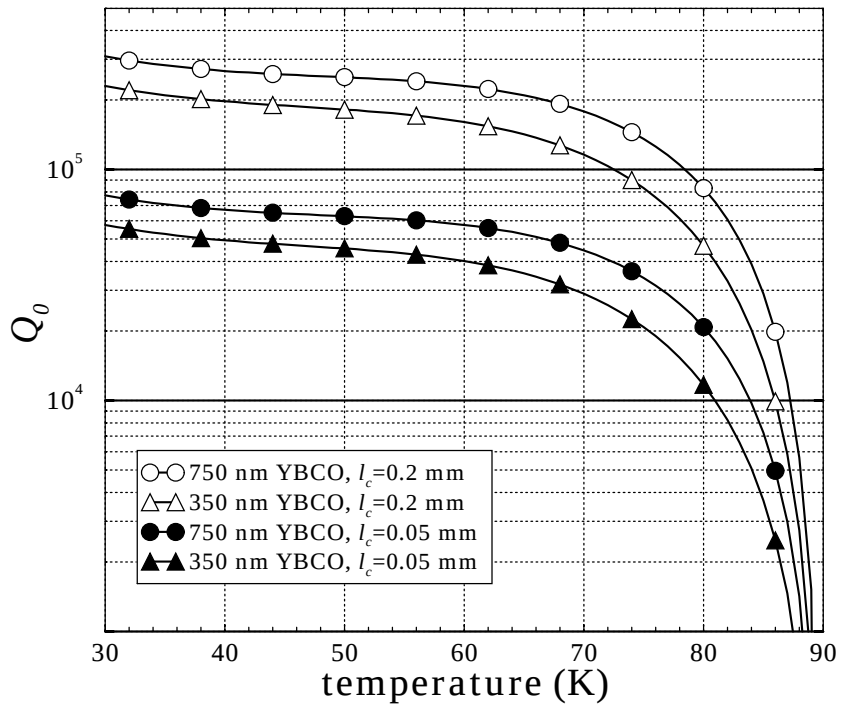

Figure 3.9: Estimated quality factor Q_c for microstrip resonators ($f_0 \approx$ 2 GHz) with l_c = 0.2 mm (open symbols) and l_c = 0.05 mm (closed symbols) made out of 350 nm (triangles) and 750 nm (circles) YBCO films.

A further estimation for the overall unloaded quality factor Q_0 of a microstrip resonator is obtained if the other loss contributions (see Eqn. (3.4)) are assumed to be temperature independent ($Q = Q_{const}$). With this approximation, Q_0 for different values of Q_{const} can be evaluated for the four different cases of Q_c from above. The results of such estimations for different values of Q_{const} are shown in Fig. 3.10. It is clear that Q_{const} has to be as high as possible to maximise Q_0, but the curves shown in the figure imply that values of $Q_{const} \geq$ 500,000 are acceptable for all four cases.

On the other hand, lanthanum aluminate has been widely used as substrate material for planar HTS applications, and it has been shown [15] that its loss

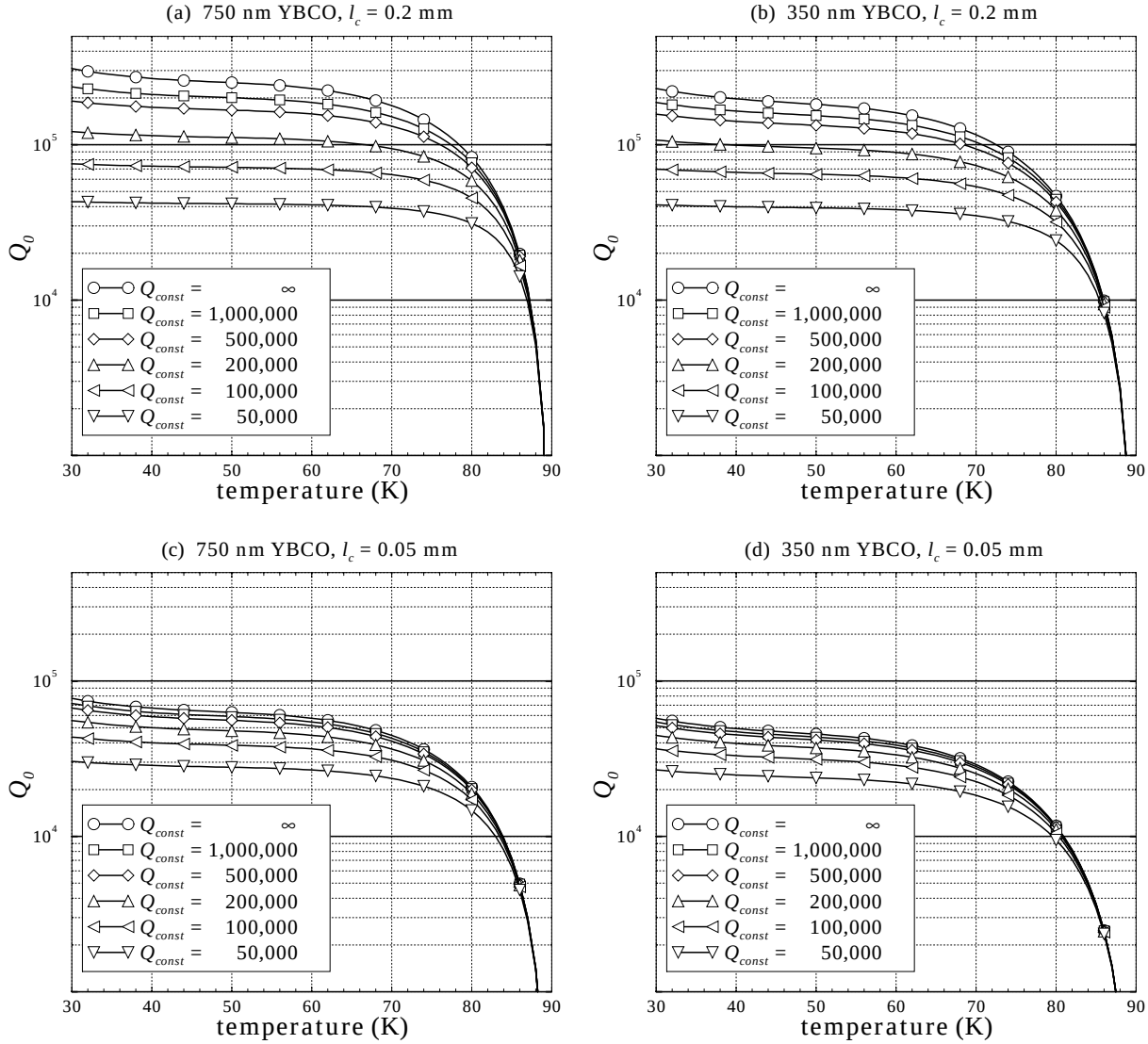

Figure 3.10: Estimations for the unloaded quality factor of a HTS microstrip resonator ($f_0 \approx$ 2 GHz) in case of an additional temperature independent quality factor Q_{const}: (a) 750 nm thick YBCO, geometric parameter l_c = 0.2 mm, (b) 350 nm YBCO, l_c = 0.2 mm, (c) 750 nm YBCO, l_c = 0.05 mm, (d) 350 nm YBCO, l_c = 0.05 mm.

tangent can strongly be temperature dependant. Some $LaAlO_3$ crystals with a relatively low loss tangent at cryogenic temperatures have been found, but most of the commonly used $LaAlO_3$ substrates are cut from crystals with a loss tangent maximum between ∼60 K and 100 K (depending on the frequency). In [21], this effect was demonstrated with high–Q HTS disk resonators, where substrates from different crystals and suppliers were used to fabricate the devices. However, at the time of writing a satisfactory explanation (e.g. growing method or optical appearance) to distinguish low loss tangent $LaAlO_3$ crystals from those with the loss tangent maximum has not been published.

The lanthanum aluminate material from which the resonators and filters presented in this work (see page 45) were fabricated possessed the higher loss tangent at cryogenic temperatures. As an example, on the left hand side of Fig. 3.11 the measured loss tangent of the $LaAlO_3$ samples is shown for temperatures between 30 K and 90 K (taken from reference [15]). The loss tangent can be transformed into the quality factor Q_d through Eqn. (3.14)[‖]. If this Q_d is then combined with the Q_c's shown in Fig. 3.9, a common quality factor Q_f for YBCO thin films on (lossy) $LaAlO_3$ substrates is obtained. Good YBCO films on $LaAlO_3$ substrates are usually ≥700 nm thick, and therefore only the 750 nm curves in Fig. 3.9 for l_c = 0.05 mm and 0.2 mm have been considered further. Q_d and the combination of Q_d with the two Q_c's are shown in Fig. 3.11 on the right hand side. It can be clearly seen that the losses in the substrate material reduces the quality factor Q_f, particularly between ∼50 K and ∼75 K, and both Q_f's are dominated by

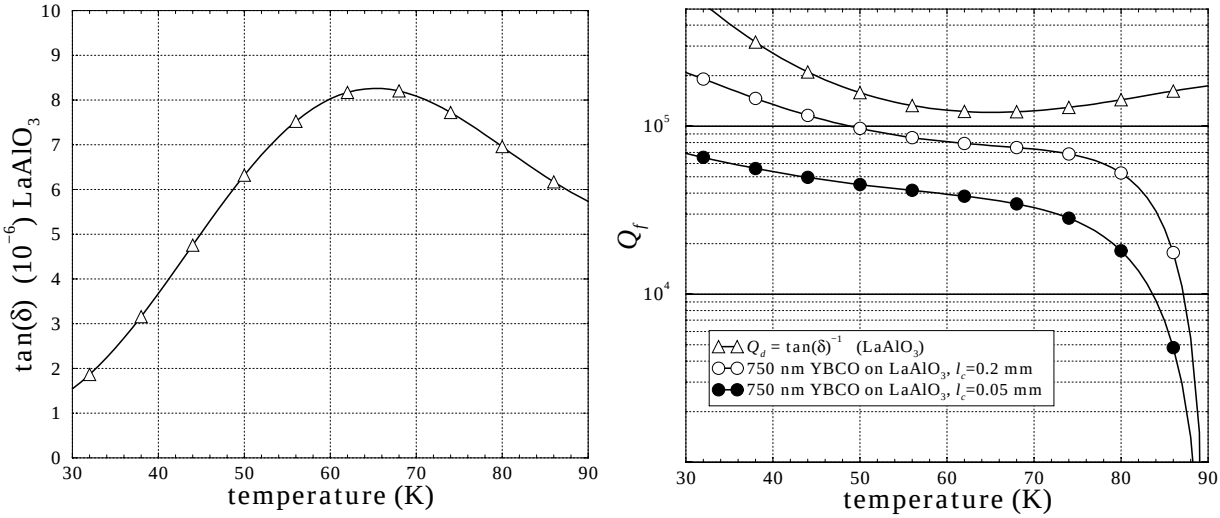

Figure 3.11: Approximated loss tangent for specific $LaAlO_3$ substrates (left), Q_d and the resulting quality factors Q_f for 750 nm YBCO films (f = 2 GHz) on these substrates for l_c = 0.05 mm and 0.2 mm (right).

[‖] $\beta_d \approx 1$ can be assumed as $LaAlO_3$ is a high permittivity material

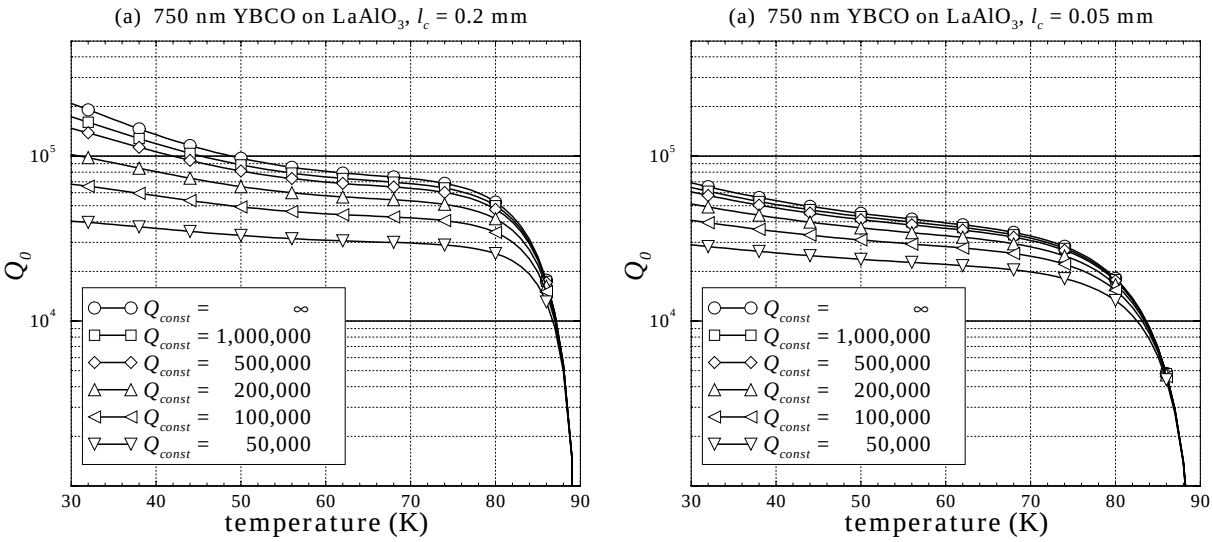

Figure 3.12: Theoretical Q_0 for HTS microstrip resonators (YBCO on $LaAlO_3$) with l_c = 0.2 mm (left) and l_c = 0.05 mm (right).

the loss tangent of the $LaAlO_3$.

The overall quality factor Q_0 for additional temperature independent loss contributions (Q_{const}) can be evaluated for both of the foregoing Q_f's. On the left hand side of Fig. 3.12 the theoretical Q_0 for YBCO microstrip resonators with l_c = 0.2 mm is shown, and on the right hand side of the figure for resonators with l_c = 0.05 mm. Again, quality factors $Q_{const} \geq$ 500,000 are acceptable.

Chapter 4

Measurement Set–Ups

The characteristics of linear multiport networks at microwave frequencies are usually expressed in terms of reflection and transmission coefficients which are known as scattering parameters (S–parameters). These S–parameters can easily be measured with modern measurement equipment such as vector network analysers with S–parameter test sets. The following sections describe briefly how the measured results presented in chapter 5 were obtained.

4.1 Measurement of the scattering parameters of a two–port device

With the wave coefficients a_j (incident waves) and b_i (reflected and transmitted waves) the S–parameters are given by

$$S_{ij} = \frac{b_i}{a_j}. \tag{4.1}$$

The case $i = j$ denotes the reflection coefficient for port i, and the case $i \neq j$ the transmission coefficient between port i and j. In the latter case, forward and reverse transmission must be distinguished. With a modern vector network analyser, all four S–parameters of a two–port device can be measured directly with a set–up as shown in Fig. 4.1. As only the characteristics of the device under test (DUT) are wanted, the cables between the analyser and the DUT have to be taken into account by calibrating the set–up for the required frequency range. However, if a HTS device is to be measured, the actual measurement is performed at cryogenic temperatures whereas the calibration is usually carried out at room temperature. This leads to a slight calibration error and consequently to a measurement error. In all measurements such errors have been observed as an increase of the magnitude of the S–parameters by $\sim$0.1 dB or less. To avoid these systematic errors, the

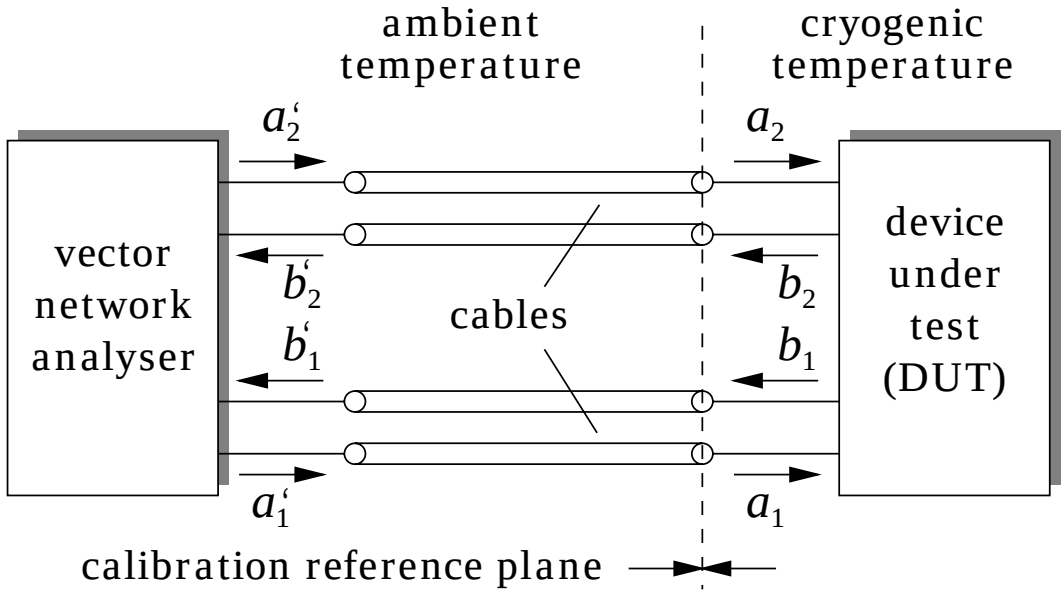

Figure 4.1: Principle measurement set–up for two–port S–parameter measurement of HTS devices with a vector network analyser.

calibration must be done at cryogenic temperatures as well, but to do so requires a relatively costly set–up which was not available for these measurements.

All measured HTS resonators and filters are passive, reciprocal low loss devices. Consequently, the relationships

$$S_{21} = S_{12} \tag{4.2}$$

$$|S_{11}|^2 + |S_{21}|^2 \leq 1 \tag{4.3}$$

$$|S_{22}|^2 + |S_{12}|^2 \leq 1 \tag{4.4}$$

can be deduced. In chapter 5, the terms reflection and transmission are used as synonyms for the magnitude of S_{11} and S_{21} respectively.

4.2 Measurement of the resonator quality factor

Usually, the unloaded quality factor Q_0 of resonators cannot be directly measured but has to be derived from the measured parameters. For this, two different measurement methods may be used; one–port or two–port measurement. With a vector network analyser, the one–port measurement is very easy to perform and has been used to obtain the results presented in chapter 5. A two–port measurement is advantageous if the external quality factor Q_{ext} of both ports is equal. In this case, only the magnitude of the transmission has to be measured to determine Q_0, and this can be done with very simple measurement equipment.

As the one–port case has been used for the measurement, only this method is discussed further. More detailed information about two–port measurements can be found in [22].

Fig. 4.2 shows the equivalent circuit of a lossy shunt resonator and the magnitude of the reflection coefficient of a one–port measurement. The unloaded quality factor Q_0 of the resonator is given by

$$Q_0 = \frac{R}{Z_c}, \tag{4.5}$$

and the external quality factor Q_{ext} which denotes the part of the oscillating power distributed to the external load Z of the set–up is given by

$$Q_{ext} = \frac{Z}{Z_c} \tag{4.6}$$

where $Z_c = \sqrt{L/C}$ is the characteristic impedance of the resonator. Q_0 and Q_{ext} are related to the loaded quality factor Q_l by

$$\frac{1}{Q_l} = \frac{1}{Q_0} + \frac{1}{Q_{ext}}. \tag{4.7}$$

From the measured reflection coefficient S_{11}, Q_l can directly be determined from

$$Q_l = \frac{f_2 - f_1}{f_0}. \tag{4.8}$$

The frequencies f_1 and f_2 are the half power points which can be found from

$$|S_{11}(f_{1,2})|^2 = \frac{|S_{11}(f_0)|^2 + 1}{2}. \tag{4.9}$$

To determine the unloaded quality factor, three cases have to be distinguished:

(a) $Q_{ext} > Q_0$ (under coupled)

(b) $Q_{ext} = Q_0$ (critically coupled)

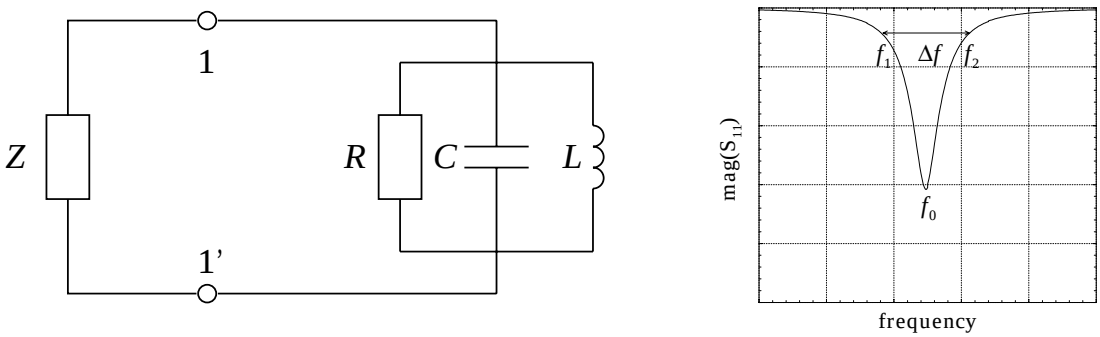

Figure 4.2: Equivalent circuit of a shunt resonator for one–port measurements (left), and magnitude of the reflection (right).

(c) $Q_{ext} < Q_0$ (over coupled)

Using a vector network analyser, it is easy to determine which of the three cases exists. Fig. 4.3 illustrates these cases, on the left hand side, the magnitudes of the reflection coefficents are shown, and on the right hand side the Smith chart plot. In case of a critical coupling, the respective circular curve passes through the centre point of the Smith chart. For an over coupling, this point is included by the curve, whereby for an under coupling the point is excluded. From this information, Q_0 and Q_{ext} can be calculated. For the under coupled case ($Q_{ext} > Q_0$) the Q's become

$$Q_0 = \frac{2\,Q_l}{1 + |S_{11}(f_0)|} \tag{4.10}$$

$$Q_{ext} = \frac{2\,Q_l}{1 - |S_{11}(f_0)|}. \tag{4.11}$$

For the critical case

$$Q_0 = Q_{ext} = 2\,Q_l \tag{4.12}$$

results, and finally the over coupled case ($Q_{ext} < Q_0$) gives

$$Q_0 = \frac{2\,Q_l}{1 - |S_{11}(f_0)|} \tag{4.13}$$

$$Q_{ext} = \frac{2\,Q_l}{1 + |S_{11}(f_0)|}. \tag{4.14}$$

For a strongly over coupled resonator ($Q_{ext} \ll Q_0$) the error for Q_0 may become large as $|S_{11}| \approx 1$ in (4.13). This case should be therefore avoided.

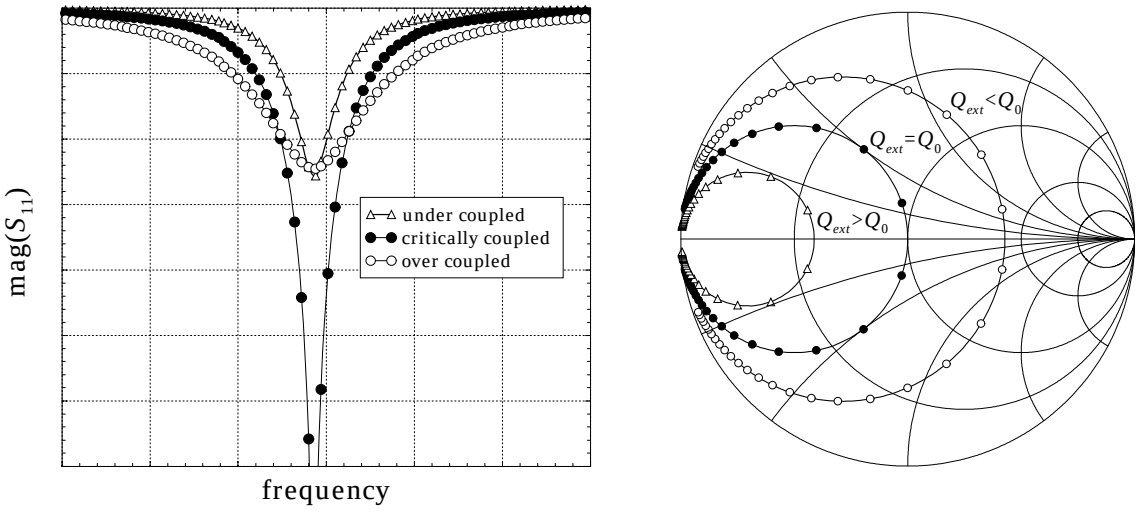

Figure 4.3: Illustration of under, over and critical coupling of a resonator: magnitudes of reflections (left) and Smith chart (right).

4.3 Intermodulation measurement set–up

All RF devices (passive or active) become nonlinear if a specific input power level is exceeded, and specifications for this characteristic have to be defined to ensure the function of a specific system or sub–system. This can be done by specifying a minimum signal–to–intermodulation level for a particular input power, or by the intercept point (both specifications are equivalent).

RF devices in microstrip technology have limited power handling capability because of the enhanced edge current density. With HTS materials this is excerbated as the superconductivity effect breaks down if the critical current density J_c is exceeded. Therefore, a HTS microstrip device becomes nonlinear at a relatively low power level.

The nonlinear behavior of a microwave device can be characterised using a two–tone measurement. In Fig. 4.4, a set–up for such a measurement is shown. The output of two sources with different frequencies f_1 and f_2 are fed to the device under test (DUT). With a spectrum analyser the output spectrum of the DUT is observed. If the DUT is linear, only the two frequencies of the sources will be detected. In the nonlinear case however, harmonics at the frequencies $n \cdot f_1$ and $n \cdot f_2$ as well as intermodulation products emerge. Attention has to be paid to the third order products at the frequencies $2f_1 - f_2$ and $2f_2 - f_1$ as these frequencies are very close to the frequencies f_1 and f_2. In an RF system, this may lead to nonlinear distortions of other signals. As example, the input and output spectra of a nonlinear device in a two–tone measurement are depicted in Fig. 4.5. The output power P_{out} of the fundamental frequencies (f_1, f_2) and the third order intermodulation products can be determined as function of the input power P_{in} of the two sources. Theoretically, the gradient of the fundamental is one, and of the intermodulation it is three, if saturation effects are negligible.

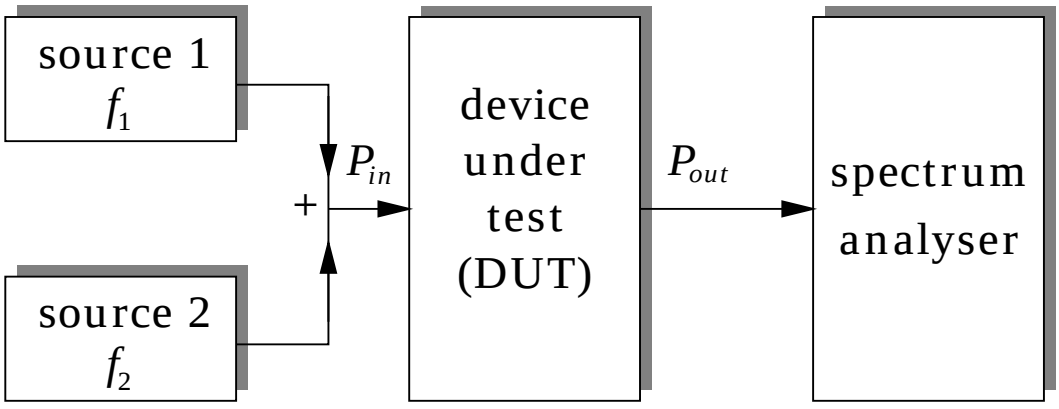

Figure 4.4: Principle measurement set–up for two–tone measurements.

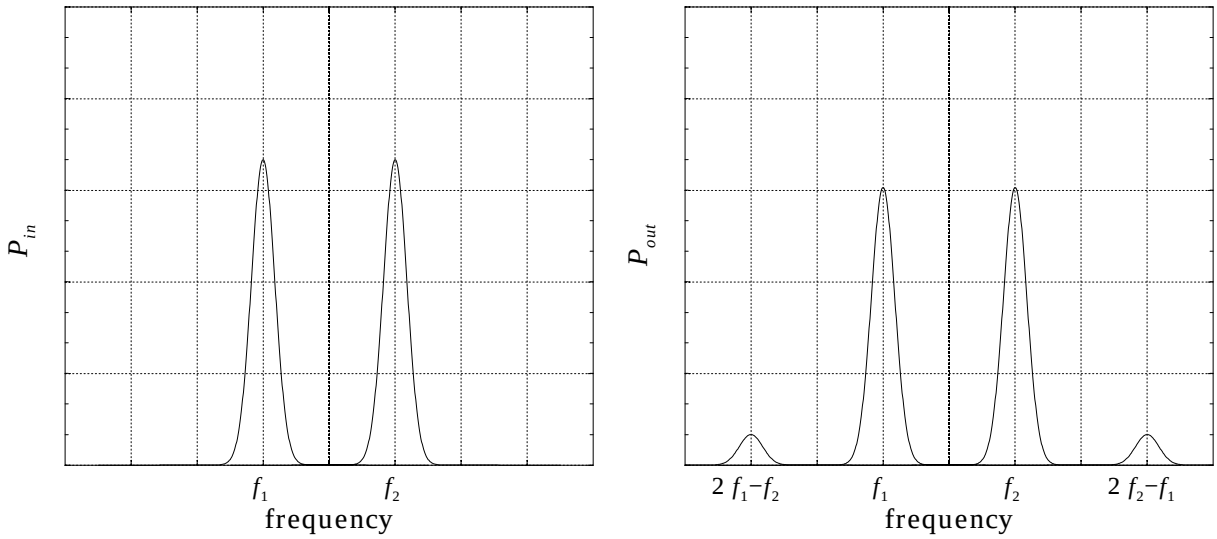

Figure 4.5: Two–tone measurement spectra of nonlinear devices: input spectrum (left) and output spectrum (right).

Because of the different gradients the two linear curves intersect, and the point of intersection is called third order intercept point (IP3). This point is a theoretical one, as saturation effects distort the linear curves as shown in Fig. 4.6. However, for a given input power the signal–to–intermodulation level can be determined if the intercept point of a device is known. These relations are illustrated in Fig. 4.6.

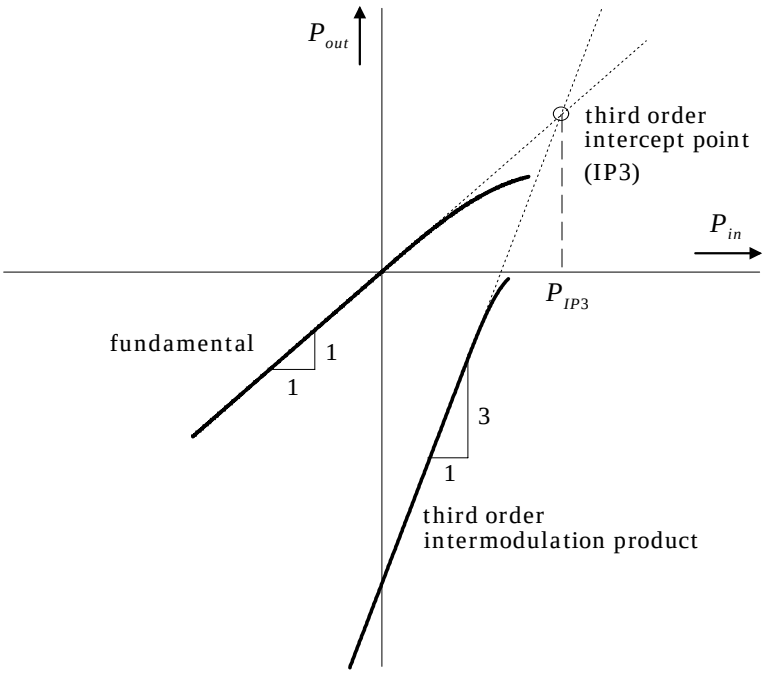

Figure 4.6: Definition of the third order intercept point IP3.

Chapter 5

Experimental Results for HTS Resonators and Filters

This chapter introduces experimental results for the unloaded quality factors of HTS microstrip resonators as well as measured results of various HTS bandpass filters.

In the first part, the fabrication of the HTS resonators and filters is briefly described. Then, the theoretical investigation of the unloaded quality factor, presented in chapter 3, for different resonator geometries is verified. It will be shown that both the novel doubly–symmetric resonator and the meander–line resonator are less sensitive to packaging losses than e.g. a hairpin resonator. The second part describes the developed HTS bandpass filters which either consist of doubly–symmetric resonators or of meander–line resonators. These filters have been developed for applications where high selectivity is required, as might be the case for future mobile communication systems where interference sets performance limitations, e.g. in the receiver front–end of the base transceiver stations (BTS). Filters with extremely steep skirts but with low pass–band insertion loss can help to overcome the limitations.

5.1 Resonator and filter fabrication

The fabrication of HTS microstrip resonators and filters requires a compatible substrate. Thin film deposition of HTS material onto both sides of a polished substrate can be performed with various methods, e.g. sputtering (DC or RF), co–evaporation, or laser ablation.

The coated substrates used here were produced by thermal reactive co–evaporation of YBCO thin films onto both sides of $LaAlO_3$ substrates [23]. Such coated substrates are generally of high quality and available in large quantities

and sizes up to 9 inches in diameter [24]. The substrate material $LaAlO_3$ has the advantage that relatively thick YBCO films (700 nm–800 nm) can be deposited compared to other standard compatible substrate materials such as CeO_2 buffered sapphire or MgO, where the YBCO film thickness is limited to approx. 350 nm. The drawbacks of $LaAlO_3$, i.e. twinning and loss tangent peak at 65 K, were observed in the experiments but turned out to be less critical in this application.

All measured resonators and filters were fabricated using standard photolithography and etching (wet chemical or ion milling) processes. The second side YBCO was metalised with 50–150 nm thick gold deposited in–situ for packaging the device. The $LaAlO_3$ substrates were specified to be 508 μm (= 0.020 inch) thick* and 2 inches in diameter. After the etching process, the filters and resonators were cut to size.

The 50 Ω feedlines of the filters required metallic contacts for interconnects, either for interfacing between substrates or to connectors (usually SMA/B/C or K–connectors). For this purpose, gold or silver contacts were deposited onto the end (2–3 mm) of the feedlines. Two different approaches were used:

(a) The contacts are made before the photolithography of the filter structure. For this, gold or silver is sputtered onto the whole HTS thin film, and after photolithography and etching only the contacts are left. The drawback of this procedure is that because of slightly nonhomogenous etching some gold spots remain scattered over the HTS thin film.

(b) The contacts are made after the etching of the filter structure with a shadow mask. For this, a thin metallic mask is required which covers the whole structure with openings for the deposition of the contacts. Mechanical tolerances of the mask are limitations of this approach.

With both methods good contacts were obtained, for silver as well as for gold. However, it was found that with the ultrasonic bonder (Marpet Enterprise Inc. 1204W and Uthe 10G ultrasonic controller) contacts with a thickness > 700 nm were required to achieve good bonds.

For the measurement of the filters the contacts of the feedlines were bonded to SMA connectors as shown in Fig. 5.1 on the left. The bond wires used were 25 μm in diameter. Either gold or aluminium wires could be used without changing the microwave properties of the connections. Measurements on test connections [25] showed that with three bond wires low loss as well as good matching between a coaxial connector and a 50 Ω microstripline could be achieved.

*Because of the required polishing prossess the thickness varied by ± 5 μm within one wafer and ± 10 μm for different wafers

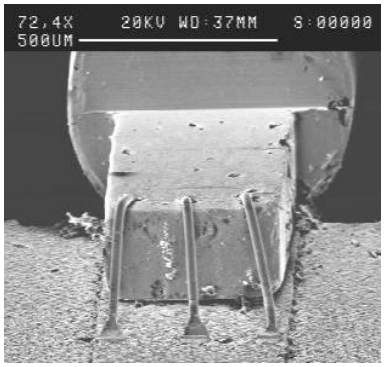

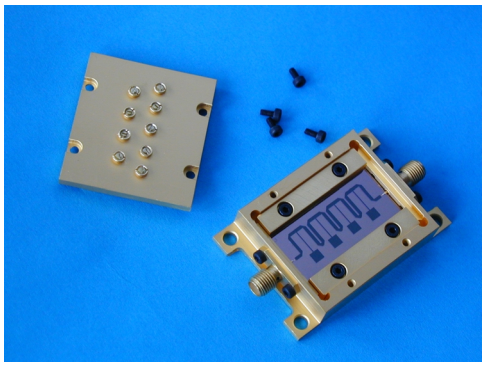

Figure 5.1: SEM image of a bonded connection between a microstrip feed line and an SMA connector with gold wires (left), assembled filter (right).

Some care has to be taken when a HTS filter or resonator is mounted into the housing, which is usually made of copper to obtain good electrical and thermal conductivity. Since the whole structure is assembled at room temperature (293 K) but is operated at cryogenic temperatures below 90 K, the device is exposed to high mechanical stress because of different thermal expansion coefficients of the components. Previous experiments showed that this stress is too high to bond devices made of $LaAlO_3$ substrates directly onto copper. Smaller devices ($< 5 \times 5$ mm) delaminated after few cooling cycles, and larger ones cracked. Thus, the devices have to be bonded onto carriers made of a material with a matching thermal expansion coefficient. For $LaAlO_3$ substrates, stainless steel and titanium were found to be appropriate carrier materials [26].

Because of this reason, all measured filters and resonators were mounted to gold plated steel or titanium carriers, which were than fixed in a copper housing using screws. On the right hand side of Fig. 5.1 an assembled filter is shown. Whereas for single resonators different packagings as shown in Fig. 3.5 were used in Q_0–measurements, all filters were directly bonded to carriers using silver loaded adhesive films[†] to achieve reproducible results.

5.2 Unloaded quality factors of HTS resonators

In order to verify the theoretical unloaded quality factors of HTS microstrip resonators (see page 34), single resonators were fabricated and tested. Besides the doubly–symmetric hairpin resonator a conventional hairpin and a meander–line resonator, with resonant frequencies of ∼1.8 GHz (Fig. 3.2 shows the layouts) were investigated for temperatures between 30 K and 85 K. Additionally, two different packaging methods were used to demonstrate the correlation between resonator

[†] Ablefilm® 5025E electrically conductive adhesive film

geometry and packaging losses.

All resonators were fabricated from YBCO thin films on 0.5 mm thick $LaAlO_3$ substrates. The YBCO film thickness was $\geq$750 nm and therefore relatively thick. The line width of the doubly–symmetric resonator and of the hairpin was w = 0.8 mm whereas the geometric parameters for the meander–line resonator were w = s = 0.48 mm. The same housing (inner measures 20 $\times$ 20 $\times$ 5 mm) was used for all measurements.

Firstly, the gold plated ground planes ($\sim$100 nm thick) of the resonators were mounted to the base of the housing with a poorly conductive epoxy adhesive. This packaging is comparable to a HTS – thin gold layer – vacuum system as shown in Fig. 3.5 (c). The results obtained for the unloaded quality factors of the three resonators and the packaging are shown in Fig. 5.2 (left). Although the line width (and therefore the geometric parameter l_c) of the doubly–symmetric and of the conventional hairpin are similar, the unloaded quality factor of the conventional hairpin resonator is limited to $\sim$60,000 (T = 30 K). By comparison, the maximum unloaded quality factor of the doubly–symmetric hairpin is $\sim$180,000 which is three times higher. The quality factors for higher temperatures ($T \geq$ 80 K) are similar, and unequal film qualities can be therefore excluded. The measured unloaded quality factors of the meander–line resonator and the doubly–symmetric hairpin resonator are similar.

The explanation for the different maximum unloaded quality factors of conventional and doubly–symmetric resonators is the different packaging losses. As predicted in the theoretical section (see Fig. 3.3), the conventional hairpin

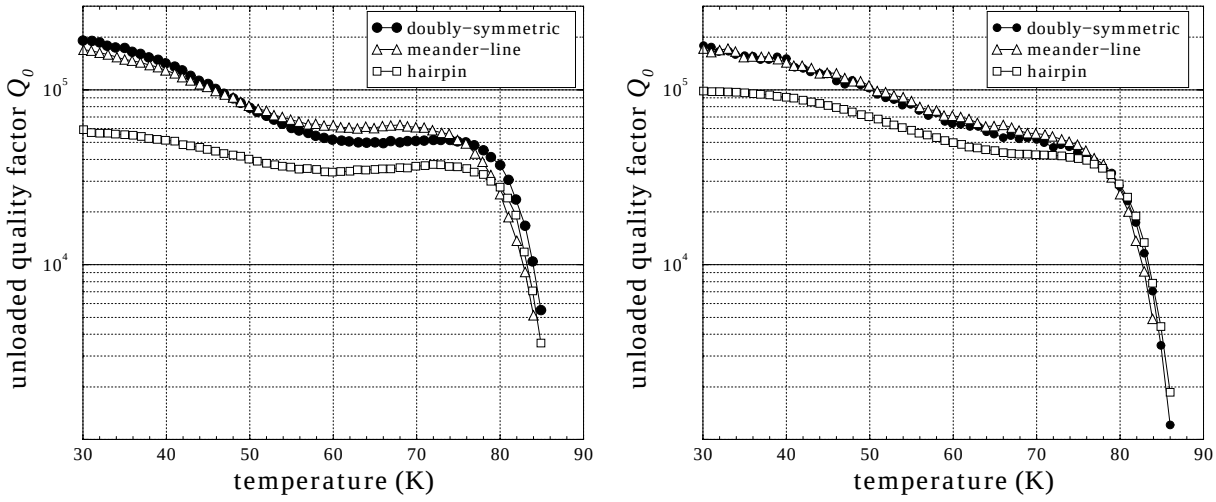

Figure 5.2: Measured unloaded quality factors Q_0 for doubly–symmetric hairpin, meander–line and conventional hairpin resonators ($f_0 \approx$ 1.8 GHz): HTS – thin gold layer – vacuum – housing (left), HTS – thin gold layer – Ablefilm – housing (right).

resonator is relatively sensitive to losses in the ground plane, and poor packaging reduces the maximum achievable unloaded quality factor.

Support to the latter statement is given by an improved packaging. When the gold plated ground planes of the resonators are bonded to the housing with an epoxy paste or film adhesive which has a good conductivity, higher unloaded quality factors are achieved. On the right hand side of Fig. 5.2, measured results of unloaded quality factors are shown for the same resonators, but with the improved packaging. In this case, the conventional hairpin resonator possesses a maximum quality factor of $\sim$100,000 which is a significant improvement. The other two resonators now possess a quality factor $\sim$1.8 times higher at T = 30 K. The difference is attributable to the higher losses in the housing walls and depends only on the resonator geometry (see Tab. 3.2 on page 30).

If the two graphs in Fig. 5.2 are compared, the influence of a poor packaging is also visible for the doubly–symmetric hairpin and for the meander–line resonator, although both resonator types are relatively insensitive to packaging losses and the thickness of the YBCO films used limited the influence of the ground plane (see Fig. 3.6 (c)). The poor packaging resulted in an almost constant quality factor between 55 K and 75 K. However, these temperatures are usual operating temperatures for HTS devices. To obtain reliable, reproducible and high quality factors, a good packaging must be provided for any HTS device.

5.3 Bandpass filters

In this section, several bandpass filters are discussed. Most of the filters developed are based on the novel doubly–symmetric hairpin resonator. To demonstrate and verify the unique coupling scheme (couplings of different natural phases) of this resonator type as described in section 2.4.2, measured results of two–pole test filters are presented.

5.3.1 Two–pole test filters

To verify the unique coupling scheme of two novel doubly–symmetric hairpin resonators, two test filters as shown in Fig. 5.3 were fabricated and measured. As already discussed in section 2.4.2, both filters are similar with the exception that one of the resonators in the second filter is mirrored (upper resonator in filter (b)). Additionally, the two filters included sapphire tuning screws as shown in Fig. 2.12 in order to demonstrate the coupling coefficient tuning capability.

Fig. 5.4 depicts the experimental results at T = 77 K for the test filters (left–hand side magnitude of the transmission coefficients, right–hand side phase).

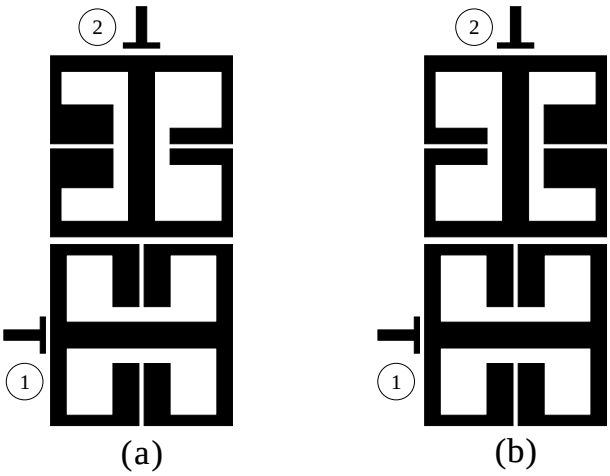

Figure 5.3: Test structures to demonstrate negative and positive coupling capability of two doubly–symmetric hairpin resonators.

Firstly, the filters were tuned to have a strong coupling, and then to have a weak coupling. In the strong coupling case (open and closed circles in Fig. 5.4), the coupling coefficients were $k_1 \approx 5.6 \cdot 10^{-3}$, and in the weak coupling case (open and closed triangles), $k_2 \approx 1.8 \cdot 10^{-3}$ was determined for both filters. The filters with the same coupling strength show almost the same transmission responses with respect to the magnitude, however, the phases of the transmission responses differ by 180°, and therefore the sign (natural phase) of the coupling is different. The terms "negative" and "positive" in Fig. 5.4 are arbitrarily chosen to distinguish the two cases.

The results obtained of the test filters clearly demonstrate the advantages

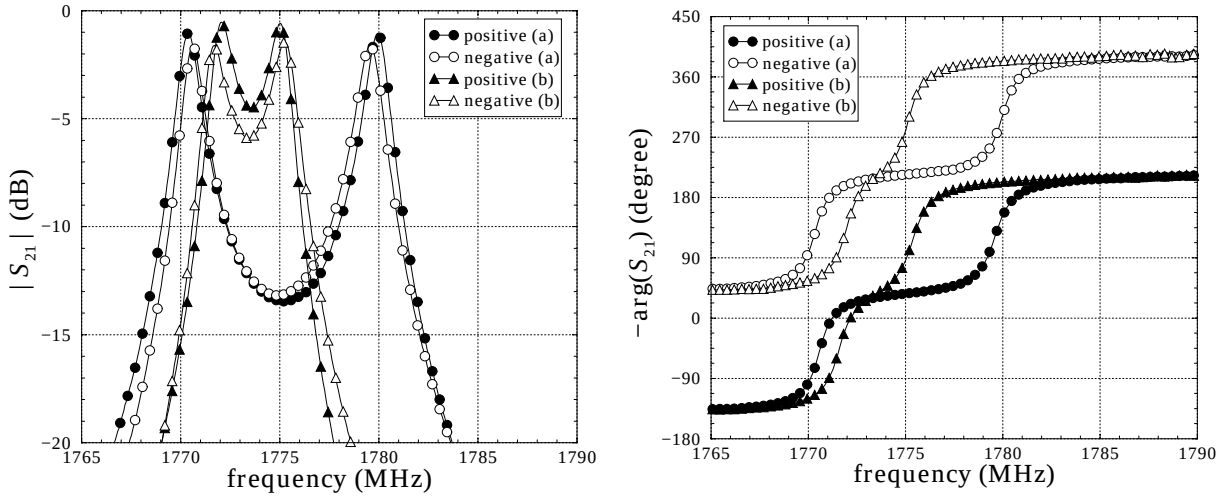

Figure 5.4: Experimental results for two–pole test filters: transmission (left) and phase (right) for different signs of coupling and coupling strength; closed symbols positive, open symbols negative coupling; (a) strong, (b) weak coupling.

of the doubly–symmetric hairpin resonator. Firstly, very weak couplings and consequently narrow–band filters can be realised although the resonators are positioned very close to each other, and secondly, the natural phase of the coupling can easily be changed.

5.3.2 Extremely narrow–band two–pole filter

The measured results of the test filters lead to the realisation of an extremely narrow–band two–pole filter. For this, two resonators with a resonant frequency of ∼1.76 GHz (each 6.5 × 6.5 mm on 0.5 mm thick $LaAlO_3$) with a spacing of only 0.25 mm as depicted in Fig. 5.5 on the left were used. The gray circles in the figure indicate the positions of sapphire tuning screws, which were placed above the filter. As for each resonator two tuning elements were used, the centre frequency as well as the coupling coefficient between the resonators could be tuned. The measured result of this filter at a temperature T = 77 K is shown on the right hand side of Fig. 5.5. The bandwidth of the filter is 0.65 MHz, which when related to the centre frequency is 0.035 %. After tuning, the input match was better than 20 dB, and the insertion loss was less than 1 dB.

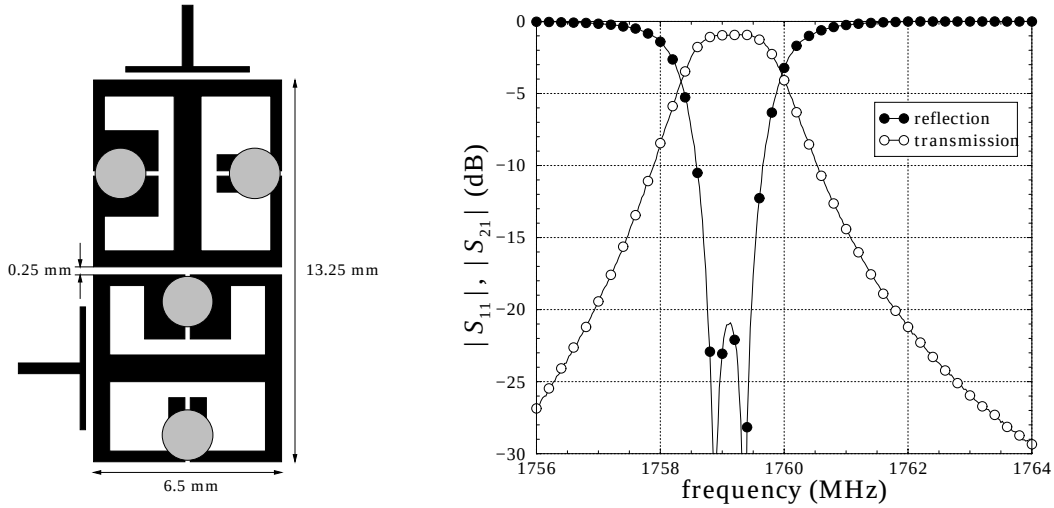

Figure 5.5: Layout (left) and measurement result (right) for an extremely narrow–band two–pole filter.

5.3.3 Quasi–elliptic narrow–band four–pole filter

A narrow–band four–pole filter with a centre frequency of ∼1.97 GHz has been designed for applications in receiver front–ends. The bandwidth of this filter is 5 MHz (≡ 0.25 %), and for steeper band edge skirts a quasi–elliptic design was

chosen. Such filters could be used for W–CDMA[‡] sub–bands for the proposed UMTS[§] for Europe or FPLMTS[¶] for Japan [27], [28].

The low–pass prototype circuit of the filter and a schematic model is shown in Fig. 5.6. As indicated in the figure, a negative cross–coupling between the first and the last (fourth) resonator has been introduced. This cross–coupling leads to a pair of symmetric transmission zeros close to the pass–band of the filter characteristic.

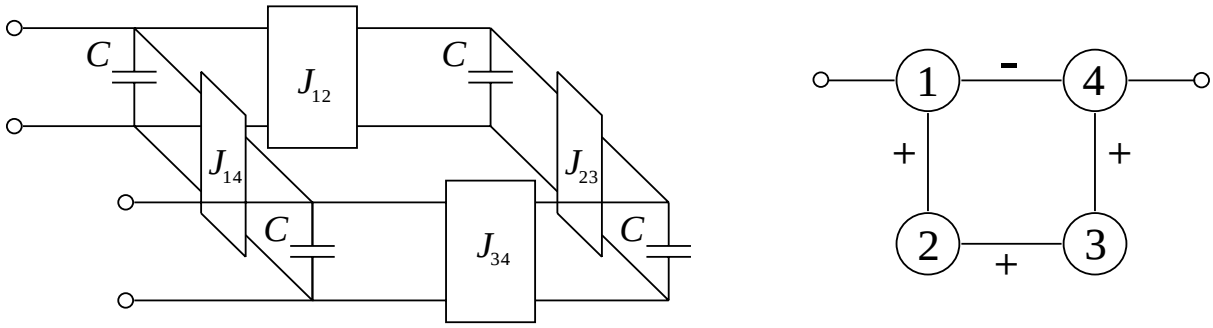

Figure 5.6: Low–pass prototype (left) and schematic filter model (right) for a four–pole quasi–elliptic filter.

Using the specified values for return loss, steepness of the band edge skirts and out–of–band rejection, the parameters of the prototype circuit (coupling coefficients k_{ij} and external quality factor Q_{ext}) were determined. However, exact analytic solutions for these parameters are generally known only for Chebyshev and Cauer filters (elliptic or truly elliptic filters) [29]. In case of quasi–elliptic filters, exact synthesis has been published for some specific filter types only [4], and for the general case numerical solutions have to be used. The parameters of the four–pole filter considered were therefore determined with the aid of circuit analysis software [30]. With today's computers, such software is capable of analysing and optimising filter parameters against given specifications within few minutes.

The low–pass prototype filter was transformed into a bandpass filter with doubly–symmetric hairpin resonators. The geometric parameters of the resonators for the required centre frequency and coupling coefficients were determined using full–wave simulation software [3]. As result, the layout shown in Fig. 5.7 on the left was obtained. The required coupling coefficients were realised with different resonator geometries as described in section 2.4.1. Therefore, the spacing between the four resonators could be kept constant as shown in the figure. The size of the compact filter structure was 12.4 $\times$ 12.4 mm and could be realised on a 20 $\times$ 20 mm $LaAlO_3$ substrate inluding the 50 Ω feedlines.

[‡]W–CDMA = Wideband – Code Division Multiple Access
[§]UMTS = Universal Mobile Telecommunication System
[¶]FPLMTS = Future Public Land Mobile Telecommunications Services

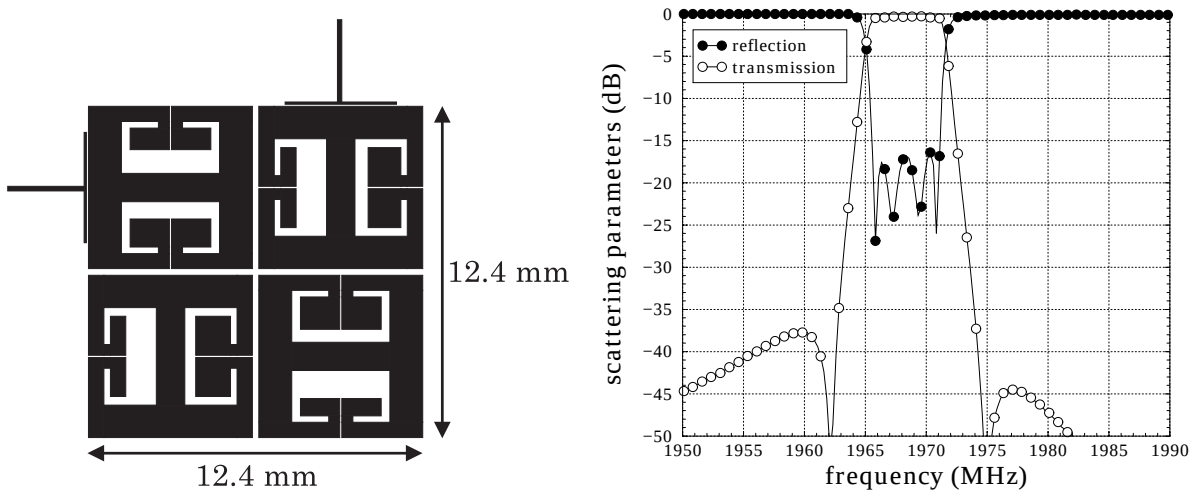

Figure 5.7: Layout (left) and measurement result (right) for a narrow–band quasi–elliptic four–pole filter (T = 60 K).

The measured results of the filter tuned at a temperature T = 60 K is shown on the right hand side of Fig. 5.7. For each resonator two sapphire tuning elements situated above the planar structure as depicted in Fig. 5.5 were used to make tuning possible. Within the pass–band, a match better than 17 dB was achieved, and due to the high quality factor ($Q_0 > 60{,}000$) the minimum insertion loss was less than 0.3 dB.

5.3.4 High order narrow–band filters

In the DCS–1800 system, the receive band for the base transceiver stations (BTS, up–link) is from 1710 to 1785 MHz, and the transmit band (down–link) from 1805 to 1880 MHz. Usually, the 75 MHz bandwidth of the system is split into sub–bands, which are assigned to different operators. If the assigned sub–bands of two closely located operators are adjacent, strong interference can occure in the case of high traffic. A lower quality of service, dropped calls, or even a complete breakdown of one sector could result. These effects can be reduced significantly if highly selective filters are used in the BTS.

Within the European Commission funded project SUCOMS (Superconducting Systems for Communications, AC115), two narrow–band high order (N = 9) filters have been developed for a demonstrator BTS front–end for the DCS–1800 system. One filter is specified for the frequency sub–band 1710 to 1720.5 MHz, the other for 1770 to 1785 MHz. Both filters are based on doubly–symmetric hairpin resonators and are to a quasi–elliptic design. In Fig. 5.8, the design of the 15 MHz filter is shown together with the filter model (the 10.5 MHz filter has an almost identical design and is therefore not shown). The necessary geometric parameters of the

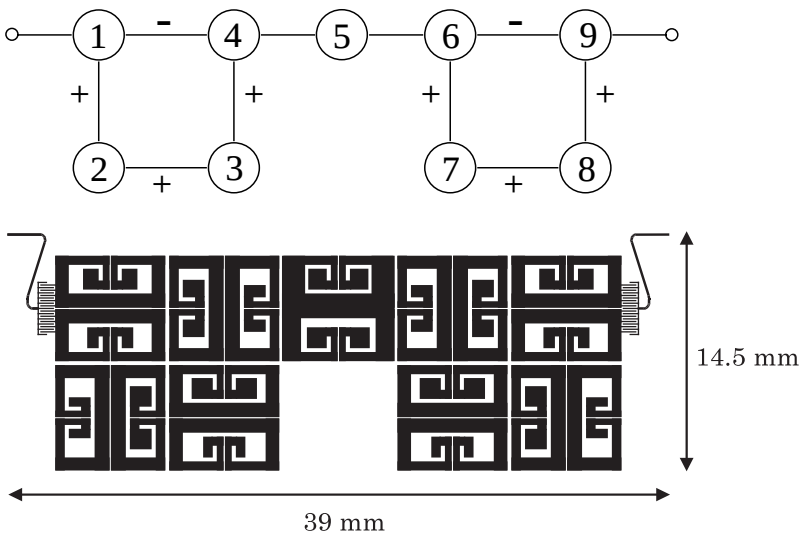

Figure 5.8: Filter model (top) and design (bottom) of the nine–pole quasi–elliptic filters.

filters have been obtained similarly to the four–pole filter described in the previous section and is not discussed further.

The experimental results obtained for both filters (T = 60 K) are shown in Fig. 5.9. The minimum insertion loss of the 15 MHz filter was less than 0.2 dB, and of the 10.5 MHz filter less than 0.3 dB. The insertion loss at the band edges increased to approx. 0.5 dB and 0.8 dB respectively. For both filters, a match of $\sim$15 dB was achieved after the tuning. Although the in–band characteristics and the steep skirts lead to a high selectivity, the out–of–band rejection of the filters differed significantly from the filter model. At frequencies lower than the pass–band, the increase of the out–of–band rejection is relatively flat compared to the frequencies higher than the pass–band. This asymmetric behaviour limits the selectivity and made the tuning more difficult.

There are two main causes which lead to the described characteristic. Firstly, as a microstrip filter is an open structure, box modes are excited and an additional transmission from the input to the output port is added to the transmission of the filter structure. It is clear that the achievable out–of–band rejection of a microstrip filter cannot exceed this parasitic transmission level. Furthermore, this effect is particularly strong for high permittivity substrates such as $LaAlO_3$ with $\varepsilon_r \approx 24$. This effect is discussed in more detail in appendix C (see page 73).

The second cause of the difference between the experimental results and the filter model in respect of the out–of–band rejection is parasitic couplings between nonadjacent resonators. With the aid of circuit analysis software, the experimental results could be verified with additional couplings between resonators three and five as well as seven and five in the filter model. Even though these parasitic couplings can be taken into account in a model, they should be avoided in practice

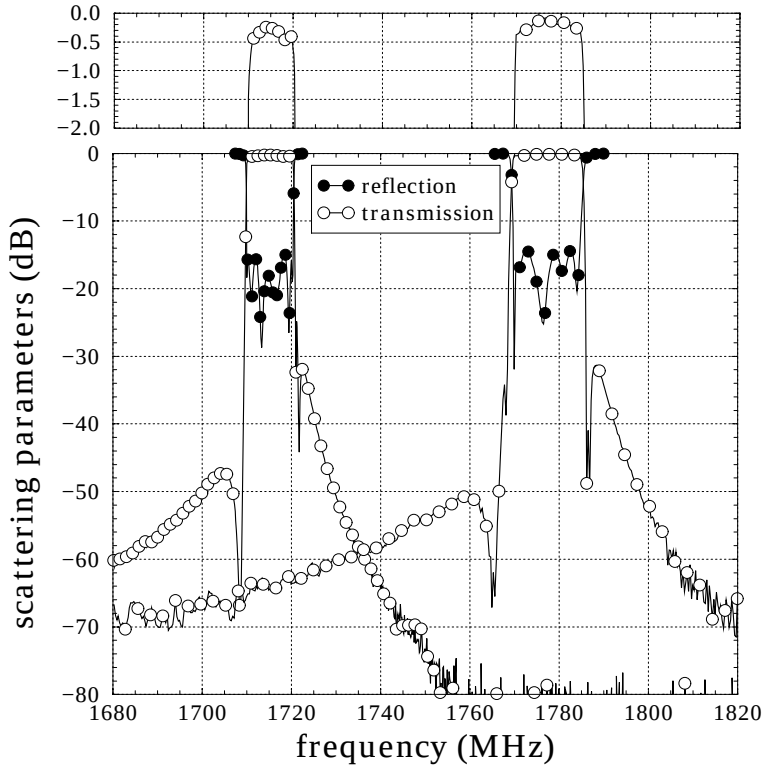

Figure 5.9: Measured results for two nine–pole filters (T = 60 K): 10.5 MHz (left curves), and 15 MHz bandwidth (right curves).

since it is difficult to control them with any accuracy.

To minimise the parasitic effects and to demonstrate miniaturised filters on $LaAlO_3$ with high out–of–band rejection, an alternative filter design with 15 MHz bandwidth based on meander–line resonators has been developed. As the same length of the substrate (39 mm) was to be used, this only allowed an eight–pole filter to be realised. The theoretic model and the design of this filter is shown in Fig. 5.10 respectively. The parasitic transmission through the housing was reduced by keeping the filter width narrow ($\sim$10 mm for the structure, $\sim$12 mm for the substrate), and as all resonators were placed in one row, parasitic coupling between nonadjacent resonators was minimised. The required cross–couplings for a quasi–elliptic filter response were realised with additional transmission lines. To achieve a different natural phase with respect to the main couplings, these transmission lines were capacitively coupled to the resonators at particular locations as shown in the figure. A limitation of this approach, which is based on relatively conventional resonators, is a reduced tuning capability compared to the filters based on doubly–symmetric resonators.

The experimental results obtained at a temperature T = 70 K of this alternative filter are shown in Fig. 5.11. By comparison to the nine–pole filter of the same

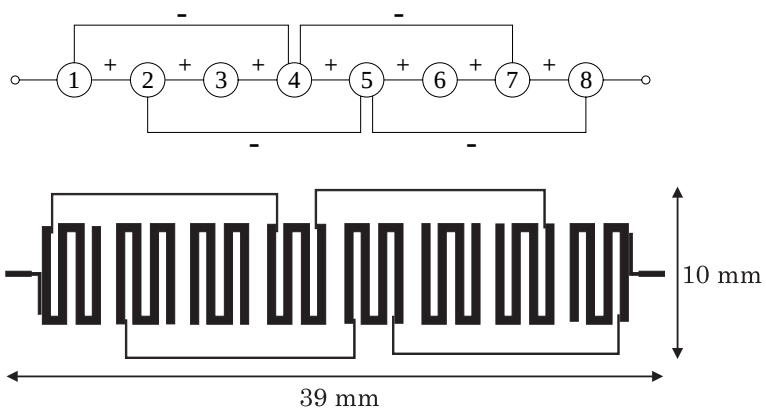

Figure 5.10: Filter model (top) and design (bottom) of the eight–pole quasi–elliptic filter. The minus signs in the filter model mark the different phase of the cross–couplings with respect to the main couplings.

bandwidth, similar values for the insertion loss and the return loss have been achieved after the tuning. However, the alternative filter has a higher and relatively symmetric out–of–band rejection.

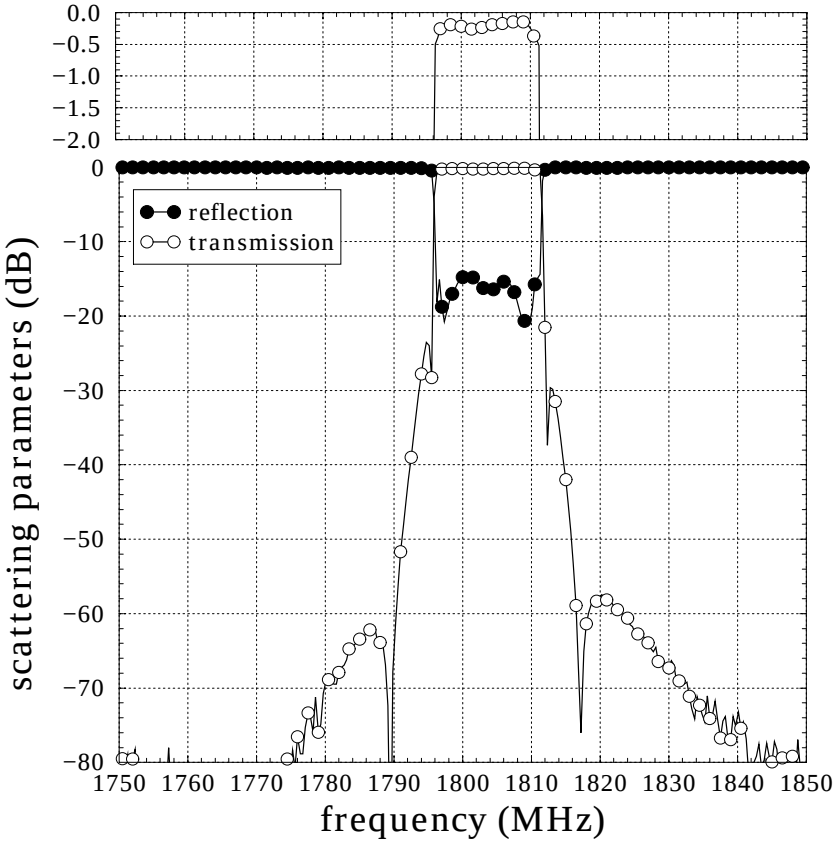

Figure 5.11: Measured result of the eight–pole filter on $LaAlO_3$ substrate at T = 70 K. The insertion loss is shown in detail at the upper plot.

5.4 Intermodulation measurements

The nonlinearity of HTS microstrip resonators is well known and has been studied experimentally and theoretically [31]. Third order intermodulation products occur at relatively low power levels, and filters in HTS microstrip technology are therefore generally restricted to receiver systems. A unique exception is a disk resonator operated in the edge–current free TM_{010} mode [32] at the expense of a larger structure.

To verify that the fabricated filters meet the requirements for receive filters, the intermodulation characteristics of the eight–pole filter (see Fig. 5.10) were measured with a two–tone measurement set–up as shown in Fig. 4.4. Three different cases have been investigated:

(a) The frequencies of the two input signals ($f_1 < f_2$) and of the intermodulation products ($2f_1 - f_2$, $2f_2 - f_1$) are all in the centre of the filter pass–band.

(b) f_1 is in the pass–band and f_2 is at the upper band edge of the pass–band ($f_2 - f_1$ = 1 MHz). The intermodulation product at $2f_2 - f_1$ is then in the stop–band of the filter.

(c) f_1 is at the upper band edge of the pass–band and f_2 is in the stop–band of the filter ($f_2 - f_1$ = 1 MHz).

In Fig. 5.12, the measured result for case (a) is shown. The power of the two sources (HP 83712B and HP 83752B) was balanced, and the power level of both intermodulation products were equal therefore. As high power amplifiers were not used for the measurement, the maximum input power was limited to 11 dBm. On the other hand, a verification measurement with a through connector instead of the filter showed no measureable intermodulation products up to the maximum input power and demonstrated that the set–up was sufficiently linear. Hence, all observed nonlinear effects were produced by the HTS filter.

The result obtained showed some deviations between the theoretical gradient of the intermodulation product and the measured gradient. Whereas in theory the gradient of the third order intermodulation product is constantly three (see Fig. 4.6), the measured gradient is less than three for low signal levels. For higher signal levels and therefore for higher intermodulation products the gradient increases slightly. This effect has been reported (see e.g. [33]) and is presumedly a typical characteristic of HTS microstrip devices.

Although a third order intercept point (IP3) cannot be derived directly from the measured data for the above mentioned reasons, the IP3 has been estimated with the assumption that from the highest measured value (at P_{in} = 11 dBm) the

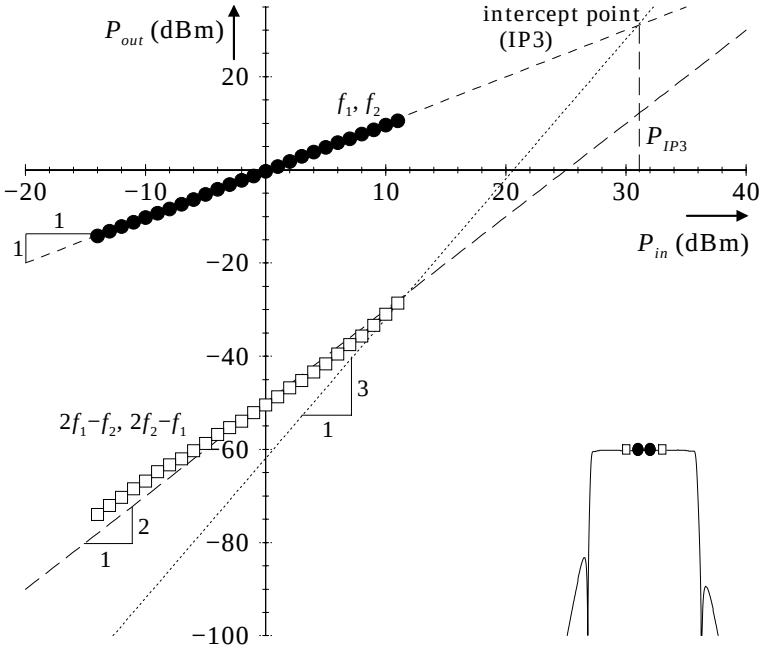

Figure 5.12: Intermodulation measurement result (T = 70 K) for the eight–pole filter depicted in Fig. 5.10: (a) the frequencies f_1 and f_2 of the two input signals as well as both intermodulation products were in the centre of the pass–band ($f_2 - f_1$ = 1 MHz).

gradient of the intermodulation product is three. With this assumption the cases (a)–(c) can be compared. For case (a), $P_{IP3} > 30$ dBm results.

For frequencies close to the band edge the intermodulation increases as more energy is stored (higher group delay). Fig. 5.13 shows the result for case (b). Noticeable here is that the power level of the intermodulation product at the frequency $2f_2 - f_1$ is higher than that at $2f_1 - f_2$ although it is in the stop–band. This is not a problem in the case of a single receive filter, but for a system with a filter bank it might be of importance. For the intermodulation product, which is in the pass–band of the filter $P_{IP3} \approx 27$ dBm can be estimated, and this value is as expected lower than in case (a).

An even lower IP3 results if one signal is close to the band edge and the other in the stop–band (case (c)). The experimental result for such a case is shown in Fig. 5.14. Here, the intermodulation product which is in the pass–band is higher, and P_{IP3} is reduced to approximately 25 dBm. The other intermodulation product is significantly lower because the stop–band attenuation is already high.

In conclusion it can be said that for the investigated eight–pole filter the estimated IP3 is 25 dBm in the worst case (c). For two signals in the centre of the pass–band the IP3 increases to over 30 dBm. The signal–to–intermodulation level is greater than 40 dB for signals up to 0 dBm.

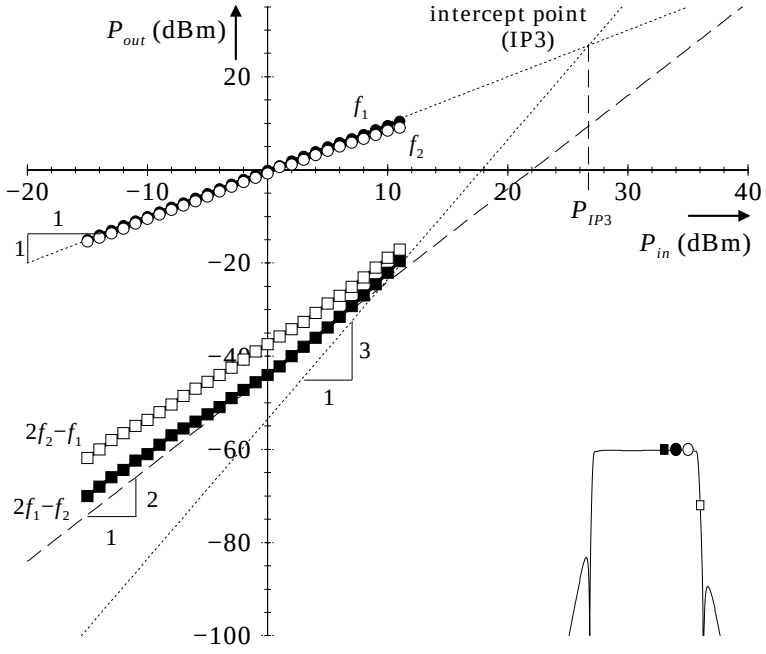

Figure 5.13: Intermodulation measurement result (T = 70 K) for the eight–pole filter: (b) the frequency f_1 of source 1 was in the pass–band, the other (f_2) at the band edge of the pass–band ($f_2 - f_1$ = 1 MHz). The intermodulation product at $2f_2 - f_1$ was in the stop–band.

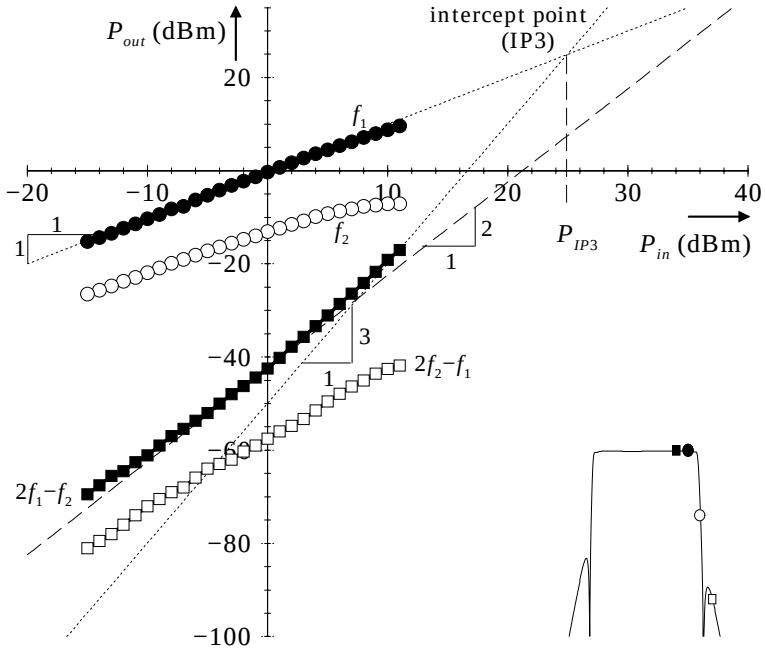

Figure 5.14: Intermodulation measurement result (T = 70 K) for the eight–pole filter: (c) the frequency f_1 of source 1 was at the band edge of the pass–band, the other (f_2) in the stop–band ($f_2 - f_1$ = 1 MHz).

Chapter 6

Filter Tuning

Although sophisticated software tools and fast computers are available to the filter designer nowadays, a measured filter response will differ from the specified response. For instance, differences can occur due to material and fabrication tolerances or to parasitic effects which have not been taken into account in the filter model. These differences can significantly degrade the filter performance especially for narrow–band filters of high order, and therefore tuning of the filter is required. On the other hand, high order filters require a large number of tuning elements and tuning is therefore a complex task. For this reason it is important to identify the actual differences between theory and measurement in order to draw the correct conclusions. This could be a revised filter design or a differently fabricated sample.

In the first part of this chapter, methods are discussed which help to determine the parameters of fabricated filters through particular measurements. In the second part, a tuning scheme is introduced which can be used to tune a high order filter in a systematic way.

6.1 Measurement of filter parameters

The theoretical performance (that is centre frequency, bandwidth, steepness of the band edge skirts etc.) of filters as discussed in the previous chapters can be expressed by three groups of parameters:

- the frequencies f_{0m} of all m–resonators,
- the coupling coefficients k_{mn} between two resonators and
- the external quality factors $Q_{ext,1}$ and $Q_{ext,2}$.

If in a realised filter all theses parameters were equal to the theoretical values, the measured filter response would be as predicted. However, as for the reasons

given above, the measured response will differ from the theoretical. As an example, a quasi–elliptic filter is discussed. Fig. 6.1 shows the theoretical transmission response together with a response, which is the result of a measurement. It can be clearly seen that the measured result is significantly different from the specified response. To identify the causes of the differences, experimental tests are carried out.

The most important parameters of a filter structure are the frequencies of the resonators, as even small deviations can lead to a poor filter response. The resonant frequencies of all resonators should be checked first. To do so, two different cases must be distinguished: the outer resonators (that is the first and the last resonators) which are coupled to the ports through the external quality factors $Q_{ext,1}$ and $Q_{ext,2}$ (or Q_{ext} if the filter is symmetric), and the inner resonators.

To check the resonant frequency of one particular inner resonator, all other resonators have to be detuned or short circuited. If now the transmission response is measured, it displays a peak at the resonant frequency of the investigated resonator.

For the two outer resonators, the method must be varied. Because of the stronger coupling to the ports the peak in the transmission response is flatter,

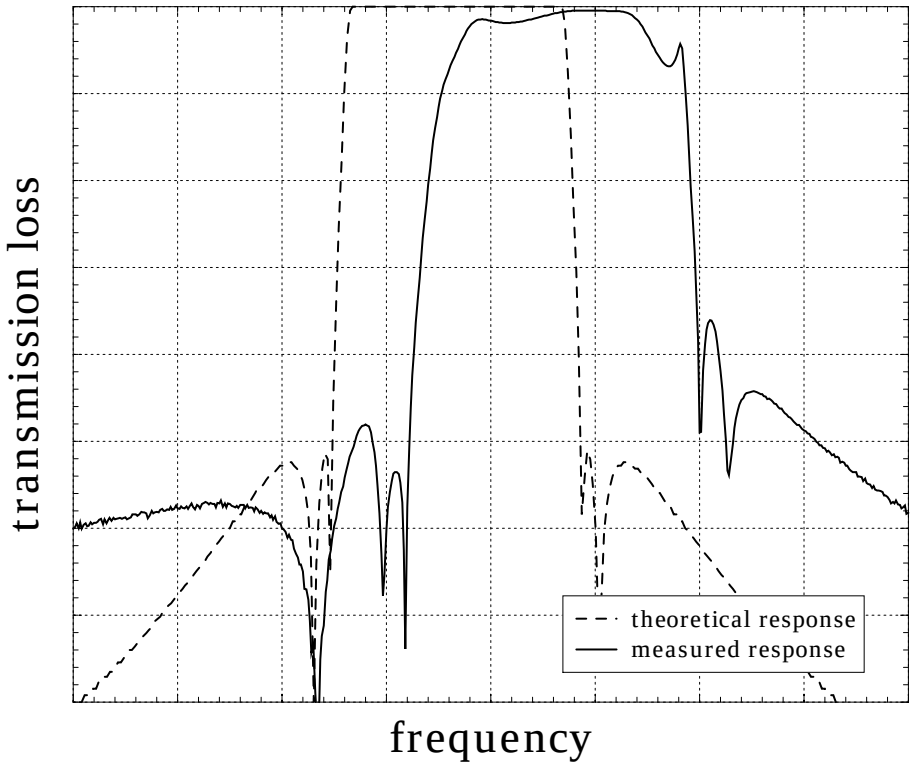

Figure 6.1: Theoretical transmission response of a quasi–elliptic filter together with the measurement result.

which makes it difficult to determine the resonant frequency without a large error. Instead of the transmission, the reflection responses S_{11} and S_{22} respectively provide the required information from the group delays $\tau_{grp,11}(\omega)$ and $\tau_{grp,22}(\omega)$ since they each display a maximum at the corresponding resonant frequency. Furthermore, as the maximum of the group delay ($\tau_{grp}(\omega = \omega_0) = \tau_{grp}$) depends on the external coupling, the external quality factor Q_{ext} can be evaluated with the approximation*

$$Q_{ext} \approx \frac{\pi}{2}\, \tau_{grp}\, f_0. \tag{6.1}$$

Examples of such test measurements are shown in Fig. 6.2. On the left hand side of the figure a measured transmission response is shown where all resonators but one inner are detuned. On the right hand side the group delay $\tau_{grp,11}(\omega)$ of the reflection is shown when all resonators but the first are detuned.

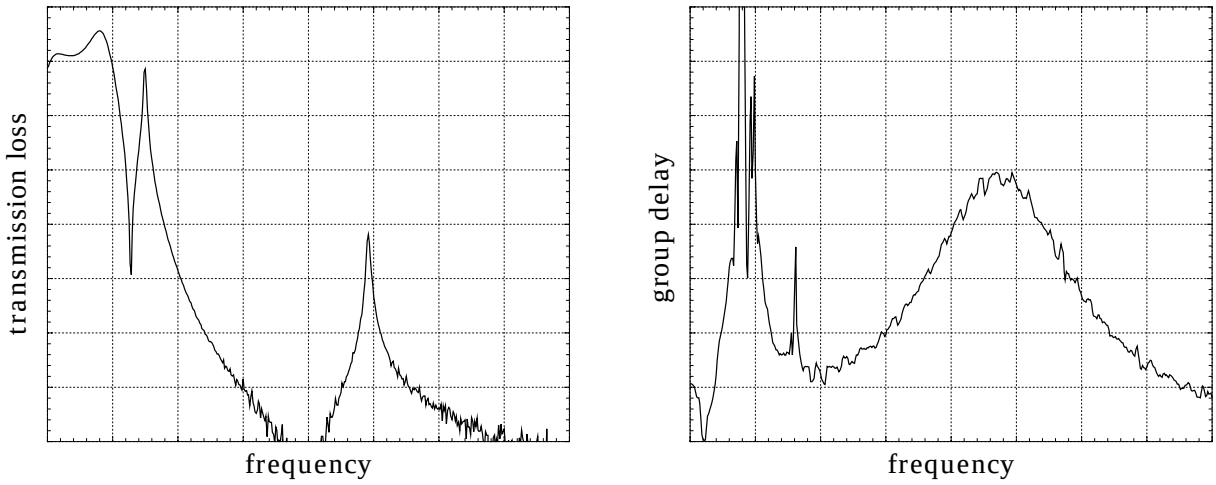

Figure 6.2: Examples for test measurements — transmission when all resonators but one inner are detuned (left), group delay $\tau_{grp,11}$ when all resonators but the first are detuned (right).

The remaining parameters to be checked are the coupling coefficients between pairs of resonators. The procedure is similar to the method described above, the only difference is that the two resonators for which the coupling coefficient is being investigated are not detuned. The transmission response displays for this case two peaks at the frequencies f_1 and f_2, and the coupling coefficient k_{mn} between the mth– and the nth–resonator is then approximately given by

$$k_{mn} \approx \frac{f_2 - f_1}{\sqrt{f_1 f_2}}. \tag{6.2}$$

*derivation given in appendix D

However, this method is only valid if the two resonant frequencies of the resonators are the same. If this is not the case, then the experimentally determined coupling coefficient will be incorrect, which means that the coupling coefficient appears to be larger than it actually is. This can be avoided if the frequency difference $\Delta f = f_2 - f_1$ is minimised by fine tuning of the two resonators. Furthermore, the coupling coefficient between the first and second resonator (last and last but one respectively) must be checked differently because of the stronger coupling to the ports. Here, the group delay of the reflection can be considered again. The experimental procedure of detuned resonators can be transfered to the equivalent circuit of the filter and the theoretical group delay of the reflection can than be compared with the measurement result. Fig. 6.3 shows two examples from which the coupling coefficients can be determined.

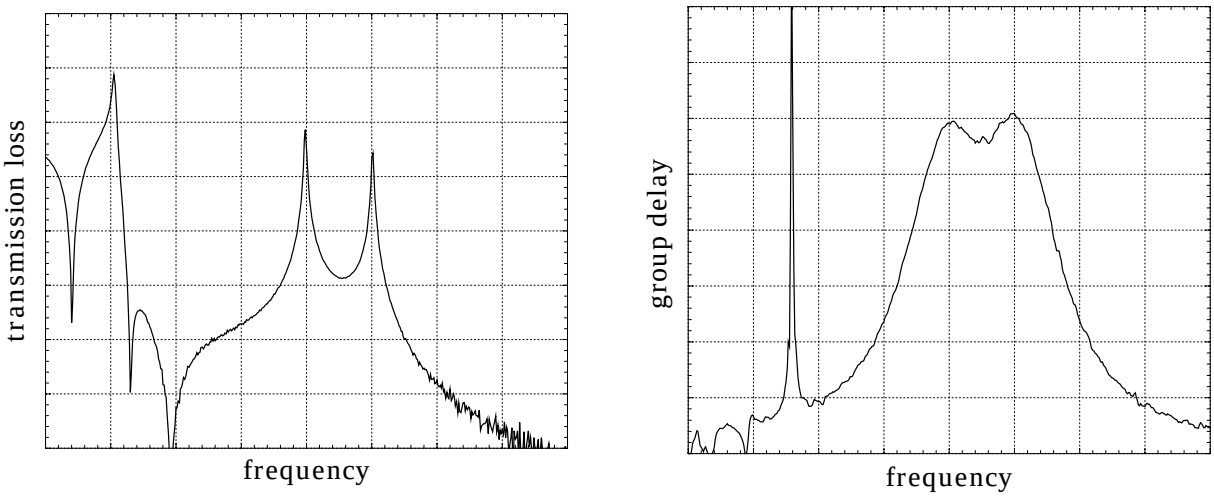

Figure 6.3: Examples for the determination of coupling coefficients — transmission response for two inner resonators (left), group delay $\tau_{grp,11}$ of the first and second resonator (right).

6.2 Iterative tuning scheme

Even if a measured frequency response of a filter does not differ much from the theory, the fine tuning can be difficult, e.g. if the centre frequency is not correct. In this case, all resonator frequencies have to be changed step by step. It can be helpful to perform the tuning by considering the group delay of the reflection coefficients S_{11} and S_{22} as described in the last section.

At first, the centre frequency of all resonators must be detuned. Then, the first and the last resonator can be tuned to the correct centre frequency of the filter by measuring the group delays $\tau_{grp,11}$ and $\tau_{grp,22}$ simultaneously. Comparing

the measured data with the theory (equivalent circuit), the tuning of the other resonators can follow in pairs, but it has to be verified at each step that both group delays correspond and that the centre frequency is maintained constant. As an example, the measured group delay $\tau_{grp,11}$ for several tuning steps of a nine–pole filter is shown in Fig. 6.4.

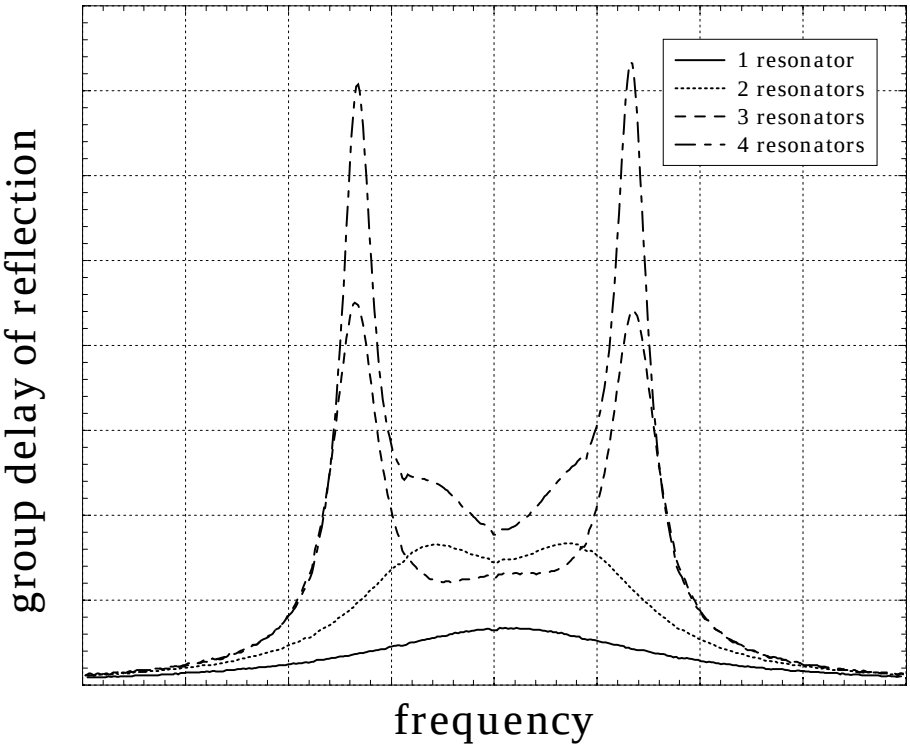

Figure 6.4: Measured group delays $\tau_{grp,11}$ for four tuning steps of a nine–pole filter.

Appendix A

Normalised expansion functions $\mathbf{f}_{mn}^{\mathrm{TE}}(x,y)$ and $\mathbf{f}_{mn}^{\mathrm{TM}}(x,y)$

In general, the normalised expansion functions $\mathbf{f}_{mn}^{\mathrm{TE}}(x,y)$ and $\mathbf{f}_{mn}^{\mathrm{TM}}(x,y)$ have to satisfy

$$\int_0^b \int_0^a \mathbf{f}_{mn}^{\mathrm{TE,TM}}(x,y) \cdot \mathbf{f}_{pq}^{\mathrm{TE,TM}}(x,y)\, dxdy = 1, \qquad \text{for } m = p \text{ and } n = q \tag{A.1}$$

$$\int_0^b \int_0^a \mathbf{f}_{mn}^{\mathrm{TE,TM}}(x,y) \cdot \mathbf{f}_{pq}^{\mathrm{TE,TM}}(x,y)\, dxdy = 0, \qquad \text{for } m \neq p \text{ or } n \neq q \tag{A.2}$$

$$\int_0^b \int_0^a \mathbf{f}_{mn}^{\mathrm{TE}}(x,y) \cdot \mathbf{f}_{pq}^{\mathrm{TM}}(x,y)\, dxdy = 0 \tag{A.3}$$

for the rectangular waveguide geometry shown in Fig. 3.8. Since TE_{mn}– and TM_{mn}–modes with respect to z are considered, the transverse spatial distribution of these waveguide modes [34] may be taken to obtain the expansion functions, excluding the case $m = n = 0$ as well as TM_{m0} and TM_{0n}:

$$\mathbf{f}_{mn}^{\mathrm{TE}}(x,y) = C \begin{pmatrix} \cos\left(\frac{m\pi x}{a}\right) \sin\left(\frac{n\pi y}{b}\right) \\ -\sin\left(\frac{m\pi x}{a}\right) \cos\left(\frac{n\pi y}{b}\right) \\ 0 \end{pmatrix} \tag{A.4}$$

$$\mathbf{f}_{mn}^{\mathrm{TM}}(x,y) = C \begin{pmatrix} \cos\left(\frac{m\pi x}{a}\right) \sin\left(\frac{n\pi y}{b}\right) \\ \sin\left(\frac{m\pi x}{a}\right) \cos\left(\frac{n\pi y}{b}\right) \\ 0 \end{pmatrix}. \tag{A.5}$$

Because of the orthogonality of the eigenmodes the criteria (A.2) and (A.3) are already satisfied, and in order to satisfy (A.1), C has to be determined by

$$C^2 \int_0^b \int_0^a \left[\cos^2\left(\frac{m\pi x}{a}\right)\sin^2\left(\frac{n\pi y}{b}\right) + \sin^2\left(\frac{m\pi x}{a}\right)\cos^2\left(\frac{n\pi y}{b}\right)\right] dxdy = 1. \tag{A.6}$$

Solving for C, we obtain from this equation

$$C = \sqrt{\frac{2}{ab}} \tag{A.7}$$

and the normalised expansion functions become finally

$$\mathbf{f}_{mn}^{\mathrm{TE}}(x,y) = \sqrt{\frac{2}{ab}} \begin{pmatrix} \cos\left(\frac{m\pi x}{a}\right)\sin\left(\frac{n\pi y}{b}\right) \\ -\sin\left(\frac{m\pi x}{a}\right)\cos\left(\frac{n\pi y}{b}\right) \\ 0 \end{pmatrix} \tag{A.8}$$

$$\mathbf{f}_{mn}^{\mathrm{TM}}(x,y) = \sqrt{\frac{2}{ab}} \begin{pmatrix} \cos\left(\frac{m\pi x}{a}\right)\sin\left(\frac{n\pi y}{b}\right) \\ \sin\left(\frac{m\pi x}{a}\right)\cos\left(\frac{n\pi y}{b}\right) \\ 0 \end{pmatrix}. \tag{A.9}$$

Appendix B

Derivation of the effective surface resistances $R^{\mathbf{TE}}_{eff,mn}(x,y)$ and $R^{\mathbf{TM}}_{eff,mn}(x,y)$

Considering the rectangular waveguide geometry depicted in Fig 3.8, the transverse electric field for TE_{mn}–modes may be expressed by

$$\mathbf{E}_1^{\mathrm{TE}}(x,y,z) = \tilde{\mathbf{E}}_1^{\mathrm{TE}}(x,y)\left(\mathrm{e}^{-jk_{z1}z} + \Gamma_1^{\mathrm{TE}}\mathrm{e}^{jk_{z1}z}\right) \tag{B.1}$$

for $0 < z < c$ (domain 1). Similarly, the magnetic field for TM_{mn}–modes is given by

$$\mathbf{H}_1^{\mathrm{TM}}(x,y,z) = \tilde{\mathbf{H}}_1^{\mathrm{TM}}(x,y)\left(\mathrm{e}^{-jk_{z1}z} + \Gamma_1^{\mathrm{TM}}\mathrm{e}^{jk_{z1}z}\right). \tag{B.2}$$

The reflected waves due to the metallic wall at $z = c$ have been accounted for by the reflection coefficients Γ_1^{TE} and Γ_1^{TM}. From Maxwell's first equation

$$\nabla \times \mathbf{E} = j\omega\mu\mathbf{H} \tag{B.3}$$

the magnetic field for TE_{mn}–modes can be calculated:

$$\mathbf{H}_1^{\mathrm{TE}}(x,y,z) = \begin{pmatrix} H_{x1}^{\mathrm{TE}} \\ H_{y1}^{\mathrm{TE}} \\ H_{z1}^{\mathrm{TE}} \end{pmatrix} = \frac{j}{\omega\mu_1}\begin{pmatrix} \partial E_{y1}^{\mathrm{TE}}/\partial z \\ -\partial E_{x1}^{\mathrm{TE}}/\partial z \\ \partial E_{x1}^{\mathrm{TE}}/\partial y - \partial E_{y1}^{\mathrm{TE}}/\partial x \end{pmatrix}. \tag{B.4}$$

The transverse part of (B.4) is

$$\mathbf{H}_{t1}^{\mathrm{TE}}(x,y,z) = \begin{pmatrix} H_{x1}^{\mathrm{TE}} \\ H_{y1}^{\mathrm{TE}} \\ 0 \end{pmatrix} = \frac{j}{\omega\mu_1}\begin{pmatrix} \partial E_{y1}^{\mathrm{TE}}/\partial z \\ -\partial E_{x1}^{\mathrm{TE}}/\partial z \\ 0 \end{pmatrix}, \tag{B.5}$$

and with (B.1) we obtain for $\mathbf{H}_{t1}^{\mathrm{TE}}$:

$$\mathbf{H}_{t1}^{\mathrm{TE}}(x,y,z) = \frac{k_{z1}}{\omega\mu_1}\begin{pmatrix} \tilde{E}_{y1}^{\mathrm{TE}}(x,y) \\ -\tilde{E}_{x1}^{\mathrm{TE}}(x,y) \\ 0 \end{pmatrix} \cdot \left(\mathrm{e}^{-jk_{z1}z} - \Gamma_1^{\mathrm{TE}}\mathrm{e}^{jk_{z1}z}\right). \tag{B.6}$$

The latter expression may also be written as

$$\mathbf{H}_{t1}^{\mathrm{TE}}(x,y,z) = \frac{-k_{z1}}{\omega\mu_1}(\mathbf{e}_z \times \tilde{\mathbf{E}}_1^{\mathrm{TE}}(x,y)) \cdot \left(\mathrm{e}^{-jk_{z1}z} - \Gamma_1^{\mathrm{TE}}\mathrm{e}^{jk_{z1}z}\right). \tag{B.7}$$

With the transverse electric field and the transverse part of the magnetic field for TE$_{mn}$–modes, a transverse impedance $Z_{t1}^{\mathrm{TE}}(z) = E_1^{\mathrm{TE}}/H_{t1}^{\mathrm{TE}}$ may be defined:

$$Z_{t1}^{\mathrm{TE}}(z) = Z_{f1}^{\mathrm{TE}}\,\frac{1+\Gamma_1^{\mathrm{TE}}\,\mathrm{e}^{j2k_{z1}z}}{1-\Gamma_1^{\mathrm{TE}}\,\mathrm{e}^{j2k_{z1}z}} \tag{B.8}$$

with $Z_{f1}^{\mathrm{TE}} = \omega\mu_1/k_{z1}$. For TM$_{mn}$–modes, the transverse impedance $Z_{t1}^{\mathrm{TM}}(z)$ can be derived in the same manner:

$$Z_{t1}^{\mathrm{TM}}(z) = Z_{f1}^{\mathrm{TM}}\,\frac{1-\Gamma_1^{\mathrm{TM}}\,\mathrm{e}^{j2k_{z1}z}}{1+\Gamma_1^{\mathrm{TM}}\,\mathrm{e}^{j2k_{z1}z}} \tag{B.9}$$

with $Z_{f1}^{\mathrm{TM}} = k_{z1}/(\omega\varepsilon_1)$. The reflection coefficients Γ_1^{TE} and Γ_1^{TM} are determined by the boundary condition $Z_{t1}^{\mathrm{TE}}(z=c) = Z_{t1}^{\mathrm{TM}}(z=c) = Z_1$. Applying this, the transverse impedances for $z = 0$ become

$$Z_{t1}^{\mathrm{TE}} \;=\; Z_{f1}^{\mathrm{TE}}\,\frac{(Z_1+Z_{f1}^{\mathrm{TE}}) + (Z_1-Z_{f1}^{\mathrm{TE}})\,\mathrm{e}^{-j2k_{z1}c}}{(Z_1+Z_{f1}^{\mathrm{TE}}) - (Z_1-Z_{f1}^{\mathrm{TE}})\,\mathrm{e}^{-j2k_{z1}c}} \tag{B.10}$$

$$Z_{t1}^{\mathrm{TM}} \;=\; Z_{f1}^{\mathrm{TM}}\,\frac{(Z_1+Z_{f1}^{\mathrm{TM}}) + (Z_1-Z_{f1}^{\mathrm{TM}})\,\mathrm{e}^{-j2k_{z1}c}}{(Z_1+Z_{f1}^{\mathrm{TM}}) - (Z_1-Z_{f1}^{\mathrm{TM}})\,\mathrm{e}^{-j2k_{z1}c}}. \tag{B.11}$$

Since we have found similar expressions for Z_{t1}^{TE} and Z_{t1}^{TM}, we omit the superscripts TE and TM for the present. In order to simplify these formulae, we use the first two terms of their Taylor series

$$Z_{t1} \approx Z_{t1}\Big|_{Z_1=0} \;+\; \frac{dZ_{t1}}{dZ_1}\Big|_{Z_1=0} \cdot Z_1, \tag{B.12}$$

assuming sufficient low Z_1 values, e.g. for good conductors. After some calculations we obtain

$$Z_{t1} \approx \frac{Z_1}{\cos^2(k_{z1}c)} \;+\; jZ_{f1}\tan(k_{z1}c). \tag{B.13}$$

The imaginary part of (B.13) is a measure for the stored energy, and since most of the energy is stored in the volume $0 < z < c$, the imaginary part of Z_1 may be neglected. Thus, we become finally:

$$Z_{t1} \approx \frac{R_1}{\cos^2(k_{z1}c)} \;+\; jZ_{f1}\tan(k_{z1}c). \tag{B.14}$$

To obtain the transformed impedance Z_{t2} for $-h < z < 0$, (B.14) can be adopted straightaway. However, only structures with a superconducting ground plane will be considered, and we can safely assume $Z_2 = 0$. We therefore become

$$Z_{t2} \approx jZ_{f2} \tan(k_{z2}h). \tag{B.15}$$

For each eigenmode, both transformed impedances take effect simultaneously, that is Z_{t1} and Z_{t2} are in parallel. Thus, we have to determine R_{eff} with

$$Z_{\mathit{eff}} = R_{\mathit{eff}} + jX_{\mathit{eff}} = \frac{Z_{t1} \cdot Z_{t2}}{Z_{t1} + Z_{t2}} \tag{B.16}$$

With $Z_{t1} = R_{t1} + jX_{t1}$ and $Z_{t2} = jX_{t2}$ we obtain

$$Z_{\mathit{eff}} = \frac{X_{t2}^2 R_{t1} + j\ X_{t2}(R_{t1}^2 + X_{t1}^2 + X_{t1}X_{t2})}{R_{t1}^2 + (X_{t1} + X_{t2})^2}. \tag{B.17}$$

Knowing that $(X_{t1} + X_{t2})^2 \gg R_{t1}^2$, the effective surface resistance R_{eff} becomes

$$R_{\mathit{eff}} \approx \left(\frac{X_{t2}}{X_{t1} + X_{t2}}\right)^2 R_{t1}. \tag{B.18}$$

Inserting (B.14) and (B.15), we find

$$R_{\mathit{eff}} \approx \left(\frac{Z_{f2} \tan(k_{z2}h)}{Z_{f2} \tan(k_{z2}h) + Z_{f1} \tan(k_{z1}c)}\right)^2 \frac{R_1}{\cos^2(k_{z1}c)}. \tag{B.19}$$

We remember that we have

$$Z_{f1} = \frac{\omega\mu_1}{k_{z1}}, \quad Z_{f2} = \frac{\omega\mu_2}{k_{z2}} \tag{B.20}$$

for TE_{mn}–modes and

$$Z_{f1} = \frac{k_{z1}}{\omega\varepsilon_1}, \quad Z_{f2} = \frac{k_{z2}}{\omega\varepsilon_2} \tag{B.21}$$

for TM_{mn}–modes. With $\mu_1 = \mu_2 = \mu_0$, $\varepsilon_1 = \varepsilon_0$, $\varepsilon_2 = \varepsilon_0\varepsilon_{r2}$ and $k_{z1} \to k_{z1,mn}$, $k_{z2} \to k_{z2,mn}$ we obtain finally

$$R_{\mathit{eff},mn}^{\mathrm{TE}} \approx \left(\frac{k_{z1,mn} \tan(k_{z2,mn}h)}{k_{z1,mn} \tan(k_{z2,mn}h) + k_{z2,mn} \tan(k_{z1,mn}c)}\right)^2 \frac{R_1}{\cos^2(k_{z1,mn}c)} \tag{B.22}$$

$$R_{\mathit{eff},mn}^{\mathrm{TM}} \approx \left(\frac{k_{z2,mn} \tan(k_{z2,mn}h)}{k_{z2,mn} \tan(k_{z2,mn}h) + \varepsilon_{r2}k_{z1,mn} \tan(k_{z1,mn}c)}\right)^2 \frac{R_1}{\cos^2(k_{z1,mn}c)}. \tag{B.23}$$

Appendix C

Parasitic Transmission through the Housing

Besides the quasi–TEM mode of a microstrip transmission line other modes are present. If a microstrip device is mounted into a metallic box for reason of shielding, box modes (wave guide modes) exist, and since microstrip devices are open structures, these unwanted modes may be excited. Even if such box modes are not resonant or the resonant frequencies are far away from the considered frequency band of the microstrip device, parasitic transmission through the box modes is present. This is especially disadvantageous for microstrip bandpass filters as the out–of–band rejection cannot exceed this parasitic transmission. Furthermore, if the unwanted modes are strongly excited, the whole characteristic and therefore the performance can be degraded.

C.1 Full–wave simulation software analysis

Experimental results have shown that the transmission through box modes depends not only on the geometry of the surrounding box but also on the permittivity of the substrate material. This effect can easily be investigated with full–wave analysis software. With this approach, the magnitude of the parasitic transmission can be analysed for a variety of box sizes (width, height and length) as well as substrate permittivity and thickness. For such an analysis, a structure as depicted in Fig. C.1 was used. The structure investigated consists of an ideally conductive box of width a, height b and length l. Mounted in the box is a substrate of thickness h, width a and permittivity ε_r. The distance between the short microstrip lines, which are to excite the box modes, and the top of the housing is given by $b-h$.

Firstly, the dependence of the parasitic transmission on the permittivity was investigated. For this, the dimensions of the box and of the substrate were chosen

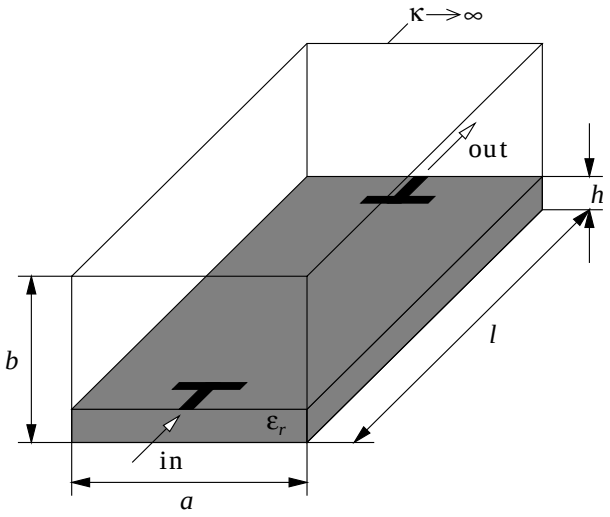

Figure C.1: Microstrip test structure to investigate the parasitic transmission through a surrounding box with full–wave analysis software.

to be a = 15 mm, b = 5.5 mm, l = 20 mm, and h = 0.5 mm. The permittivity of the substrate was varied between $1 \leq \varepsilon_r \leq 30$. As in this work microstrip devices for about 2 GHz are presented, the considered frequency range in the simulations was 1 GHz $\leq f \leq$ 3 GHz. The results of the simulations are shown in Fig. C.2. On the left hand side, the magnitude of the transmission (in dB) for different values of the permittivity is shown. The graph on the right hand side of Fig. C.2 shows the transmission dependence on the permittivity for f = 2 GHz

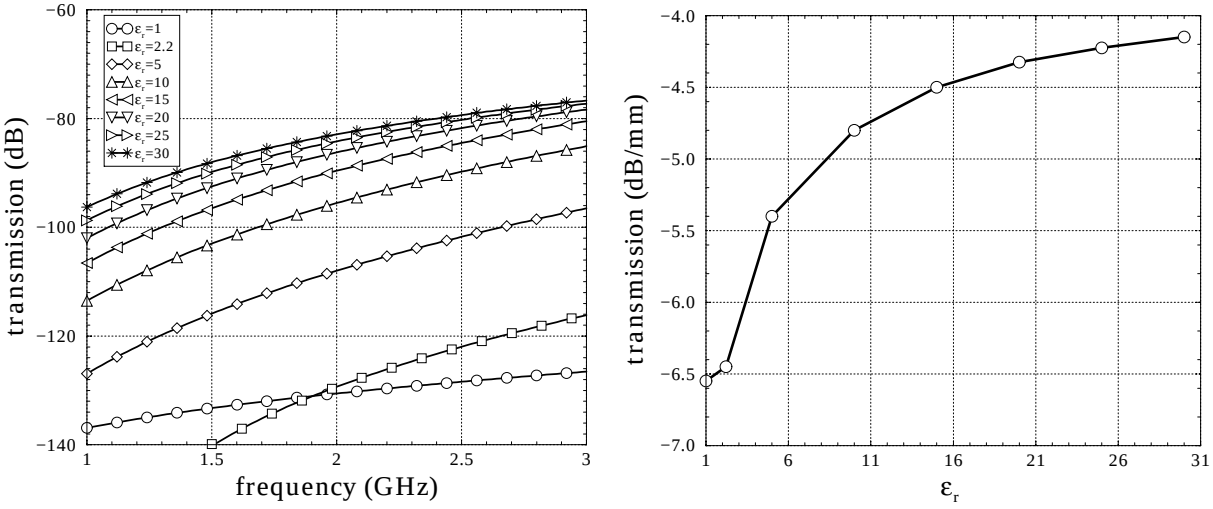

Figure C.2: Simulation results of the parasitic transmission through a housing with the dimensions a = 15 mm, b = 5.5 mm, l = 20 mm, and a substrate thickness of h = 0.5 mm: frequency dependence (left) and permittivity dependence (right, f_0 = 2 GHz, normalised to the length l).

normalised to the length l of the housing. The simulation results obtained clearly show that the parasitic transmission through box modes significantly increases as the permittivity of a substrate is increased. Although the actual values of the observed parasitic transmissions seem to be relatively low (∼-75 dB or less), it has to be considered that the feeding microstrip lines have been kept short in order to obtain a common result. In a filter structure however, at least the first resonator is excited even if its resonant frequency is far away. In this case, a parasitic mode may be readily excited, and the parasitic transmission will therefore be much higher.

Further simulations were carried out whereby the width a of the housing was changed in the range 5 mm $\leq a \leq$ 30 mm. Additionally, two different substrate permittivities (ε_r = 10 and ε_r = 24) were investigated. The results which are depicted in Fig. C.3 show that the parasitic transmission changes with the width of the housing. The narrower the housing, the smaller the parasitic transmission. Consequently, if the parasitic transmission is too high, e.g. in case of high permittivity substrates, it can be reduced by keeping the whole structure as narrow as possible.

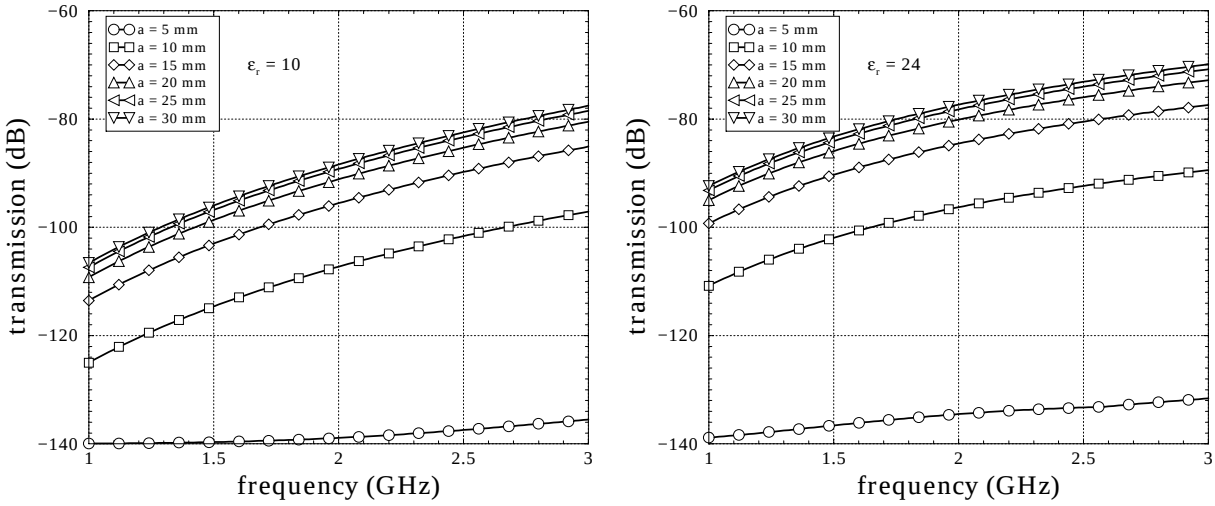

Figure C.3: Simulation results of parasitic transmission through a housing with the measures 5 mm $\leq a \leq$ 30 mm, b = 5.5 mm, l = 20 mm, and a substrate thickness of h = 0.5 mm for ε_r = 10 (left) and ε_r = 24 (right)

C.2 Theoretical analysis

The parasitic box modes in a microstrip structure can theoretically be analysed when the cross–section of the structure in Fig. C.1 is considered. This cross–section represents a rectangular waveguide with a dielectric inset of thickness h and

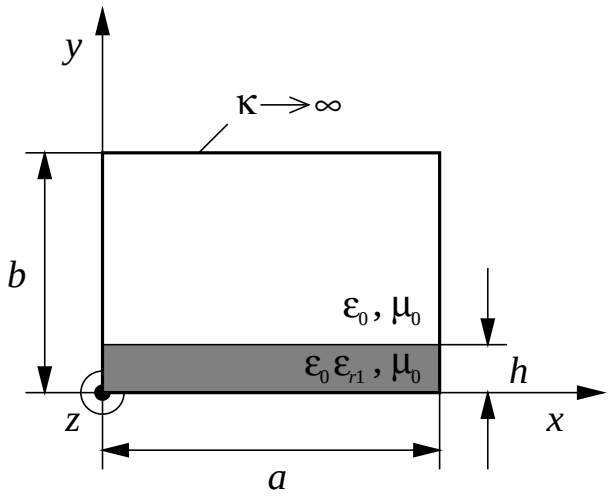

Figure C.4: Cross–section of a rectangular waveguide with an embedded substrate of thickness h and permittivity ε_{r1}.

permittivity $\varepsilon_{r1} > 1$ which is embedded as shown in Fig. C.4. The fundamental mode (quasi–TE$_{10}$, $a > b$) is mainly responsible for the parasitic transmission.

Using $\gamma = \alpha + j\beta$ and $k_0 = 2\pi/\lambda_0$, the electromagnetic field analysis for the forward wave propagation of the quasi–TE$_{10}$ mode results

$$
\begin{aligned}
E_{x1} &= -\frac{\sqrt{k_y^2 + k_0^2(\varepsilon_{r1}-1)}}{k_0^2 - k_y^2}\,\frac{\pi}{a}\,E_1\,\cos\left(\frac{\pi}{a}x\right)\,\sin\left(\sqrt{k_y^2 + k_0^2(\varepsilon_{r1}-1)}\,y\right)\,\mathrm{e}^{-\gamma z}\\
E_{y1} &= E_1\,\sin\left(\frac{\pi}{a}x\right)\,\cos\left(\sqrt{k_y^2 + k_0^2(\varepsilon_{r1}-1)}\,y\right)\,\mathrm{e}^{-\gamma z}\\
E_{z1} &= \frac{\gamma\sqrt{k_y^2 + k_0^2(\varepsilon_{r1}-1)}}{k_0^2 - k_y^2}E_1\,\sin\left(\frac{\pi}{a}x\right)\,\sin\left(\sqrt{k_y^2 + k_0^2(\varepsilon_{r1}-1)}\,y\right)\,\mathrm{e}^{-\gamma z}\\
H_{x1} &= \frac{j\omega\gamma\varepsilon_0\varepsilon_{r1}}{k_0^2 - k_y^2}E_1\,\sin\left(\frac{\pi}{a}x\right)\,\cos\left(\sqrt{k_y^2 + k_0^2(\varepsilon_{r1}-1)}\,y\right)\,\mathrm{e}^{-\gamma z}\\
H_{y1} &= 0\\
H_{z1} &= \frac{j\omega\varepsilon_0\varepsilon_{r1}}{k_0^2 - k_y^2}\,\frac{\pi}{a}\,E_1\,\sin\left(\frac{\pi}{a}x\right)\,\cos\left(\sqrt{k_y^2 + k_0^2(\varepsilon_{r1}-1)}\,y\right)\,\mathrm{e}^{-\gamma z}
\end{aligned}
\qquad \text{(C.1)}
$$

for the field components of the fields $\mathbf{E}_1$ and $\mathbf{H}_1$ within the substrate ($0 \le y < h$, $\varepsilon = \varepsilon_0\varepsilon_{r1}$) and

$$
E_{x2} = \frac{k_y}{k_0^2 - k_y^2}\,\frac{\pi}{a}\,E_2\,\cos\left(\frac{\pi}{a}x\right)\,\left[\tan\left(k_y b\right)\cos\left(k_y y\right) - \sin\left(k_y y\right)\right]\,\mathrm{e}^{-\gamma z}
$$

$$
\begin{aligned}
E_{y2} &= E_2 \ \sin\left(\frac{\pi}{a}x\right) \ \left[\tan\left(k_y b\right)\sin\left(k_y y\right)+\cos\left(k_y y\right)\right] \ \mathrm{e}^{-\gamma z} \\
E_{z2} &= -\frac{\gamma k_y}{k_0^2-k_y^2} \ E_2 \ \sin\left(\frac{\pi}{a}x\right) \ \left[\tan\left(k_y b\right)\cos\left(k_y y\right)-\sin\left(k_y y\right)\right] \ \mathrm{e}^{-\gamma z} \\
H_{x2} &= \frac{j\omega\gamma\varepsilon_0}{k_0^2-k_y^2} \ E_2 \ \sin\left(\frac{\pi}{a}x\right) \ \left[\tan\left(k_y b\right)\sin\left(k_y y\right)+\cos\left(k_y y\right)\right] \ \mathrm{e}^{-\gamma z} \\
H_{y2} &= 0 \\
H_{z2} &= \frac{j\omega\varepsilon_0}{k_0^2-k_y^2}\,\frac{\pi}{a} \ E_2 \ \cos\left(\frac{\pi}{a}x\right) \ \left[\tan\left(k_y b\right)\sin\left(k_y y\right)+\cos\left(k_y y\right)\right] \ \mathrm{e}^{-\gamma z}
\end{aligned}
\tag{C.2}
$$

for the field components of the fields $\mathbf{E}_2$ and $\mathbf{H}_2$ above the substrate ($h < y \leq b$, $\varepsilon = \varepsilon_0$). The ratio of the constants E_1 and E_2 is determined by

$$
\frac{E_1}{E_2} = \frac{\tan\left(k_y b\right)\sin\left(k_y h\right)+\cos\left(k_y h\right)}{\varepsilon_{r1} \ \cos\left(\sqrt{k_y^2+k_0^2(\varepsilon_{r1}-1)} \ h\right)}.
$$

Besides frequency, the propagation constant γ depends only on the permittivity of the substrate and on the geometric parameters. γ is given by the equation

$$
\begin{aligned}
&\sqrt{k_0^2-\left(\frac{\pi}{a}\right)^2+\gamma^2} \quad \tan\left(\sqrt{k_0^2-\left(\frac{\pi}{a}\right)^2+\gamma^2}\,(b-h)\right)+ \\
&\quad + \ \frac{1}{\varepsilon_{r1}}\sqrt{k_0^2\varepsilon_{r1}-\left(\frac{\pi}{a}\right)^2+\gamma^2} \quad \tan\left(\sqrt{k_0^2\varepsilon_{r1}-\left(\frac{\pi}{a}\right)^2+\gamma^2} \ h\right) = 0
\end{aligned}
\tag{C.3}
$$

which cannot be solved analytically. Below the cut–off frequency f_c, γ is real (β = 0) and a wave propagated in z–direction is strongly attenuated as $\mathrm{e}^{-\alpha z}$. For an explanation of permittivity dependant parasitic transmission, it was firstly assumed that this attenuation decreases with increasing permittivity. However, numerical analyses of (C.3) have shown that α is almost constant with respect to the permittivity ε_{r1} of the substrate if f_c is relatively far away from the considered frequency ($f_c > 2 \ f_0$) and $h \leq 0.9 \ b$ holds. Furthermore, for practical substrate thicknesses and housing dimensions ($h \leq b/5$, $b \leq a/2$) the cut–off frequency does not change significantly with the permittivity (low “filling factor”).

On the other hand, the permittivity dependant parasitic transmission can be explained by the existence of tangential field components of the electric field (E_x, E_z with respect to the substrate surface). These components are only present for $\varepsilon_{r1} > 1$ and depend almost linearly on the permittivity value. For high permittivity substrates they are therefore much higher than for low permittivity substrates.

In a microstrip structure, currents with a high surface current density (source a) are present for $y = h$, and these currents can react with the field of the fundamental box mode (field b) according to [35]

$$\langle a, b \rangle = \int_A (J_x(x,z)E_{x2}(x,h,z) + J_z(x,z)E_{z2}(x,h,z))\, dxdz. \tag{C.4}$$

It is clear that this reaction is higher if the tangential field components are higher. Thus, the parasitic box mode is excited more if high permittivity substrates are used because the electric field of the box mode has high tangential components.

Appendix D

Relation between Q_{ext} and τ_{grp}

In section 6.1, the approximation

$$Q_{ext} \approx \frac{\pi}{2}\, \tau_{grp}\, f_0 \tag{D.1}$$

for the relation between the external quality factor Q_{ext} and the group delay τ_{grp} of a loaded resonator was given. This approximation will now be validated.

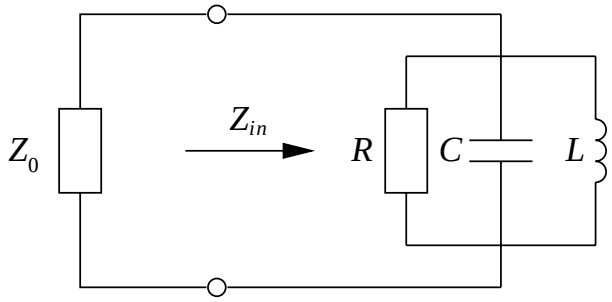

Figure D.1: Equivalent lumped element circuit for a loaded shunt resonator.

Fig. D.1 shows the equivalent lumped element circuit of a loaded shunt resonator. The input impedance Z_{in} of the resonator is given by

$$\frac{1}{Z_{in}} = \frac{1}{R} + j\omega C + \frac{1}{j\omega L}. \tag{D.2}$$

A more general form for Z_{in} is given if the angular frequency ω_0, the characteristic impedance Z_c, and the unloaded quality factor Q_0 are introduced:

$$\omega_0 = \frac{1}{\sqrt{LC}}, \quad Z_c = \sqrt{\frac{L}{C}}, \quad \text{and} \quad Q_0 = \frac{R}{Z_c} \tag{D.3}$$

$$\Longrightarrow \quad Z_{in} = Z_c\, \frac{\omega\, \omega_0\, Q_0}{\omega\, \omega_0 + j\, Q_0\, (\omega^2 - \omega_0^2)}. \tag{D.4}$$

The unloaded quality factor Q_0 in (D.3) has been defined with the dissipated power in the resistor R. Accordingly, the power delivered to the external termination Z_0, an external quality factor Q_{ext} may be defined:

$$Q_{ext} = \frac{Z_0}{Z_c}. \tag{D.5}$$

With this definition, the reflection coefficient $\Gamma(\omega)$ becomes

$$\Gamma(\omega) = \frac{Z_{in} - Z_0}{Z_{in} + Z_0} = \frac{Z_{in} - Z_c\, Q_{ext}}{Z_{in} + Z_c\, Q_{ext}}, \tag{D.6}$$

and inserting (D.4) gives

$$\Gamma(\omega) = \frac{\omega\ \omega_0\ \left(\dfrac{Q_0}{Q_{ext}} - 1\right) - j\ Q_0\ (\omega^2 - \omega_0^2)}{\omega\ \omega_0\ \left(\dfrac{Q_0}{Q_{ext}} + 1\right) + j\ Q_0\ (\omega^2 - \omega_0^2)}. \tag{D.7}$$

With the assumption that the unloaded quality factor is much higher than the external quality factor, i.e. $Q_0 \gg Q_{ext}$, (D.7) may be approximated to

$$\Gamma(\omega) \approx \frac{\omega\ \omega_0\ - j\ Q_{ext}\ (\omega^2 - \omega_0^2)}{\omega\ \omega_0\ + j\ Q_{ext}\ (\omega^2 - \omega_0^2)} \quad = \quad \mathrm{e}^{-j\varphi(\omega)}. \tag{D.8}$$

Following this approximation, $|\Gamma(\omega)| \approx 1$ and

$$\varphi(\omega) \approx 2\ \arctan\left(Q_{ext}\frac{\omega^2 - \omega_0^2}{\omega\ \omega_0}\right) \tag{D.9}$$

results. The group delay $\tau_{grp}(\omega)$ is given by

$$\tau_{grp}(\omega) = \frac{d\varphi(\omega)}{d\omega}, \tag{D.10}$$

and with

$$\frac{d}{d\omega}\arctan\left(X(\omega)\right) = \frac{1}{1 + X^2(\omega)}\ \frac{dX(\omega)}{d\omega}$$

the group delay becomes

$$\tau_{grp}(\omega) \approx \frac{2\ Q_{ext}}{1 + \left(Q_{ext}\ \dfrac{\omega^2 - \omega_0^2}{\omega\ \omega_0}\right)^2}\left(\frac{1}{\omega_0} + \frac{\omega_0}{\omega^2}\right). \tag{D.11}$$

At the resonant frequency, i.e. $\omega = \omega_0$, (D.11) reduces to

$$\tau_{grp}(\omega = \omega_0) = \tau_{grp} \approx \frac{4\ Q_{ext}}{\omega_0} \tag{D.12}$$

$$\Longrightarrow \quad Q_{ext} \approx \frac{\pi}{2}\ \tau_{grp}\ f_0 \qquad \text{for} \qquad Q_0 \gg Q_{ext}. \tag{D.13}$$

The same result is obtained for a series resonator.

Acknowledgements

First of all I would like to thank Prof. Dr. H. Chaloupka for giving me the opportunity to work on the relatively new field of applied high temperature superconductivity. Furthermore, I could frequently profit from his experience and advice.

I am particularly grateful to Robert B. Greed for reviewing the manuscript of this work. His thorough scrutiny helped to make it a lot more understandable.

I would also like to thank Arno Baumfalk and Serguei Kolesov who have been my colleagues at the University of Wuppertal for more than four years now. With both I could discuss or ask for advice any time.

The patterning of the HTS devices was done by various people. Firstly, I thank Benedict Aschermann and Frank Hill (Physics Department, University of Wuppertal) who patterned the first devices which I designed. Their job was taken over by Dorothea Wehler (Cryoelectra GmbH), and she also helped decisively to improve the metallic contacts of the devices. The devices which were developed for the project SUCOMS were fabricated with the help of Dieter Jedamzik, Jens Holland (both at that time GEC Marconi, UK) and Jean–Claude Mage (Thomson CSF, France).

List of Symbols

a_i	wave coefficient (incident waves)
b_i	wave coefficient (reflected or transmitted waves)
$\mathbf{B}$	magnetic flux density vector
c_0	speed of light in vacuum; $299,792,458$ m/s
d	disctance between resonators
E	electric field
$\mathbf{E}$	electric field vector
E_t	tangential electric field
f	frequency
f_0	resonant frequency
Δf	bandwidth
h	substrate height
H	magnetic field
$\mathbf{H}$	magnetic field vector
H_t	tangential magnetic field
I	electric current
J_s	electric surface current density
k	coupling coefficient
k_z	wave number
l	resonator length
l_c	geometric parameter of a resonator
P_{IP3}	input power at third order intercept point
P_{dis}	dissipated power
Q	quality factor
Q_0	unloaded quality factor
Q_c	conductor quality factor
Q_d	dielectric quality factor
Q_{ext}	external quality factor
Q_f	film quality factor
Q_h	housing quality factor
Q_l	loaded quality factor

Q_p	packaging quality factor
R_{eff}	effective surface resistance
R_s	surface resistance
s	spacing between microstrip lines
S	surface
S_{ij}	scattering parameter
t	film thickness
T	temperature
T_c	critical temperature of a superconductor
V	volume
w	microstrip resonator line width
W	stored energy
X_s	surface reactance
Z_0	free space wave impedance; $\sim 377\ \Omega$
Z_c	resonator characteristic impedance
Z_L	transmission line impedance
Z_s	surface impedance
β_d	geometric factor
δ	loss tangent angle; skin depth
ε	permittivity
ε_0	free space permittivity; $\sim 8.854 \cdot 10^{-12}$ As/(Vm)
ε_r	relative dielectric permittivity
$\varepsilon_{r,eff}$	effective relative dielectric permittivity
κ	conductivity
λ_0	free space wavelength
λ_g	guided wavelength
λ_L	London penetration depth
μ_0	free space permeability; $4\pi \cdot 10^{-7}$ Vs/(Am)
μ_r	relative permeability
τ_{grp}	group delay
ω	angular frequency
ω_0	resonant angular frequency

List of Figures

References

[1] I. Bahl and P. Bhartia, *Microwave Solid State Circuit Design*. John Wiley & Sons Inc., 1988.

[2] G. L. Matthaei, L. Young, and E. M. T. Jones, *Microwave Filters, Impedance–Matching Networks, and Coupling Structures*. Dedham, MA: Artech House Books, 2. ed., 1985.

[3] Sonnet Software, Liverpool, NY, *Sonnet User's Manual Release 6.0*, 1999.

[4] R. Levy, "Filters with single transmission zeros at real or imaginary frequencies," *IEEE Trans. Microwave Theory Tech.*, vol. 24, pp. 172–181, April 1976.

[5] H. K. Onnes *Leiden Comm.*, vol. 120 b, no. 3, 1911.

[6] J. G. Bednorz and K. A. Müller, "Possible high T_c superconductivity in the La–Ca–Cu–O system," *Z. Physik*, vol. B 64, pp. 189–193, 1986.

[7] M. J. Lancaster, *Passive Microwave Device Applications of High–Temperature Superconductors*. Cambridge, UK: Cambridge University Press, 1997.

[8] M. Hein, *High–Temperature–Superconductor Thin Films at Microwave Frequencies*, vol. 155 of *Springer Tracts in Modern Physics*. Berlin: Springer, 1999.

[9] H. Weinstock, ed., *Applications of Superconductivity*. Nato ASI Series, Kluwer Academic Publishers, 2000.

[10] I. B. Vendik and O. G. Vendik, *High Temperature Superconductive Devices for Microwave Signal Processing*. St.–Petersburg, Russia: SCLADEN Ltd, 1997.

[11] I. B. Vendik, O. G. Vendik, and D. Kaparkov, "Superconducting microwave circuits," in *High Temperature Superconductive Devices for Microwave Signal Processing*, vol. II, St.–Petersburg, Russia: SCLADEN Ltd, 1997.

[12] A. Enokihara, K. Setsune, K. Wasa, M. Sagawa, and M. Makimoto, "High–T_c bandpass filter using miniaturised microstrip hairpin resonators," *Electr. Lett.*, vol. 28, pp. 1925–1926, September 1992.

[13] J. D. Goettee, W. J. Skocpol, D. E. Oates, and P. M. Mankiewich, "Two–GHz microstrip thin–film resonators of Nb and $YBa_2Cu_3O_7$," *IEEE Trans. Appl. Superconductivity*, vol. 4, pp. 2547–2550, June 1995.

[14] J. Krupka, R. G. Geyer, M. Kuhn, and J. H. Hinken, "Dielectric properties of single crystals of Al_2O_3, $LaAlO_3$, $NdGaO_3$, $SrTiO_3$, and MgO at cryogenic temperatures," *IEEE Trans. Microwave Theory Tech.*, vol. 42, pp. 1886–1889, October 1994.

[15] C. Zuccaro, M. Winter, N. Klein, and K. Urban, "Microwave absorption in single crystals of lanthanum aluminate," *J. Appl. Phys.*, vol. 82, pp. 5695–5703, November 1997.

[16] T. Konaka, M. Sato, H. Asano, and S. Kubo, "Relative permittivity and dielectric loss tangent of substrate materials for high–T_c superconducting film," *J. Superconductivity*, vol. 4, no. 4, pp. 283–288, 1991.

[17] J.-F. Liang, C.-F. Shih, Q. Huang, D. Zhang, and G.-C. Liang, "HTS microstrip filters with multiple symmetric and asymmetric prescribed transmission zeros," in *1999 IEEE MTT–S Int. Microwave Symp. Dig.*, pp. 1551–1554, June 1999.

[18] E. R. Soares, "Design and construction of high performance HTS pseudo–elliptic band–stop filters," in *1999 IEEE MTT–S Int. Microwave Symp. Dig.*, pp. 1555–1558, June 1999.

[19] T. Kässer, M. Klauda, C. Neumann, E. Guha, S. Kolesov, A. Baumfalk, and H. Chaloupka, "A satellite repeater comprising superconducting filters," in *1998 IEEE MTT–S Int. Microwave Symp. Dig.*, pp. 375–378, June 1998.

[20] S. Rastuttis, "Temperatur– und Frequenzabhängigkeit der Oberflächenimpedanz von HTSL–Mehrschichtstrukturen," Master's thesis, Bergische Universität Wuppertal, Fachbereich Elektrotechnik, Wuppertal, Germany, September 1996. (in German).

[21] A. Baumfalk, M. Reppel, H. Chaloupka, and S. Kolesov, "Investigations on the unloaded quality factor of planar resonators with respect to substrate materials and packaging," in *Applied Superconductivity 1999*, pp. 311–314, Inst. Phys. Conf. Ser., no. 167, 1999.

[22] M. Sucher and J. Fox, eds., *Handbook of Microwave Measurements*, vol. II. New York: John Wiley & Sons, Inc., 3 ed., 1964.

[23] H. Kinder, P. Berberich, B. Utz, and W. Prusseit, "Double–sided YBCO films on 4 inch substrates by thermal reactive evaporation," *IEEE Trans. Appl. Superconductivity*, vol. 5, no. 2, pp. 1575–1580, 1995.

[24] B. Utz, R. Semerad, M. Bauer, W. Prusseit, P. Berberich, and H. Kinder, "Deposition of YBCO and NBCO films on areas of 9 inches in diameter," *IEEE Trans. Appl. Superconductivity*, vol. 7, no. 2, pp. 1272–1277, 1997.

[25] T. Köpke, "Untersuchungen zur Kontaktierung von koaxialen Steckverbindern mit Mikrostreifenleitungen," Master's thesis, Bergische Universität Wuppertal, Fachbereich Elektrotechnik, Wuppertal, Germany, March 1997. (in German).

[26] R. B. Greed, "Mechanical analysis." ACTS/SUCOMS deliverable number AC115/GEC/MRC/DS/I/005/b1, April 1997.

[27] P. Fletcher, "CDMA – the answer to the multiple choice," *Mobile Europe*, pp. 25–27, September 1998.

[28] R. Arnott, S. Ponnekanti, C. Taylor, and H. Chaloupka, "Advanced base station technology," *IEEE Comm. Mag.*, pp. 96–102, February 1998.

[29] R. Saal, *Handbuch zum Filterentwurf – Handbook of Filter Design*. AEG–Fachbücher, Heidelberg: Hüthig, 2. ed., 1988. (in German and English).

[30] Compact Software, *SuperCompact® User's Manual*, 1996.

[31] T. Dahm and D. J. Scalapino, "Theory of intermodulation in a superconducting mircrostrip resonator," *J. Appl. Phys.*, vol. 81, pp. 2002–2009, February 1997.

[32] H. Chaloupka, M. Jeck, B. Gurzinski, and S. Kolesov, "Superconducting planar disk resonators and filters with high power handling capability," *Electr. Lett.*, vol. 32, no. 18, pp. 1735–1736, 1996.

[33] T. Kässer, *Herstellung, Abgleich und Charakterisierung planarer Mikrowellenfilter aus Hochtemperatursupraleitern*. PhD thesis, Bergische Universität Wuppertal, Fachbereich Elektrotechnik, Wuppertal, Germany, 1999. (in German).

[34] H.-G. Unger, *Elektromagnetische Theorie für die Hochfrequenztechnik*, vol. I+II. Hüthig, 1981. (in German).

[35] J. A. Kong, *Theory of Electromagnetic Waves*. John Wiley & Sons Inc., 1975.